DEVELOPMENT OF MEMS SENSORS FOR MEASURMENTS OF PRESSURE, RELATIVE HUMIDITY, AND TEMPERATURE

A Thesis
Submitted to the faculty
of the

Worcester Polytechnic Institute

in partial fulfillment of the requirements for the
Degree of Master of Science
in
Mechanical Engineering
by

Houri Johari

29 April, 2003

Approved:

_____
Prof. Ryszard J. Pryputniewicz, Major Advisor

_____
Prof. John J. Blandino, Member, Thesis Committee

_____
Prof. Brian J. Savilonis, Member, Thesis Committee

_____
Prof. Cosme Furlong, Member, Thesis Committee

_____
Mr. Robert Sulouff, Director of Business Development, Analog Devices
Member, Thesis Committe

_____
Prof. John M. Sullivan, Graduate Committee Representative

by

Houri Johari
NEST – NanoEngineering, Science, and Technology
CHSLT- Center for Holographic Studies and Laser micro-mechaTronics
Mechanical Engineering Department
Worcester Polytechnic Institute
Worcester, MA 01609-2280

SUMMARY

Continued demands for better control of the operating conditions of structures and processes have led to the need for better means of measuring temperature (T), pressure (P), and relative humidity (RH). One way to satisfy this need is to use MEMS technology to develop a sensor that will contain, in a single package, capabilities to simultaneously measure T, P, and RH of its environment. Because of the advantages of MEMS technology, which include small size, low power, very high precision, and low cost, it was selected for use in this thesis. Although MEMS sensors that individually measure T, P, and RH exist, there are no sensors that combine all three measurements in a single package.

In this thesis, a piezoresistive pressure sensor and capacitive humidity sensor were developed to operate in the range, of 0 to 2 atm and 0% to 100%, respectively. Finally, a polysilicon resistor temperature sensor, which can work in the range of –50ºC to 150ºC, was analyzed. Multimeasurement capability will make this sensor particularly applicable for point-wise mapping of environmental conditions for advanced process control. In this thesis, the development of sensors for such an integrated device is outlined. Selected results, based on the use of analytical, computational, and experimental solutions (ACES) methodology, particularly suited for the development of MEMS sensors, are presented for the pressure, relative humidity, and temperature sensors.

ACKNOWLEGEMENTS

I would like to thank Professor Ryszard J. Pryputniewicz for his advice and support in the research and writing of this thesis.

I would like also to thank Professor Cosme Furlong, Mr. Peter Hefti, Mr. Kevin Bruff, Mr. Shivananda Pai Mizar, and Mr. Hamid Ghadyani for their invaluable help and patience through the entire thesis and experimental work. Also, thanks to all of the other members of Center for Holographic Studies and Laser micro-mechaTronics (CHSLT) for their support and help.

I would like to express my great gratitude to my mother for her love and encouragement throughout my studies at WPI.

TABLE OF CONTENTS

LIST OF FIGURES

LIST OF TABLES

NOMENCLATURE

a	length of the diaphragm, length fingers of the top electrode in humidity sensor
b	width of the diaphragm, width fingers of the top electrode in humidity sensor
c	specific heat
d	thickness of dielectric in humidity sensor
e_T	trapping state energy referred to E_i at grain boundary
h	Planck's constant (J-s), thickness of the diaphragm
k	thermal conductivity
l	half-width of crystallite neutral region
l_i, m_i, n_i	direction cosine used for axis rotation
m, n	number of terms in the diaphragm deflection equation
m_{ij}	effective mass for the i^{th} and j^{th} valley
m_x, m_y, m_z	effective mass component for a single valley
m_e^*	electron effective mass
m_h^*	hole effective mass
n	number of fingers of top electrode in humidity sensor
n_i	intrinsic carrier concentration
p	hole concentration
$p(0)$	hole concentration in neutral region or at center of the grain
p	average carrier (hole) concentration
q	elementary charge
x, y, z	Cartesian coordinate
v_r	recombination velocity
v_d	diffusion velocity
w	width of strain gauge, the barrier width
A	cross-sectional area of a conductor, cross-section area of resistor
A'	general Richardson's characteristic
C	capacitance in humidity sensor
C_0	initial capacitance in humidity sensor
C_f	final capacitance in humidity sensor
C_{nor}	normalized capacitance in humidity sensor
D	diffusion constant, flexural rigidity of the plate
E	modulus of elasticity
E_a	activation energy of resistivity to $1/kT$
E'_a	exponential term
E_g	energy band gap
E_i	intrinsic Fermi level referred to E_{io}, the input voltage
E_{io}	intrinsic Fermi level at center of grain
E_o	the output voltage
E_A	impurity (acceptor) level

E_F	Fermi energy level
E_T	grain-boundary trapping state energy referred to E_{io}
F	the rate of transfer per unit area
G	modulus of rigidity
GF	gauge factor
I	current
I_s	saturation current
J	current density
K_1	the constant which depends on the moisture material
K_2	the constant which depends on the moisture material
K	Boltzmann's consutant
L	grain size, length of a conductor, silicon grain length
L_{gb}	the grain boundary length
M	moisture concentration diffusion
M_0	the initial moisture concentration
M_1	the solution for moisture concentration with zero boundary condition
M_2	the solution for moisture concentration with zero initial condition
M_n	molecular weight of water
M_s	the constant moisture concentration diffuses from boundary
N	doping concentration
N_c	effective density of states (m^{-3})
N^+	ionized impurity concentration
N^*	doping concentration below which grains are completely depleted
N_g	number of grains between resistor contacts
P	uniform pressure applied to the diaphragm
P_o	the initial pressure
Q_T	grain-boundary trapping state density
Q_T^+	effective (or ionized) trapping state density
R	resistance
R_p	pressure ratio
R_s	stress ratio
$R_{<\alpha\beta\gamma>}$	relative abundance of the $<\alpha\beta\gamma>$ orientation
Sa	the sub term in sensitivity equation
Sb	the sub term in sensitivity equation
SF	scaling factor
S_{ij}, S'_{ij}	reduced form of the compliance tensor for the x, y, z and x', y', z' axes
T	temperature
U	the bending strain energy for the diaphragm
V_a	applied voltage between resistor contacts
V_{ba}	applied voltage across grain boundary barriers
V_c	applied voltage across crystallite neutral region
V_g	applied voltage across each grain
V_B	built-in potential barrier height

W	the potential energy due to deflection by external force, width of depletion region
$\alpha_{m,n}$	the coefficient in the moisture concentration Eq
α	the coefficient for maximum stress in a rectangular diaphragm
β	the coefficient for maximum deflection in a rectangular diaphragm
δ	grain-boundary thickness
δ_{ij}	Kroneka delta
ε	Single-crystal silicon permittivity
ε_0	permittivity
ε_r	relative permittivity
ε_x, ε_y, ε_z	strain components
ε_l, ε_t	longitudinal and transverse strain
ϕ_b	barrier height relative to the Fermi level
γ_{xy}	shear strain
μ_{eff}	Polysilicon effective mobility
μ_n	electron mobility of single-crystal silicon
μ_p	hole mobility of single-crystal silicon
ν	Poisson ratio
π	the potential energy of the system
π_l	longitudinal piezoresistive coefficients
π_t	transverse piezoresistive coefficients
π_{lg}	longitudinal piezoresistive coefficient of the grain
π_{lb}	longitudinal piezoresistive coefficient of the barrier
θ, ϕ, φ	Euler's angels for axis rotation
$\theta_{\alpha\beta\gamma}$, $\phi_{\alpha\beta\gamma}$	Euler's angles to describe the $\alpha\beta\gamma$ orientation
ρe	the electrical resistivity
ρ	polysilicon resistivity, density
ρ_b	barrier resistivity
ρ_g	grain resistivity
ρ_B	barrier resistivity
ρ_C	crystallite bulk resistivity
ρ_{GB}	grain-boundary resistivity
σ_x, σ_y, σ_z	stress components
ξ	deflection of flat plate in z-direction
$\Delta\rho_e$	change in the electrical resistivity
$\Delta\rho_b$	change in the barrier resistivity
$\Delta\rho_g$	change in the grain resistivity
$[\Delta]$	resistivity tensor
$[\pi]$	piezoresistive tensor
[T]	stress tensor

1. INTRODUCTION

The term MEMS is an acronym of microelectromechanical systems. The concept of MEMS can be traced back in history by about four decades, to the time when Prof. Richard Feynmann lectured on the subject in a talk titled: "There's plenty of room at the bottom (Feynmann, 1959)." Feynmann suggested what micromachines could be, why one would want to use them, how to build them, and how physics for machines at the microscale would be different from that for machines at the macroscale (MEMS). A MEMS is constructed to achieve a certain engineering functions by electromechanical or electrochemical means. The core element in MEMS generally consists of two principal components: a sensing or actuating element and a signal transudation unit.

Microsensors are built to sense the existence and the intensity of certain physical, chemical, or biological quantities, such as temperature, pressure, force, humidity, light, nuclear radiation, magnetic flux, and chemical composition (Hsu, 2002). Microsensors have the advantage of being sensitive and accurate with minimal amount of required sample substance. A sensor is a device that converts one form of energy into another and provides the user with a usable energy output in response to a specific measurable input (Madou, 1997).

MEMS have been used to describe microminiature systems that are constructed with both integrated circuit (IC) based fabrication techniques and other mechanical fabrication techniques (Madou, 1997). In most cases, an emphasis has been placed on having the techniques compatible with IC techniques to ensure the availability of related electronics close by. In this chapter, the techniques for the fabrication of

microelectromechanical devices are briefly introduced. Pressure, temperature, and humidity sensors are presented together with their particular applications. The processes for the fabrication of microelectromechanical devices are as follows:

1) bulk micromachining,
2) surface micromachining,
3) LIGA (Lithographie, Galvanoformung, Abformung) micromachining.

Out of three processes listed above, the surface micromachining, was used for the first successful commercial application of a MEMS (Hsu, 2002).

1.1. Bulk micromachining

Bulk micromachining is the oldest process for the production of MEMS, and it was developed in the 1960s (Diem, et al., 1995). Areas of single crystal silicon that have first been exposed through a photolithographic mask are removed by alkaline chemicals (Stix, 1992). Etching produces concave, pyramidal or other faceted holes, depending on which face of the crystal is exposed to the chemicals (Tang, 2001). These sculpted-out cavities can then become the building blocks for cantilevers, diaphragms, or other structural elements needed to make devices such as pressure or acceleration, sensors. This technique has come to be known as bulk micromachining because the chemicals that pit deeply into the silicon produce structures that use the entire mass of the chip (Tao and Bin, 2002). This process has the disadvantage that it uses alkaline chemicals to conventional chip processing (Camporesi, 1998).

1.2. Surface micromachining

The limitations of bulk micromachining have been overcome by surface micromachining (Lyshevsky, 2002). This technique parallels electronic fabrication so closely that it is essentially a series of steps added to the making of a microchip (Mehregany and Zorman, 2001). It is called surface micromachining because it deposits a film of silicon oxide a few microns thick, from which beams and other edifices can be built (Gabriel, 1995). Photolithography creates a pattern on the surface of a wafer, marking off an area that is subsequently etched away to build up micromechanical structures (Chen, et al., 2002). Manufacturers start by patterning and etching a hole in a layer of silicon dioxide deposited on the silicon wafer. A gaseous vapor reaction then deposits a layer of polycrystalline silicon, which coats both the hole and the remaining silicon dioxide material (Hsu, 2002). The silicon deposited into the holes becomes the base of, for instance, a beam and the same material that overlays the silicon dioxide forms the suspended part of the beam structure. In the final step the remaining silicon dioxide is etched away, leaving the polycrystalline silicon beam free and suspended above the surface of the wafer. The thinness of these structures is a challenge to the designer, who must derive useful work from machines whose form is essentially two-dimensional (Camporesi, 1998).

1.3. LIGA micromachining

A technique that allows overcoming the two-dimensionality of surface micromachining is the LIGA (Lithographie, Galvanoformung, Abformung) process. The

technology was developed in Germany as a method for separation of uranium isotopes using miniaturized nozzles (Ehrfeld, et al., 1988). It is able to produce a microstructure with a height ranging from a few to hundreds of microns, and like bulk and surface micromachining relies on lithographic patterning. But instead of ultraviolet light streaming through a photolithographic mask, this process utilizes high-energy x-ray that penetrates several hundred microns into a thick layer of polymer. Exposed areas are stripped away with a developing chemical, leaving a template that can be filled with nickel or another material by electrode position (Bacher, et al., 1994). What remains may be either a structural element or the master for a molding process. As with surface micromachining, LIGA structures can be processed to etch away an underlying sacrificial layer, leaving suspended or movable structures on a substrate (Hruby, 2001). The entire process can be carried out on the surface of a silicon chip, giving LIGA a degree of compatibility with microelectronics (Stadler and Ajmera, 2002). The biggest limitation of this technology is the availability of high-energy synchrotrons for the x-ray generation. There are, for instance, no more than ten synchrotrons in the USA (Holmes, 2002).

To date, the integrated circuit industry has been the technology base that has driven MEMS. The MEMS community has made significant advances in the area of deep etching bulk silicon and in surface (sacrificial etching) micromachining with polysilicon. MEMS have driven the silicon industry into understanding the mechanical and electrical properties of silicon structures. MEMS have driven researchers to investigate fabrication methods other than IC-based techniques to obtain microdevices.

These techniques include LIGA, laser-assisted chemical vapor deposition (CVD), and electrodes plating (Renard and Gaff, 2000).

The advantages of the MEMS technology include small size, low power, very high precision, and the potential for low cost through batch processing. MEMS does offer a challenge in the area of how to effectively package devices that require more than an electrical contact to the out of package. Pressure sensors are the most commercially successful MEMS-type sensors to use circuit-type packaging. Hall sensors, magnetoresistive sensors, and silicon accelerometers have all used IC-based packaging (Itoh, et al., 2000). The IC packaging is viable with these devices since the measurand can be introduced without violating the package integrity. Some optical systems use IC-type packages with windows. MEMS will require the development of an extensive capability in packaging to allow the interfacing of sensors to the environment (Blates, et al., 1996). The general area of MEMS durability is also one that has to be improved. Proven durability is a major need before MEMS technology can be extended to high reliability, long-term (greater than five years) applications.

The greatest impact of MEMS is likely to be in the medical field. A true MEMS medicine dispenser (sensor, actuator, and control) should allow the treatment of patients to improve substantially. The ability to monitor and dispense medicine as required by the patient will improve the treatment of both chronic (e.g., diabetes) and acute (e.g., infectious) conditions (Camporesi, 1998).

Within the next ten years, MEMS will find applications in a variety of areas, including:

1) Remote environmental monitoring and control, which can vary from sampling, analyzing, and reporting to doing on-site control. The applications could range from building environmental control to dispensing nutrients to plants,
2) Dispensing known amounts of materials in difficult-to-reach places on an as-needed basis, which could be applicable in robotic systems,
3) Automotive applications will include intelligent vehicle highway systems and navigation applications,
4) Consumer products will see uses that allow the customer to adapt the product to individual needs. This will range from the automatic adjustment of a chair contour to measuring the quality and taste of water, and compensating for the individual requirements at the point of use (Giachino, 2001).

1.4. Pressure sensors

Mechanical methods of measuring pressure have been known for centuries. The first pressure gauges used flexible elements as sensors. As pressure changed, the flexible element moved, and this motion was used to rotate a pointer in front of a dial. In these mechanical pressure sensors, a Bourdon tube, a diaphragm, or a bellows element detected the process pressure and caused a corresponding movement.

1.4.1. Bourdon tube

A bourdon tube is C-shaped and has an oval cross-section with one end of the tube connected to the process pressure. The other end is sealed and connected to the pointer or transmitter mechanism. To increase their sensitivity, Bourdon tube elements can be extended into spirals or helical coils. This increases their effective angular length and, therefore, increases the movement at their tip, which in turn increases the resolution of the transducer (Figliola and Beasley, 1991).

Designs in the family of flexible pressure sensor elements also include the bellows and the diaphragms, Fig.1.1. Diaphragms are popular because they require less space and because the motion (or force) they produce is sufficient for operating electronic transducers. They also are available in a wide range of materials for corrosive service applications (Omegadyne, 1996).

After the 1920s, automatic control systems evolved in industry, and by the 1950s pressure transmitters and centralized control rooms were commonplace. Therefore, the free end of a Bourdon tube (bellows or diaphragm) no longer had to be connected to a local pointer, but served to convert a process pressure into a transmitted (electrical or pneumatic) signal. At first, the mechanical linkage was connected to a pneumatic pressure transmitter, which usually generated a 3-15 psig output signal for transmission over distances of several hundred feet, or even farther with booster repeaters (Omega, 1996). Later, as solid-state electronics matured and transmission distances increased, pressure transmitters became electronic. The early designs generated dc voltage outputs:

10-50 mV, 0-100 mV, 1-5 V (Omega, 2003), but later were standardized as 4-20 mA dc current output signals.

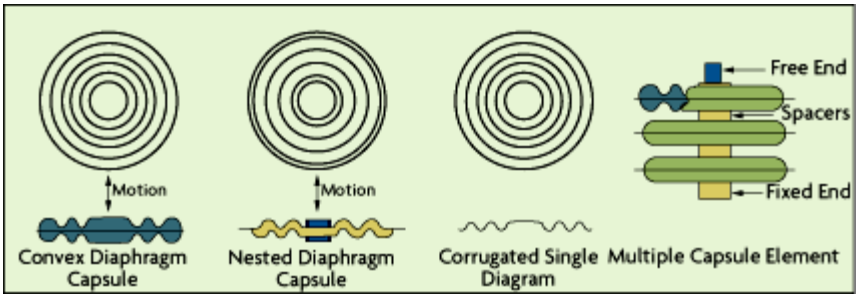

Fig. 1.1. Pressure sensor diaphragm (Omega, 2003).

Because of the inherent limitations of mechanical motion-balance devices, first the force-balance and later the solid state pressure transducer were introduced.

1.4.2. Strain gauge pressure sensors

The first unbonded-wire strain gauges were introduced in the late 1930s. In this device, the wire filament is attached to a structure under strain, and the resistance in the strained wire is measured. This design was inherently unstable and could not maintain calibration. There also were problems with degradation of the bond between the wire filament and the diaphragm, and with hysteresis caused by thermoelastic strain in the wire (Omega, 1996).

The search for improved pressure and strain sensors first resulted in the introduction of bonded thin-film and finally diffused semiconductor strain gauges. These were first developed for the automotive industry, but shortly thereafter moved into the general field of pressure measurement and transmission in all industrial and scientific

applications. Semiconductor pressure sensors are sensitive, inexpensive, accurate, and repeatable (Omega, 2003). When a strain gauge, which is shown in Fig. 1.2, is used to measure the deflection of an elastic diaphragm or Bourdon tube, it becomes a component in a pressure transducer. Strain gauge-type pressure transducers are widely used.

Strain-gauge transducers are used for narrow-span pressure and for differential pressure measurements. Essentially, the strain gauge is used to measure the displacement of an elastic diaphragm due to a difference in pressure across the diaphragm. These devices can detect gauge pressure if the low pressure port is left open to the atmosphere, or differential pressure if connected to two process pressures. If the low pressure side is a sealed vacuum reference, the transmitter will act as an absolute pressure transmitter (Omega, 2003).

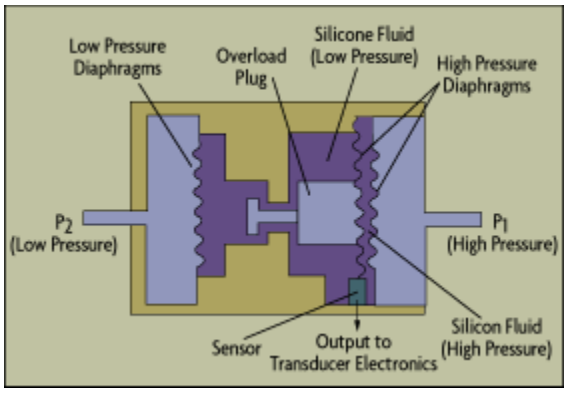

Fig. 1.2. Strain-gauge based pressure cell (Omega, 2003).

1.4.3. Potentiometric pressure sensors

The potentiometric pressure sensor provides a simple method for obtaining an electronic output from a mechanical pressure gauge. The device consists of a precision

potentiometer, whose wiper arm is mechanically linked to a Bourdon or bellows element. The movement of the wiper arm across the potentiometer converts the mechanically detected sensor deflection into a resistance measurement, using a Wheatstone bridge circuit Fig. 1.3 (Omega, 2003).

The mechanical nature of the linkages connecting the wiper arm to the Bourdon tube, bellows, or diaphragm element introduces unavoidable errors into this type of measurement. Temperature effects cause additional errors because of the differences in thermal expansion coefficients of the metallic components of the system. Errors will also develop due to mechanical wear of the components and of the contacts (Liptak, 1995).

Potentiometric transducers can be made small and installed in very tight quarters, such as inside the housing of a 4.5-in. dial pressure gauge. They also provide an output that can be used without additional amplification. This permits them to be used in low power applications. They are also inexpensive. Potentiometric transducers can detect pressures between 5 and 10,000 psig (35 kPa to 70 MPa). Their accuracy is between 0.5% and 1% of full scale because using electrical community instead of mechanical, not including drift and the effects of temperature (Omega, 2003).

1.4.4. Resonant-wire pressure sensors

The resonant-wire pressure transducer was introduced in the late 1970. In this design, Fig 1.4, a wire is gripped by a static member at one end, and by the sensing diaphragm at the other (Avallone and Baumeister, 1996).

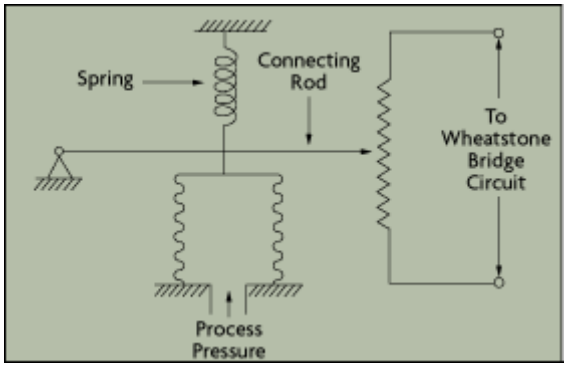

Fig. 1.3. Potentiometric pressure transducer (Omega, 2003).

An oscillator circuit causes the wire to oscillate at its resonant frequency. A change in process pressure changes the wire tension, which in turn changes the resonant frequency of the wire. A digital counter circuit detects the shift. Because this change in frequency can be detected quite precisely, this type of transducer can be used for low differential pressure applications as well as to detect absolute and gauge pressures.

The most significant advantage of the resonant wire pressure transducer is that it generates an inherently digital signal, which can be sent directly to a stable crystal clock in a microprocessor. Limitations include sensitivity to temperature variation, a nonlinear output signal, and some sensitivity to shock and vibration. These limitations typically are minimized by using a microprocessor to compensate for nonlinearities as well as ambient and process temperature variations (Omega, 2003).

1.4.5. Capacitive pressure sensors

Capacitive pressure sensors use a thin diaphragm, usually metal or metal-coated quartz, as one plate of a capacitor. The diaphragm is exposed to the process pressure on one side and to a reference pressure on the other. Changes in pressure cause it to deflect

and change the capacitance. The change may or may not be linear with pressure and is typically a few percent of the total capacitance (Considine, 1993). The capacitance can be monitored by using it to control the frequency of an oscillator or to vary the coupling of an AC signal. The schematic of a capacitive pressure sensor is shown in Fig. 1.5 (Omega, 2003).

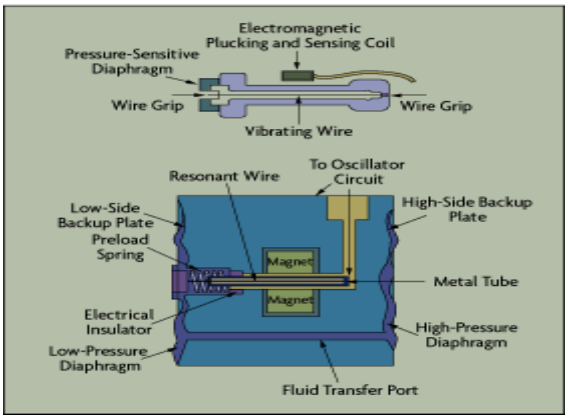

Fig. 1.4. Resonant-wire pressure transducer (Omega, 2003).

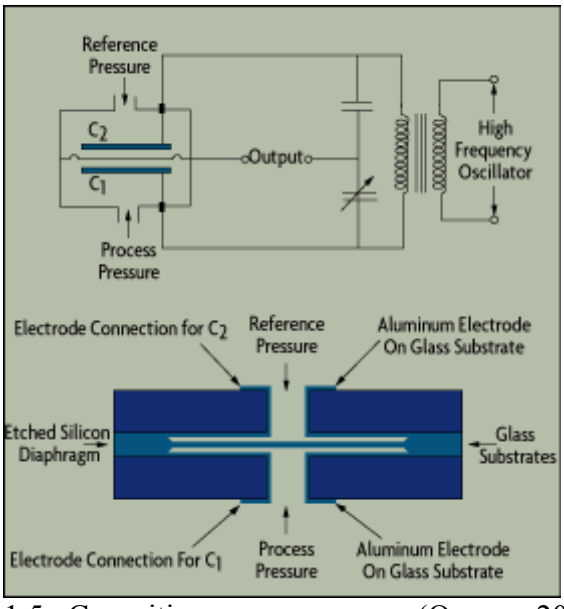

Fig. 1.5. Capacitive pressure sensor (Omega, 2003).

1.4.6. Piezoresistive pressure sensors

The piezoresistive pressure sensor elements consist of a silicon chip with an etched diaphragm and, a glass base anodically bonded to the silicon at the wafer level. The front side of the chip contains four ion-implanted resistors in a Wheatstone bridge configuration. The resistors are located on the silicon membrane and metal paths provide electrical connections. When a pressure is applied, the membrane deflects, the piezoresistors change unbalancing the bridge. Then a voltage develops proportional to the applied pressure (Sugiyama et al., 1983). Silicon piezoresitive sensors have been widely used for industrial and biomedical electronics (Ko, et al., 1979). The piezoresitive sensors have excellent electrical and mechanical stability that can be fabricated in a very small size.

1.5. Humidity sensors

The need for environmental protection has led to expansion in sensor development. Humidity sensors have attracted a lot of attention in industrial and medical fields. The measurement and control of humidity is important in many areas including industry (paper, electronic), domestic environment (air conditioning), medicine (respiratory equipment), etc. Different methods are used for measurements humidity, e.g., changes in mechanical, optical, and electrical properties of the gas water vapor mixtures (White and Turner, 1997; Qu and Meyer, 1992).

Three types of humidity sensors are:

1) capacitive humidity sensor,

2) resistive humidity sensor,

3) thermal conductivity humidity sensor.

1.5.1. Capacitive humidity sensors

Capacitive relative humidity sensors are widely used in industrial, commercial, and weather telemetry applications. They consist of a substrate on which a thin film of polymer or metal oxide is deposited between two conductive electrodes. The sensing surface is coated with a porous metal electrode to protect it from contamination and exposure to condensation. The substrate is typically glass, ceramic, or silicon. The incremental change in the dielectric constant of a capacitive humidity sensor is nearly directly proportional to the relative humidity (RH) of the surrounding environment. The change in capacitance is typically 0.2–0.5 pF for a 1% RH change, while the bulk capacitance is between 100 and 500 pF at 50% RH and 25°C. Capacitive sensors are characterized by low temperature coefficient, ability to function at high temperatures (up to 200°C), full recovery from condensation, and reasonable resistance to chemical vapors. The response time ranges from 30 to 60 s for a 63% RH step change (Laville and Pellet, 2002).

State-of-the-art techniques for producing capacitive sensors take advantage of many of the principles used in semiconductor manufacturing to yield sensors with minimal long-term drift and hysteresis. Thin film capacitive sensors may include monolithic signal conditioning circuitry integrated onto the substrate. The most widely used signal conditioner incorporates a Complementary Metal-Oxide Semiconductor

(CMOS) timer to pulse the sensor and to produce a near-linear voltage output. The typical uncertainty of capacitive sensors is ±2% RH from 5% to 95% RH with two-point calibration. Capacitive sensors are limited by the distance the sensing element can be located from the signal conditioning circuitry, due to the capacitive effect of the connecting cable with respect to the relatively small capacitance changes of the sensor.

Direct field repeatability can be a problem unless the sensor is laser trimmed to reduce variance to ±2% or a computer-based recalibration method is provided (Dokmeci and Najafi, 2001).

1.5.2. Resistive humidity sensors

Resistive humidity sensors measure the change in electrical impedance of a hygroscopic medium such as a conductive polymer, salt, or treated substrate. The impedance change is typically an inverse exponential relationship to humidity. Resistive sensors usually consist of noble metal electrodes either deposited on a substrate by photoresist techniques or wire-wound electrodes on a plastic or glass cylinder. The substrate is coated with a salt or conductive polymer. Alternatively, the substrate may be treated with activating chemicals such as acid. The sensor absorbs the water vapor and ionic functional groups are dissociated, resulting in an increase in electrical conductivity.

The response time for most resistive sensors ranges from 10 to 30 seconds for a 63% (RH). The impedance range of typical resistive elements varies from 1 kΩ to 100 MΩ.

Most resistive sensors use symmetrical AC excitation voltage with no DC bias to prevent polarization of the sensor. The resulting current flow is converted and rectified to a DC voltage signal for additional scaling, amplification, liberalization, or A/D reconversion.

A distinct advantage of resistive RH sensors is their repeatability, usually within ±2% RH, which allows the electronic signal conditioning circuitry to be calibrated by a resistor at a fixed RH point. This eliminates the need for humidity calibration standards, so resistive humidity sensors are generally field replaceable. The accuracy of individual resistive humidity sensors may be confirmed by testing in an RH calibration chamber or by a computer-based data acquisition (DA) system referenced to standardized humidity-controlled environment. Nominal operating temperature of resistive sensors ranges from –40°C to 100°C.

In residential and commercial environments, the life expectancy of these sensors is greater than 5 years, but exposure to chemical vapors and other contaminants such as oil mist may lead to premature failure. Another drawback of some resistive sensors is their tendency to shift values when exposed to condensation if a water-soluble coating is used. Resistive humidity sensors have significant temperature dependencies when installed in an environment with large (>10°F) temperature fluctuations. Simultaneous temperature compensation is incorporated for accuracy. The small size, low cost, interchangeability, and long-term stability make these resistive sensors suitable for use in control and display products for industrial, commercial, and residential applications.

One of the first mass-produced humidity sensors was the Dunmore type, developed by NIST in the 1940s and still in use today (Piezosensors, 2001). It consists of a dual winding of palladium wire on a plastic cylinder that is then coated with a mixture of polyvinyl alcohol (binder) and either lithium bromide (LiBr) or lithium chloride (Licl). Varying the concentration of LiBr or LiCl results in very high-resolution sensors that cover humidity spans of 20% to 40% RH. For a very low RH control function in the 1% to 2% RH range, accuracies of 0.1% can be achieved. Dunmore sensors are widely used in precision air conditioning controls to maintain the environment of computer rooms and as monitors for pressurized transmission lines, antennas, and wave-guides used in telecommunications.

The latest development in resistive humidity sensors uses a ceramic coating to overcome limitations in environments where condensation occurs. The sensors consist of a ceramic substrate with noble metal electrodes deposited by a photoresist process. The substrate surface is coated with a conductive polymer/ceramic binder mixture, and the sensor is installed in a protective plastic housing with a dust filter.

The binding material is a ceramic powder suspended in liquid form. After the surface is coated and air-dried, the sensors are heat treated. The process results in a clear non-water-soluble thick film coating that fully recovers from exposure to condensation. The manufacturing process yields sensors with a repeatability of better than 3% RH over the 15% to 95% RH range. The precision of these sensors is confirmed to ±2% RH by a computer-based DA system coupled to a standard reference. The recovery time from full condensation to 30% is a few minutes. When used with a signal conditioner, the sensor

voltage output is directly proportional to the ambient relative humidity (Piezosensors, 2001).

1.5.3. Thermal conductivity humidity sensors

Thermal conductivity humidity sensors measure the absolute humidity by quantifying the difference between the thermal conductivity of dry air and that of air containing water vapor.

When air or gas is dry, it has a greater capacity to "sink" heat, as in a desert climate. A desert can be extremely hot in the day but at night the temperature rapidly drops due to the dry atmospheric conditions. By comparison, humid climates do not cool down so rapidly at night because heat is retained by water vapor in the atmosphere. Thermal conductivity humidity sensors (or absolute humidity sensors) consist of two matched negative temperature coefficient (NTC) thermistor elements in a bridge circuit; one is hermetically encapsulated in dry nitrogen and the other is exposed to the environment. When current is passed through the thermistors, resistive heating increases their temperature to >200°C. The heat dissipated from the sealed thermistor is greater than the exposed thermistor due to the difference in the thermal conductively of the water vapor as compared to dry nitrogen. Since the heat dissipated yields different operating temperatures, the difference in resistance of the thermistors is proportional to the absolute humidity. A simple resistor network provides a voltage output equal to the range of 0 to 14 mV at 60°C. Calibration is performed by placing the sensor in moisture-free air or nitrogen and adjusting the output to zero. Absolute humidity sensors are very durable,

operate at temperatures up to 575°F (300°C) and are resistant to chemical vapors by virtue of the inert materials used for their construction, i.e., glass, semiconductor material for the thermistors, high-temperature plastics, or aluminum.

An interesting feature of thermal conductivity sensors is that they respond to any gas that has thermal properties different from those of dry nitrogen; this will affect the measurements. Absolute humidity sensors are commonly used in appliances such as clothes dryers and both microwave and steam-injection ovens. Industrial applications include kilns for drying wood; machinery for drying textiles, paper, and chemical solids; pharmaceutical production; cooking; and food dehydration. Since one of the by-products of combustion and fuel cell operation is water vapor, particular interest has been shown in using absolute humidity sensors to monitor the efficiency of those reactions. In general, absolute humidity sensors provide greater resolution at temperatures >200°F than do capacitive and resistive sensors, and may be used in applications where the other sensors would not survive. The typical accuracy of an absolute humidity sensor is ±3 g/m^3; this corresponds to about ±5% RH at 40°C and ±0.5% RH at 100°C.

1.6. Temperature sensors

Measurement of temperature is critical in modern electronic devices, especially laptop computers and other portable devices with densely packed circuits, which dissipate considerable power in the form of heat. Knowledge of system temperature can also be used to effectively control battery charging as well as prevent damage to microprocessor. Compact high power portable equipment often has fan cooling to maintain junction

temperature at proper levels. Accurate control of the fan requires knowledge of critical temperatures from the appropriate temperature sensor. Application of temperature sensors are (Analog Devices, 2000):

1) monitoring
    1.1) portable equipment,
    1.2) CPU temperature,
    1.3) battery temperature,
    1.4) ambient temperature,
2) compensation
    2.1) oscillator drift in cellular phones,
    2.2) thermocouple cold-junction compensation,
3) control
    3.1) battery charging,
    3.2) process control.

Accurate temperature knowledge is required in many other measurement systems such as those used in process control and instrumentation applications.

Temperature sensors provide a change in a physical parameter such as resistance or output voltage in response to changing temperature. Common temperature sensors are: Resistance Temperature Detector (RTD), negative temperature coefficient (NTC) thermistors, thermocouples, and silicon based sensors.

RTDs are wire windings or thin film serpentines that exhibit changes in resistance with changes in temperature. While metals such as copper, nickel, and nickel-iron are

often used, the most linear, and repeatable and stable RTDs are constructed from platinum. Platinum RTDs, due to their linearity and unmatched long term stability, are firmly established as the international temperature reference transfer standard. Thin film Platinum RTDs offer performance matching all but reference grade wire-wounds at improved cost, size, and convenience. Early thin film Platinum RTDs drifted because their higher surface-to-volume ratio made them more sensitive to contamination. Improved film isolation and packaging have since eliminated these problems so that thin film Platinum RTDs are increasingly the first choice over wire-wounds and NTC thermistors (Honeywell, 1998).

NTC Thermistors are composed of metal oxide ceramics, are low cost, and the most sensitive temperature sensors. They are also the most nonlinear and have a negative temperature coefficient. Thermistors are offered in a huge variety of sizes, base resistance values and Resistance versus Temperature (R-T) curves to facilitate both packaging and output linearization schemes. Often two thermistors are combined to achieve a more linear output. Common thermistors have repeatability of 10% to 20%. Tight 1% interchangeabilities are available, but at costs often higher than platinum RTDs. Common thermistors exhibit good resistance stability when operated within restricted temperature ranges and moderate stability 2%/1000 hr at 125°C (Analog Devices, 2000).

Thermocouples consist of two dissimilar metal wires welded together at one end to form one junction. Temperature differences between the junction and the other reference cause a thermoelectric potential (i.e., a voltage) between the two wires. By holding the reference junction at a known temperature and measuring this voltage, the

temperature of the sensing junction can be deduced. Thermocouples have very large operating temperature ranges and the advantage of very small size. However, they have the disadvantages of small output voltages, noise susceptibility from the wire loop, and a relatively high drift (Honeywell, 1998).

Silicon sensors are attractive for many reasons. In fact, most of the physical properties of silicon are known with a high degree of accuracy and highly reproducible behavior can be achieved. Moreover, recent developments in the field of silicon micromachining allow the realization of miniature-integrated devices with extreme precision at affordable costs (Cocorullo, et al., 1997). Silicon sensors are based on silicon batch process technology and make use of both the electrical and mechanical properties of silicon. Since the properties of this temperature sensor are based on those of the chemical element silicon, sensor behavior is as stable as this chemical element. Batch process technology produces silicon temperature sensors that show linear characteristics - unlike the NTC Thermistor - and display a temperature coefficient that is nearly constant over the complete temperature range. Typical applications for silicon sensors include aerospace, military, automotive, medical, and process/industrial control (Honeywell, 1998).

2. FUNDAMENTALS OF MEMS SENSORS

2.1. Fundamental characteristic of pressure sensors

The emerging area of MEMS (i.e., microelectromechanical systems) has its roots in IC processing. After decades of research and development, the state of the art in MEMS processes is capable of integrating microelectronics and sensors on a single chip (Motorola, 1994; Core, et al., 1993). The combination of microelectronics and mechanical components makes MEMS more powerful and versatile than the conventional sensors. The possibility of applying theories and practice of macroscale mechatronics systems to microelectromechanical systems is both attractive and challenging.

This section presents a type of pressure sensor that is designed for small size, low weight, and low cost. Pressure sensors are one of the earliest products made by bulk-micromachining of silicon (Peterson, 1982). These first generation micro-size pressure sensors were developed in the 1970s. Today, many companies fabricate and sell bulk micromachined pressure sensors for automobile, industrial, and biomedical applications. Since these bulk micromachined pressure sensors have been investigated for many years, the knowledge in both areas of fabrication and design is abundant (Tufte, et. al., 1962; Suzuki, et al., 1987).

Pressure sensors based on surface micromachined diaphragms were first proposed and fabricated in the 1980s (Guckel and Burns, 1984). Thin film deposition and reactive sealing technologies were used to fabricate polysilicon diaphragms with cavities underneath. The backside silicon wet etching process that has been used for bulk micromachined pressure sensors was avoided (Sugiyama, et al., 1992). These surface

micromachined pressure sensors may be more attractive than the bulk-micromachined ones because of the following reasons:

1) Bulk-micromachined pressure sensors require anisotropic silicon etching (Bassous, 1995) to create thin diaphragms from the backside of silicon wafers. This process consumes large areas (Suwazono, et al., 1987). For example, if a standard four-inch wafer with thickness of 500 μm is used, an area of about $800\mu m \times 800\mu m$ is required to make $100\mu m \times 100\mu m$ diaphragm. However, an area of only $100\mu m \times 100\mu m$ is needed to make a surface micromachined diaphragm.
2) Bulk micromachined pressure sensors require post processing including glass to silicon bonding before the final packaging process. Surface micromachined pressure sensors are ready for packaging after the micromachining processes.
3) Surface micromachining is easier to be integrated with IC processes for additional signal processing or device functionality (Lin and Yun, 1998).

This chapter presents a design process for surface micromachined pressure sensors. Design optimization for piezoresistive sensing resistors including position, orientation, and length is also addressed.

2.2. Humidity sensors

Determination of humidity is based on the amount of water vapor per unit mass of the atmosphere. As all gases in the atmosphere, water vapor constitutes a finite portion of the total atmospheric pressure. This partial pressure of water vapor is proportional to the atmospheric moisture content and thus provides a measure of the absolute amount of

moisture in the air. If a sample of air is confined over water at a given temperature, it eventually reaches an equilibrium state in which the rate of water molecules leaving the liquid is the same as the rate at which they enter it, Fig 2.1. As a result, the water vapor content in the air and the water vapor pressure become constant. The vapor pressure in this state is called the saturation water vapor pressure and it increases with increasing of temperature (Ahrens, 1985).

Depending on which aspect of water-liquid-vapor equilibrium is emphasized, the amount of atmospheric vapor content is defined either by absolute humidity, specific humidity, the mixing ratio, the relative humidity, or the dew point (Barry and Chorley, 1992).

Absolute humidity is defined as the ratio of the mass of water vapor per unit volume of air, which can be expressed as

$$Absolute\ humidity\left(g/m^3\right)=\frac{mass\ \ of\ \ water\ vapor}{volume\ of\ \ air} \quad . \tag{2.1}$$

The absolute humidity changes with air volume expansion so that it does not give a reliable representation of the overall humidity in the air.

Specific humidity is the ratio of the mass of water vapor (moisture) per unit mass of air-water-vapor mixture

$$Specific\ humidity\left(g/kg\right)=\frac{mass\ \ of\ \ water\ vapor}{unit\ mass\ of\ \ air-water-vapormixture} \quad . \tag{2.2}$$

Mixing ratio is defined as the mass of water vapor per unit mass of dry air (which does not include moisture):

$$Mixing\ ratio\left(g/kg\right)=\frac{mass\ of\ water\ vapor}{mass\ of\ dry\ air}\quad . \tag{2.3}$$

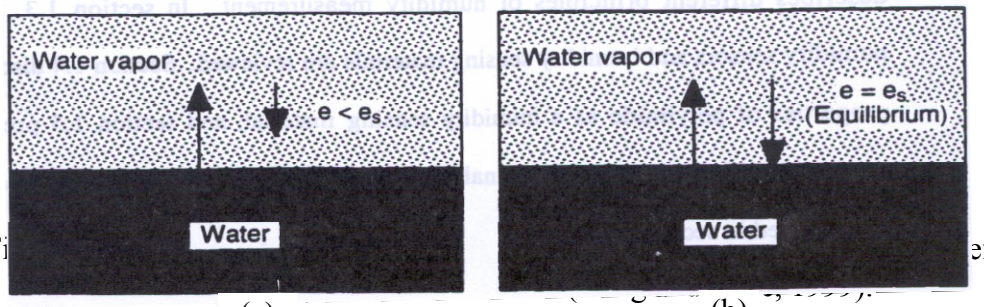

Fi efore

(a) (b)

Relative humidity is the ratio of the water vapor content in the air to the maximum amount of water vapor that the air can retain at a given temperature, i.e.,

$$\text{Re}\,lative\ humidity=\frac{amount\ \ of\ water\ vapor\ in\ the\ air}{amount\ of\ \ water\ vapor\ the\ air\ can\ hold}\quad . \tag{2.4}$$

Since the saturation vapor pressure is a function of temperature, the relative humidity changes not only with the amount of water vapor in the air, but also with temperature. The relative humidity is important because it is a dimensionless parameter and it is associated with dryness of material.

Dew point is the temperature to which the air would have to be cooled for saturation to occur while the air pressure and the moisture content are kept constant. The difference between the ambient temperature and the dew point is a measure of the ambient relative humidity; when this temperature difference is larger the relative humidity is lower.

2.3. Temperature sensors

Polysilicon has been studied for many years and has found an increasing number of recent applications (Kazmerski, 1980) in solar cells, integrated circuit elements such as silicon–gate MOS devices, interconnection passivation or isolation layers, monolithic distributed RC filters, and high value resistors. Polysilicon resistors are important for integrated circuits for the following reasons:

1) they are compatible with such monolithic silicon technologies as MOS and bipolar (BJT) processes (Gerzberg, 1979),
2) resistance can be adjusted through several decades by ion implantation where the lightly doped material has a sheet resistance as high as that of pure intrinsic single-crystal silicon. This is especially required in low-power circuits,
3) resistors top-deposited on the field oxide of MOS ICs or on the isolation region of bipolar transistors require no additional area compared to the large space occupied by diffused or ion-implanted resistors (Lu, 1981),
4) because they are isolated by a thick oxide, resistance is much less dependent on substrate bias, and parasitic capacitance is smaller than that resulting from junction isolation in diffused or implanted resistors,
5) their linearity is good for a typical electric field where sheet resistance ranges as high as GΩ/□; this is in contrast to the much lower linearity and less controllability of all other monolithic resistors (Gerzberg, 1979).

However, the following problems are encountered when employing polysilicon for monolithic resistors:

1) the sensitivity of polysilicon resistivity to the doping concentration is very large, especially in the high resistivity range; for example, over the doping level of 5×10^{17} to 5×10^{18} atoms/cm^3, a resistivity change of approximately five decades has been observed (Seto, 1975),
2) the structure of polysilicon and grain size are sensitive to thermal processing steps; in addition, implanted arsenic dopants segregate to the grain boundaries in quantities that are dependent on annealing temperature (Mandurah, et al., 1979),
3) polysilicon shows a very large temperature coefficient, especially in lightly doped samples, for example, a sheet resistance of 1GΩ/□ at 25°C drops three decades when the temperature is elevated to 160°C (Seto, 1975).

3. MATERIALS FOR MEMS

3.1. Polymers for microelectronics

Polymers play a significant role in microelectronics. They are not only found in final products such as housings of components, packaging of IC chips, and intermetallic dielectric layers, but are also used extensively in major processing steps such as resist in microlithography. The microlithography with photoresists is an essential step in the fabrication of microelectronics, and polymers are absolute requirements (Bowden and Turner, 1988; Soane and Martynenko, 1989)

In multiplayer fabrication of IC and LSI, insulation between conducting layers and patterned interconnections between them are indispensable. The most widely used dielectric for insulation is silicon dioxide (SiO_2) deposited by plasma-enhanced chemical vapor deposition (PECVD). Aluminum and its alloys are used to form a conducting layer. As shown in Fig. 3.1, such inorganic thin films with a thickness limited to a few μm or less tend to reproduce the topography of the underlying substrate since they lack any planarizing properties. Problems typically encountered are poor step coverage and thinning of the coating over sharp surface features. Thicker inorganic films are prone to cracking. Poor step coverage ultimately leads to poor line width resolution and long-term reliability problems stemming from cracks and discontinuities in the conducting and insulating layers (Horie and Yamashita, 1995).

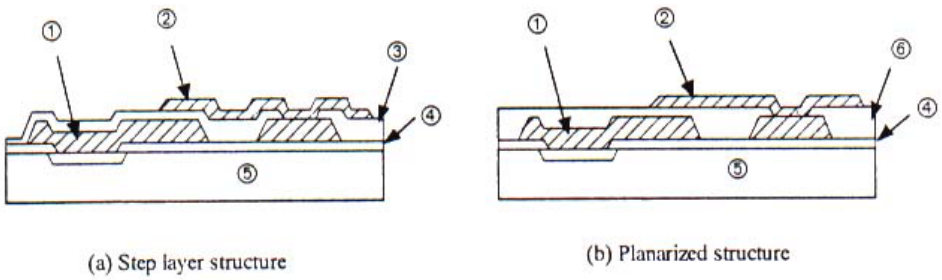

Fig. 3.1. Structures of multilayer wiring: (1) first aluminum wiring, (2) inorganic insulation layer, (4) SiO_2, (5) silicon, (6) polyimide insulating layer (Horie and Yamashita, 1995).

One active area of research is in the replacement of the SiO_2 inorganic insulating layer with polymeric dielectrics. Amongst organic materials, the high demands on thermal and mechanical properties have, until now, been best met by polyimides. Their high electric resistivity, high breakdown voltage, low dielectric constants, and ease of processing make organic polymers particularly suitable as insulating layers in multilevel interconnections. In the case of polyimides, the planarization as shown in Fig. 3.2 can be attained by spinner coating of their precursor poly amicacids and successive thermal imidization. Polyimides have another important advantage of high thermal stability. Thus, polyimides rapidly became of general interest in the field of electronics (Horie and Yamashita, 1995).

3.1.1. Polyimides as a sensitive layer

Polyimide was originally developed for use in electronic industries as an interlevel dielectric, stress buffer, passivation layer, and alpha particle layer (Khan, et al., 1988; Horie and Yamashita, 1995). Important parameters of polyimides include those

related to planarization, thermomechanical and electrical properties, stress, adhesion, resistance to solvents, hysteretic, long-term stability, accuracy, and sensitivity.

Polyimides have been well studied for use in humidity sensors for several reasons (Denton, et al., 1985, 1995; Ralston, et al., 1995; Ralston, et al., 1990):

1) they have high thermal stability at temperatures greater than 400°C,
2) they are fully compatible with silicon processing technology,
3) they have a high sensitivity to humidity, their dielectric values change from about 3.0 to 4.2 as relative humidity changes from 0% RH to 100%RH, they absorb a lot more water than ceramic oxides, about 3% by weight on the average, leading to changes in bulk properties,
4) their response to humidity change is linear, in contrast to ceramic oxides,
5) the diffusion constant is often very large, leading to fast response time,
6) they also absorb water reversibly with little or almost no hysteresis,
7) they have a good resistance to chemical corrosion (Delapierre et al., 1983).

Usually, polyimides are insoluble. They can, however, be applied to substrate as a relatively high coating thickness, for instance, via spin coating of a soluble precursor followed by a tempering step, in order to obtain polyimide. Such layers can be patterned photo-lithographically by using a photoresist, Fig. 3.2 (left). In this case, the photo-patterned resist layer acts as a mask for the lower polyimide layer (indirect patterning). Apart from the large number of processing steps involved, there is a problem, because undercutting of the polyimide layer to be patterned could result due to its solubility during the wet development process. This has proved to be unfavorable, not only with

respect to the reproducibility of the whole process, but also especially regarding the resolution capability. Polyimide precursors or soluble polyimides that possess photoresist properties Fig. 3.2 (right) provide higher yields at lower cost because of fewer and safer processing steps. They can easily be employed in common photo techniques. Just as in the case of conventional photoresists of the negative type, light exposure through a mask gives rise to large solubility differences by crosslinking in the exposed area directly in the layer to be patterned, i.e., direct patterning (Horie and Yamaskito, 1995). This is important for high resolution. After development with a solvent and subsequent curing, appropriate polyimide patterns for the described application result. Polyimides can be divided into two groups:

1) non-photosensitive,
2) photosensitive.

Non-photosensitive polyimide should be patterned by dry or wet etching using a photoresistive layer as a mask so that additional process steps of spin-coating and patterning of photoresist are required. Using photosensitive polyimide just two process steps are required: exposure to ultraviolet, and development. Since the photosensitive type needs considerably fewer processing steps than for the non-photosensitive type, this type of polyimide is selected for use as the sensitive layer in a humidity sensor.

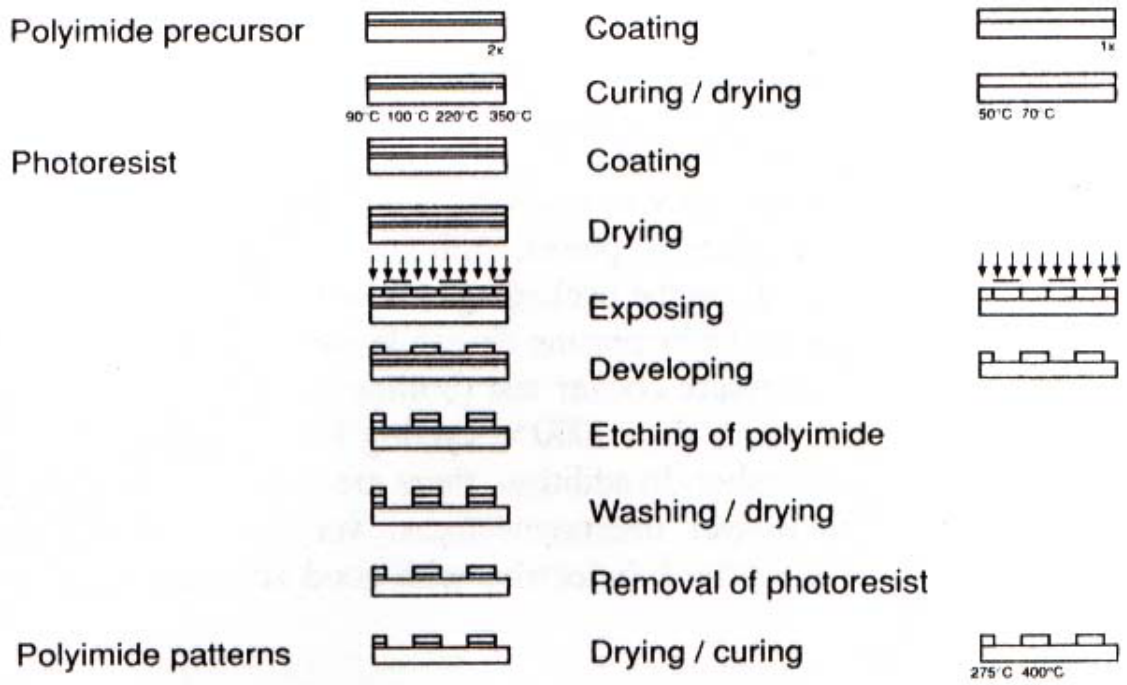

Fig. 3.2. Indirect patterning of polyimides (left) versus direct patterning with photosensitive polyimide precursor (right) (Horie and Yamashita, 1995).

3.1.2. Photosensitive polymers

Photosensitive materials utilize the changes in physical properties due to chemical reactions induced by irradiation with ultraviolet or visible light. Photosensitive polymers are defined as polymers whose photosensitive groups perform crosslinking, chain scission, or other chemical reactions under the light irradiation, leading to the changes in various physical properties such as solubility, adhesive strength, softening point, or the change from liquid to solid and vice versa (Reiser, 1989). By the end of the 19th century, photosensitivity of diazo-compounds and photodimerization of cinnamic acid were already known. However, the modern technology of photosensitive polymers began in 1930 with the discovery of photoresists by the photo-crosslinking of unsaturated ketones.

In 1948, Minsk and van Deusen (1948) at Eastman Kodak reported poly-vinyl- cinnamate as a photosensitive polymer using photodimerization of cinnamate groups. This polymer was prepared from the reaction of poly vinyl alcohol with cinnamoyl chloride.

3.1.3. Commercially available photosensitive polyimides

In order to save processing steps and, simultaneously, to produce high solubility differences in the polyimide layer to be patterned (as with a photoresist), attempts were made to develop photosensitive polyimides. The first approach was made more than twenty years ago by Kerwin and Goldrick (1971). They used soluble polyamic acids as polyimide precursor and chromium salt additives as photosensitizers. This system did not become commercially viable due to the inorganic metal salts and the low shelf life. Photoresists, which, after photolithographic processing remain in electronic component as a durable protection and insulation layer, must fulfill particularly stringent demands with regard to purity (especially concerning metal-ionic impurities) in order to avoid problems with leakage currents, doping, and response curve shifts in the components. In the meantime, nearly all of the known principles of photoresists have been adapted to the design of photosensitive polyimides. Yet only a few types are commercially available now and are therefore important for practical applications in electronics. These are of the negative type, based on polyamic acids with ester- or salt like bound photo-cross linkable groups in the side chain (Horie and Yamashita, 1995).

3.1.3.1. Polyamic acid methacrylic ester

Rubner, et al., (1974) invented the first entirely organic photoresist to create polyimide patterns. It is based on ester-type, photoreactive polyimide precursors and is especially suitable for applications in microelectronics by providing a low level of metal ions. The starting material is the highly soluble polyamic acid methacrylate ester as phot-crosslinkable polyimide precursor, which can be converted to the polyimide by thermal treatment, Fig 3.3. Just like a conventional photoresist, the solution of a polyimide precursor is deposited, together with photoinitiators, on the substrate by spin coating, spraying, etc., and is then dried. The resulting film is exposed through a mask. The photo-crosslinking that takes place via the photoreactive groups R* gives rise to a large solubility difference between the exposed and unexposed regions of the layer to be patterned, thus allowing the following developing steps to be carried out safely and reproducibly. By extracting the still soluble regions with an organic solvent in the shadow of the mask, high-resolution patterns are obtained, which are finally converted into the polyimide by tempering. At the same time the crosslinks de-polymerize to produce the alcohol that had originally been integrated into the soluble polyimide precursor as a photosensitive ester group. As already pointed out, in all applications, the curing conditions are especially important for producing fully imidized polyimides, which have to withstand harsh test conditions and provide long-term properties.

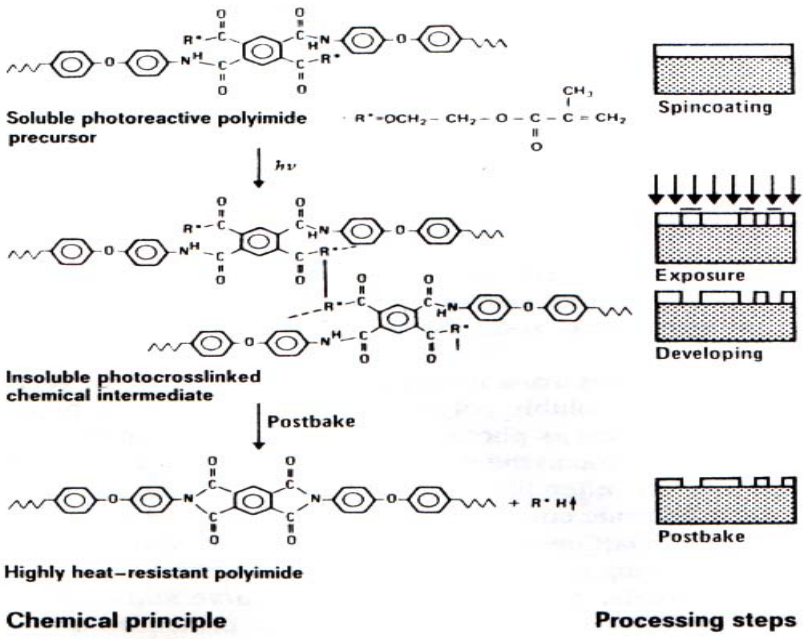

Fig. 3.3. Chemical principle and processing steps for direct production of Pi-patterns starting from polyamic acid methacrylatester (Rubner, et al., 1974).

3.1.3.2. Polyamic acids with ionic bound photo-cross linkable groups

Yoda and Hiramoto (1984) reported a simple procedure to get a polyamic acid solution photosensitive by adding photoreactive tertiary amines containing an acryloyl or methacryloyl group and a sensitizer. This led to a salt-like interaction between the amino groups and the carboxylic acid groups of the polyamic acid. The photoreaction has been discussed in details by Tomokawa, et al., (1992). Figure 3.4 shows the basic chemical components of this system. In this case, there is an easy chlorine-free access to the photosensitive polyamic acid as polyimide precursor.

Compared to the photosensitive polyimide precursors with ester-like bound photoreactive groups, the difference in solubility between exposed and nonexposed areas is less pronounced. The developing process is thus more critical. The resulting patterns

have good mechanical properties (Torary, 1992; Hiramoto, 1990). Materials based on this chemical principle are commercially available from Toray under the trademark "photoneece." These include recently improved materials with high-resolution capability and low thermal expansion coefficient: UR-5100 type (Asano, et al., 1993).

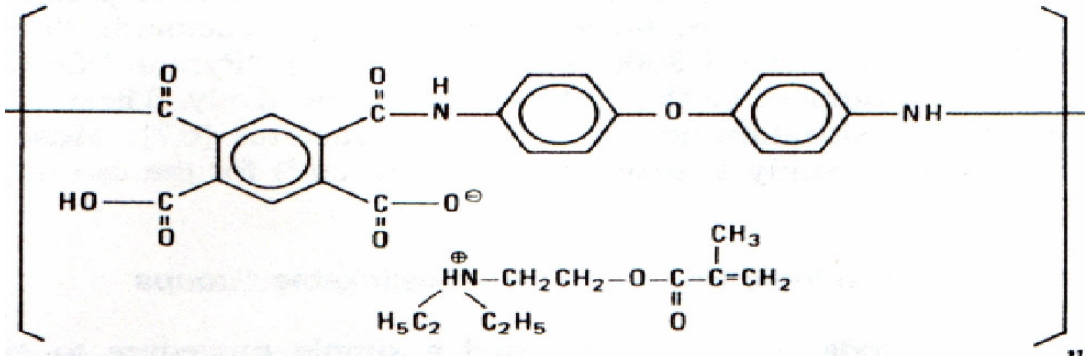

Fig. 3.4. Polyimide precursor with salt-like bound photoreactive group (Horie and Yamashita, 1995).

3.1.4. Discussion of performance of commercial photosensitive polyimides

3.1.4.1. Thermomechanical properties

The trend in the development of new photosensitive polyimides is towards polymers, which minimize stress, show high elongation before breaking and good adhesion. The film-induced stress of the substrate can be measured by wafer deformation.

Low shrinkage due to curing, as in the case of "probimide 400," does not seem to be a relevant parameter to minimize stress, since a relatively high stress to be a relevant parameter to minimize the stress, since a relatively high stress of 46 MPa is involved with "probimide 400," compared with ester and salt-like type precursors, which exhibit the

lowest stress value of about 10-25 MPa, Tables 3.1 and 3.2. The crosslinked structure of the autophotosensitive polyimide may be the reason for the high stress. In the case of polyimides derived from a precursor, the crosslinked network is destroyed during the curing cycle, which allows the polymer to relax at curing temperature above T_g (softening point). Also, a linear correlation between the modulus of elasticity and the coefficient of thermal expansion (CTE) is found for polyimide films, in which a high value of the modulus corresponds to a low CTE (Matsuoka, et al., 1991). Therefore a high value in the modulus of elasticity can help to reduce stress and, if combined with a high tensile strength and elongation at break, satisfactorily tough materials may be obtained.

For nonphotosensitive polyimides, it is known that stiff linear polymers have a relatively low coefficient of thermal expansion (Numata, et al., 1986; Ree, et al., 1991), which is important in reducing the misfit in thermal expansion between polyimide and substrate. This principle has also been used for photosensitive polyimides in order to reduce the stress. The development in the polyimide generations is exemplified by the Dupont product line. From the first to the third generation, Fig 3.5, the more flexible benzophenon-tetracarboxylic-dianhydried and oxydianiline (type 2) have been replaced by the rigid biphenyl-tetracarboxylic-dianhydried and p-phenylene-diamine (type 3) (Nader, et al., 1991). The latter polymer type shows a significantly lower wafer deformation than the first type due to its lower coefficient of thermal expansion.

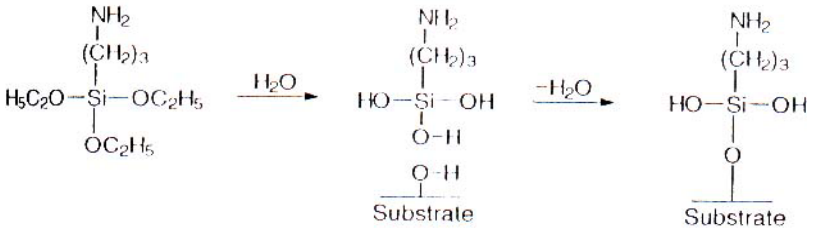

Fig. 3.5. Mechanism of coupling reaction between adhesion promoter (amino-organosilane) and silicon surface (Horie and Yamashita, 1995).

Table 3.1. Mechanical and electrical properties of commercially available photosensitive polyimides.

Material	Mechanical properties				Electrical properties		
	Tensile strength (MPa)	Elongation (at break) (%)	Modulus elasticity (Gpa)	Stress (MPa)	Dielectric constant (1kHz)(0%rh)	Loss factor (1kHz)*10^{-3}	Water update % (50%rh, 24 h RT)
G-7621A[a]	>150	>30	3.3	40-50	3.3	3	0.8
TL-530A[a]	>200	>15	6	10-20	3	2	0.8
I-8320A[a]	>130	>50	2.8	40	3.4	2	0.8
MX-91C2[a]	>140	>30	3.5	30	3.3	2	0.9
PI-2722[b]	175	10	3.8	39.2	3.3	2	2.1
PI-2732[b]	192	8	6	13.5	2.9	-	1.5
Prob. 7500[c]	160	45	3.3	33	3.2 (1 MHz)	3	1.1
Prob. 7000[c]	166	48	2.97	30	3.2(1 MHz)	4	1.25
UR 3800[d]	145	30	3.4	-	3.3	2	1.1
UR 5100[d]	200	>20	2.1	-	3.2	2	-
Prob. 400[c]	147	56	2.9	48	2.9	6	2.5
Ultr. 7501[e]	-	65	3.5	-	2.8	4	3.4

a Pimel/Asahi Chemical
b Pryalin/Du Pont
c Probimide/OCG
d Photoneece/Toray
e Ultradel/Amoco

Table 3.2. Patterning and thermal properties of commercially available photosensitive polyimides.

Material	Type	Exposure Dose (mJ/cm^2)	Curing Temp (°C)	Thickness Loss (%)	Aspect Ratio (cured)	Tg (°C)	Thickness (cured)	CTE (ppm/°C)
G-7621A[a]	ester	300	350-400	50	>0.7	355	5	40-50
TL-530A[a]	ester	200	450	50	>1	None	5	10-20
I-8320A[a]	ester	300	330-400	40	>0.7	280	5	50
MX-91C2[a]	ester	400	350-400	50	>0.8	-	10	35
PI-2722[b]	ester	300	350-400	50	0.5	>320	5	46
PI-2732[b]	ester	150-200	350-400	50	0.5	>400	5	13
Prob. 7500[c]	ester	100-180	350	40	0.6	285	5.7	55
Prob. 7000[c]	ester	150-220	350	40	>1	380	5.9	30
UR 3800[d]	salt	250	-	40-50	-	280	-	45
UR 5100[d]	salt	150-250	350-400	50-62	1	None	-	20
Prob. 400[e]	polyim	600-700	350	5-9	0.7	357	5	37
Ultr. 7501[e]	polyim	230	350	8	>1	>400	5	-

a Pimel/Asahi Chemical
b Pryalin/Du Pont
c Probimide/OCG
d Photoneece/Toray
e Ultradel/Amoco

3.1.4.2. Adhesion properties

Low stress materials with high elongation are prerequisites to avoid cracks. Moreover, excellent adhesion of the polyimide to metals (and vice versa) and to the cured polyimide film beneath is important as well. Difficulties arise in meeting both demands, i.e., good mechanical properties and good adhesion, since polyimides with rigid and linear molecular structure show low stress but have weaker adhesive forces than flexible ones, which, in turn, have poorer mechanical properties (Numata, et al., 1991).

Adhesive forces can be increased by using special adhesion prompters for various kinds of polyimides and substrates (e.g., amino-organosilane), the mechanism of the coupling reaction between the adhesion promoter and the silicon surface is shown in Fig. 3.6, or by plasma treatment of the substrate surface. Some new types of commercially available polyimides already contain an integrated adhesion promoter:Pimel G-X Grade (Asahi, 1994), Pyralin PI 2700 (DuPont, 1994), and probimide 7000, 7500 (OCG, 1994). "Photoneece UR-5100" provides the NMD-3 developer and oxygen plasma (Toray, 1992).

Normally, the exposure of polyimide layers to water at elevated temperatures lowers the adhesion of polyimides, because water can hydrolyze chemical bonds between the polyimide and the substrate surface. Recently, the adhesive forces have been significantly improved. New generations of polyimides have passed the tape test, even when wafers coated with the polyimide on a silicon nitride surface were boiled at 121°C and 2 atm for 400 hr (DuPont, 1994) and 500 hr (Asahi, 1994; OCG, 1994). Excellent adhesion strength values of up to 70 MPa have been reported (Asahi, 1994). Of course, these data depend on the interface polyimide/substrate.

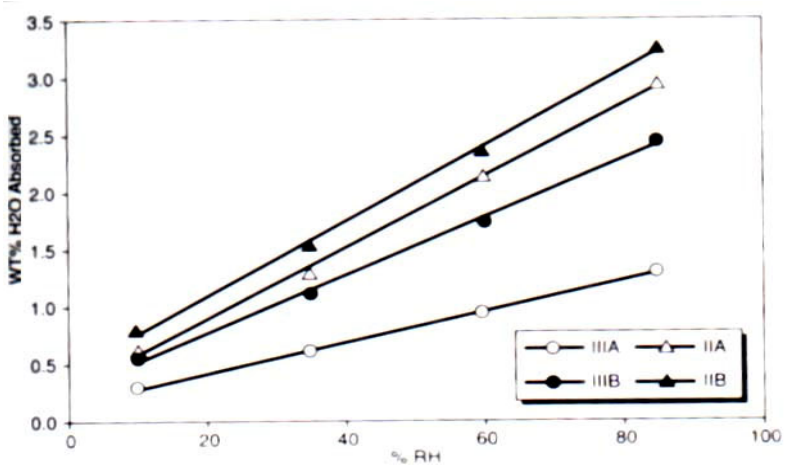

Fig. 3.6. Water absorption of polyimide films derived from (a) nonsensitive (b) photosensitive polyimide precursors II and III as a function of relative humidity (% RH) (Horie and Yamashita, 1995).

3.1.4.3. Electrical properties

The dielectric constant (DC) is the critical parameter for polyimides used in multilevel interconnects. A lower DC will allow a higher packing density at the same impedance and operation at higher frequencies due to lower line capacitance. The DC values of commercially available photosensitive polyimides range between 2.8 and 3.5, Table 3.2. Rigid polyimide polymers that are designed for a low CTE are orientated in the wafer plane by spin coating and curing and, therefore, show anistropic dielectric properties, i.e., DC equal to 2.9 (vertical) and 3.9 (lateral), and refractive index values (Noe, et al., 1991). This should also apply for photosensitive, low CTE polyimides but has not been investigated extensively. The values given in Table 3.2 may therefore be valid only in a lateral or vertical direction, depending on the measuring method. The data were collected at 0% RH. Since polyimides take up water (which has a very high DC of

78) from the moisture of the air, these data are only relevant for polyimides as dielectrics in a device that has been sealed after final curing. In general, the DC can be reduced by incorporating fluorinated groups or siloxane units into the polymer backbone (Hougham, 1991). For fluorine-containing polymers, a compromise is necessary with respect to the adhesion properties and the wet ability with the developer in the lithographic patterning process.

In addition, thermomechanical properties suffer if too many fluorinated or siloxane units are present in the polymer. As an advantage, the water uptake can be reduced by these hydrophobic units. The loss factor is an important indicator for the overall electrical power loss. The dielectric strength (breakdown voltage) is decisive for insulation layers in power electronic devices. As shown in Table 3.2, the loss factor and breakdown voltage of most of the commercially available materials fulfill today's requirements.

3.1.4.4. Water uptake and solvent resistance

As mentioned above, water uptake mainly affects the dielectric constants (DC) of the polyimide film due to the high value of DC for water equal to 78. From 0% RH to 100% RH, the water uptake increases linearly from about 3% to 4%. Densely packed polymers with a low CTE show a lower water uptake (about 1%) and, therefore, a lower change (up to only 3.3%) in DC.

Most of the water can be released again via an additional baking process; However, for polyimides, this process is not totally reversible. Some of the water can be

consumed irreversibly by hydrolysis reactions of the polyimide (Hammerschmidt, et al., 1989; De Souza-Machado, et al., 1991). Water uptake also affects the mechanical properties and can cause stress relaxation. This fact has been used to estimate the diffusion coefficient of water in the polyimide films, which range from 3×10^{-8} to 5×10^{-9} cm^2/sec, depending on the type of polyimide (Ree, et al., 1991). In the fabrication of multilevel interconnects, bake-out cycles are used to keep water out of the component during processing before encapsulation.

Depending on the chemical structure of the polyimide, the dissipation factor can also be affected by water uptake. Especially in the case of polyimides derived from photosensitive precursors, the change of the dissipation factor increases with humidity (Hammerschmidt, et al., 1989).

When polyimides are applied as dielectrics in multichip modules or other multilevel interconnects with several stacked layers of metal and polyimide, the residual tensile stress in the part increases with each layer and each curing cycle due to the thermal expansion mismatch, and this can result in cracks. When a new layer of polyimide is spin-coated on top of a polyimide layer already cured (with or without metal lines inside), the solvent of the top layer penetrates the underlying layer to some extent (Cech, et al., 1991). This exposure of the cured underlying polyimide layer to solvents (in most cases, N methyl-pyrrolidone) can induce crack growth as well (Hu, et al., 1991). Crack growth depends on the pre-strain in the polyimide film, which is exposed to solvents. Solvent incorporation reduces the stress because it acts as a plastifier that makes relaxation of the stress possible or it causes cracks in the film. The inertness of

polyimides towards solvents or water, with respect to crack-free films and good adhesion, can be quite different. Often, densely packed rigid linear polymers are most inert towards such chemicals.

3.1.4.5. Planarizing properties

When photosensitive polyimides are used as an insulating layer for multilevel interconnections, the two main functions of these layers are to planarize the underlying topography and to produce a low dielectric constant for high switching speed. After spin-coating of the precursor or polyimide and soft bake, the degree of planarization (DOP) (Day, et al., 1984), Fig 3.7, is a function of the pattern width. Even in the ideal case of 100% planarization after soft bake, there will still be a limited DOP after curing, especially in the case of the photosensitive polyimide precursor with its high layer shrinkage. This is due to the fact that the absolute shrinkage differs because there is a thin polyimide layer on top of metal conductors and a higher thickness between the metal lines. Systems with low shrinkage during the curing cycle, such as photosensitive soluble polyimides, show better planarization. There is very little data available on planarization properties of photosensitive polyimides. A comparison between the ester-like photosensitive polyimide precursor HTR 3-50 (OCG) with 50% shrinkage and a 6F polybenzoxazol (6F-PBO) precursor with 30% shrinkage exhibits a significantly better planarization of the material with the lower shrinkage (DOP: 35% for HTR –3 and 60% for 6F-PBO) for 4 μm spaces between 1.3 μm high aluminum steps (Rubner, et al., 1990). The molecular weight (M_n) affects the DOP as well: the lower the molecular

weight, the better the planarization (Day, et al., 1984). On the other hand, a low M_n is accompanied by a relatively high coefficient of thermal expansion (Matsuoka, et al., 1991), which should be avoided with respect to the formation of stress.

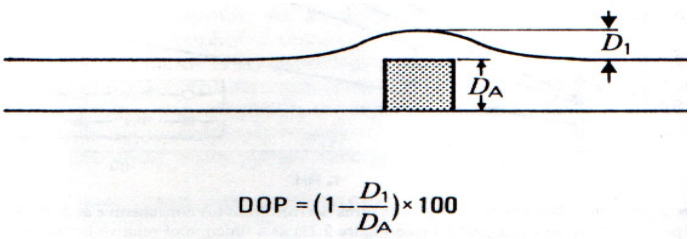

Fig. 3.7. Schematic diagram of planarization of a metal line (Horie and Yamashita, 1995).

3.1.5. ULTRADEL 7501 properties

Proper choice of the sensing material is very important since it determines many performance aspects of the humidity sensor. A preimidized photosensitive polyimide (Amoco, 1992) has been used as the moisture sensing material in this thesis. A preimidized film has been chosen to reduce any stress build-up between the upper electrode and the polyimide induced during the curing cycle. This type of polyimide shrinks in thickness by only about 8% after curing, while polyimide precursors shrink by as much as 50%. Photosensitivity is necessary for forming the suspended top-electrode structure. ULTRADEL 7501 has a tensile modulus of 510,000 psi, a thermal expansion coefficient at 200°C of 24 ppm/°C, and a moisture uptake at 0% and 50% RH are 2.8% and 3.4%, respectively. Therefore, ε_r is 2.8 and 4 at 0% and 100% RH, respectively.

3.1.6. Moisture sorption and transport in polyimides

Moisture absorbed in a material modifies many physical material-properties, including the dielectric constant, conductivity, modulus, impact strength, ductility, and toughness. The dielectric constant is significantly influenced by moisture absorption since water has a relative large dielectric constant of 80. Moisture is exchanged between the material and the environment until a steady state is reached. In steady state, the net gain and loss of moisture becomes zero. The equilibrium moisture content is a function of humidity, temperature, type of material, and the moisture history of the material.

The absorbed water in a material exists in several different forms: chemisorbed, physisorbed, and condensed states. In the first state, water molecules are chemically bound to the constituents of the material; in the second state, they are held by surface forces; and in the third state, water is condensed inside small pores present inside the material (clustering). The radius of the pores (r_k) below which water condenses is given by the equation

$$r_k = \frac{2\gamma M_n}{\rho RT \ln\left(\frac{p_s}{p}\right)} \quad , \tag{3.1}$$

where γ, M_n, ρ, R, T, p_s, and p are the surface tension, molecular weight of water, density, universal gas constant, temperature, saturated water vapor pressure and the water vapor pressure, respectively (Traversa, 1995).

In polyimides, water molecules are either chemically bound to the polymer matrix or are condensed in microvoids, depending on the humidity level. Figure 3.8 shows

possible bonding sites for water molecules in polyimides; they are bound either to the carbonyl group or to the oxygen of the ether linkage (Melcher, et al., 1989).

It has been shown by measuring the equilibrium moisture content in a material as a function of the water vapor pressure (the plot of this measurement result is called the equilibrium moisture content isotherm) that moisture starts to condense as the relative humidity level becomes higher (Yang, et al., 1985, 1986). Experimental results show that the isotherm curve is concave with respect to the vapor pressure axis at the lower vapor pressures while it is convex to the axis at higher pressures. The transition from the concave to the convex form is explained to be due to clustering of water molecules inside the material; the transition point at which moisture clustering starts to occur, which depends on the material and the temperature. Moisture transport inside a material occurs not only by diffusion but also by reaction. At higher temperature, however, reaction occurs at a very slow rate so that the transport due to this mechanism can be neglected. In the temperature range at which humidity sensors are normally operated (>-50°C), moisture transport is due to diffusion through the microvoids.

3.2. Polysilicon films

3.2.1. Preparation of polysilicon films

Polysilicon films are generally prepared by either vacuum evaporation of silicon on heated substrates (Mountvala and Abowitz, 1965; Collins, 1961; King, et al., 1973) or chemical vapor deposition (CVD) (Kamins, 1974; and Seto, 1975).

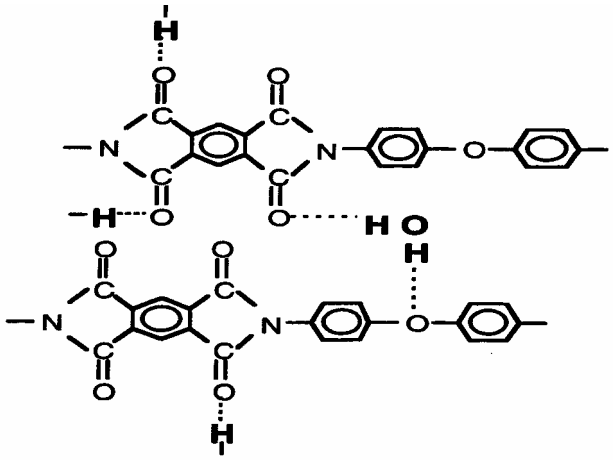

Fig. 3.8. Possible bonding sites in polyimides for water molecules (Melcher, et al., 1989).

Because of better quality and uniformity, most of those found in commercial applications are deposited by CVD where a silicon-containing gas is reduced or decomposed near the structure of a heated substrate. The substrate can be amorphous (such as SiO_2 or Si_3N_4) or crystalline such as silicon or sapphire (Al_2O_3). The deposition temperature is critical because, at a deposition temperature on the order of 1000°C to 1300°C, the silicon layers deposited on single-crystal silicon become epitaxial single crystals and, if lowered to 600°C and below, they become polycrystalline; layers deposited over amorphous substrates are amorphous below 600°C and become polycrystalline above 600°C (Kamins, et al., 1978).

The silicon containing gas comprises only a small fraction of the total flow, most of which is composed of an inert carrier gas such as hydrogen, nitrogen, or argon. The deposition temperature can be varied from 600°C to 1250°C, depending on film thickness and applications. Because of the limited loading capacity inherent in horizontal

deposition systems, systems operating at low pressure (a fraction of a Torr) are preferred because the wafers are placed vertically which greatly increases capacity.

The physical and electrical properties of films deposited under low pressure have been studied (Mandurah, et al., 1979; Kamins, et al., 1978) and compared to those deposited at atmospheric pressure. The electrical properties of both were found to be similar. However the grain size is smaller in films deposited at low-pressure CVD temperatures (which never exceed 800°C) and the deposition rate is also slower. Depending on the polysilicon film application, the polysilicon film can be deposited on the substrate by atmospheric or low pressure CVD.

3.2.2. Polysilicon structure

Polysilicon material is composed of crystallites joined together by grain boundaries, and it is a three-dimensional material with grains having a wide distribution of sizes and irregular shapes, Fig 3.9. Inside each crystallite, atoms are arranged in such a way that it can be considered as a small single crystal. The boundary region consists of layers of disordered atoms that represent a transitional region between different orientations of neighboring crystals.

The grain structure, size, and orientation of polysilicon films are dependent on the deposition conditions (Kamins and Cass, 1973), subsequent doping, and thermal steps (Wada and Nishimatsu, 1978). Surface topology can be examined via scanning electron microscopy (SEM) and grain size (normally very small—from angstroms to microns) is best analyzed through transmission electron microscopy (TEM) (Hirch, et al., 1965). For

example, a schematic of compressive poly-Si formed at 620°C-650°C is shown in Fig. 3.10. The columnar coarse-grain structure arises from a process of grain growth competition among the small grains, during which the grains preferentially oriented for fast vertical growth survive at the expense of disoriented, slowly growing grains (Krulevitch, 1994).

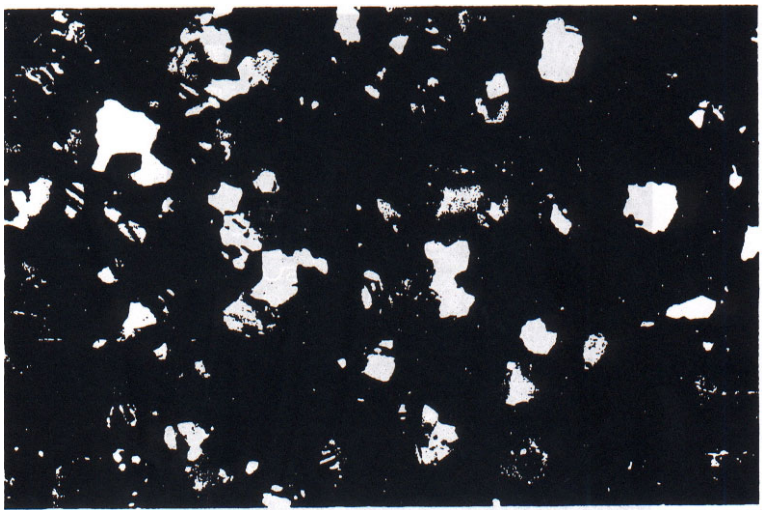

Fig. 3.9. Dark-field TEM of a 1 μm polysilicon film. The grain configuration in certain crystal orientations is well defined (Lu, 1981).

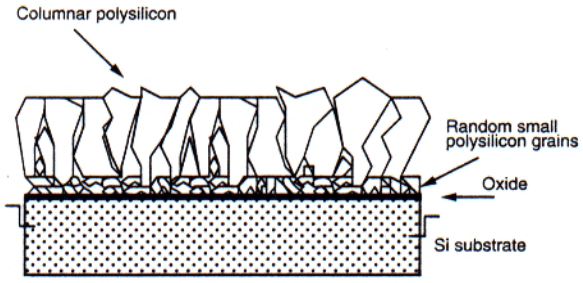

Fig. 3.10. Schematic of compressive poly-Si formed at 620°C to 650°C (Krulevitch, 1994).

3.2.3. Electrical properties of polysilicon film

The electrical properties of polysilicon films are shown in Fig. 3.11, (Gerzburg, 1979; Seto, 1975). When the doping concentration increases, resistivity drops and carrier concentration increases, Fig. 3.11a. A sharp change occurs at intermediate dopant levels. In Fig. 3.11b, carrier mobility is at a minimum near the same dopant levels, which differs considerably from the properties of single-crystal silicon where mobility decreases monotonically and resistivity and carrier concentration vary more gradually as the doping concentration increases. At any dopant level, polysilicon resistivity is consistently higher than that in a single-crystal silicon.

Two models are used to explain the effect of a grain boundary on the electrical properties of doped polysilicon films.

The first is a dopant-segregation model wherein the grain boundary serves as a sink for the preferential segregation of impurity atoms that become inactive at the boundary (Cowher and Sedgwick, 1972). As the dopant concentration increases, the grain boundaries begin to saturate and the dopant atoms diffuse into the bulk of the crystallites. As a result, carrier concentration increases rapidly and resistivity drops sharply. A further rise in the doping level causes a proportional increase in carrier concentrations and a reduction in resistivity. This model alone, however, cannot explain the mobility minimum at the critical doping level, the temperature dependence of resistivity, and the large-signal I-V behavior.

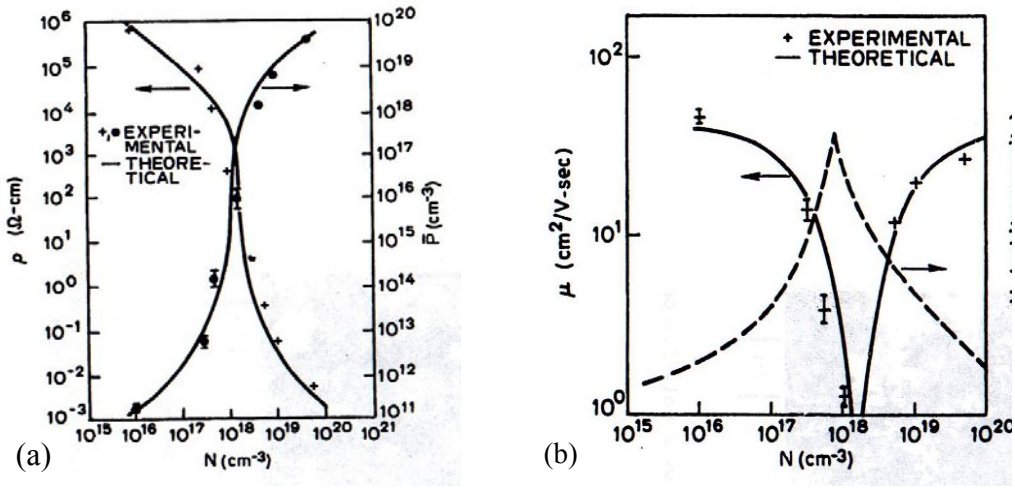

Fig. 3.11. Electrical properties of 1 μm polysilicon film (Seto, 1975): (a) carrier concentration and resistivity as a function of dopant concentration (b) carrier mobility and barrier potential as a function of dopant concentration.

The second is a carrier-trapping model (Seto, 1975; Kamins, 1971; Baccarani, et al., 1978) wherein the grain boundary contains trapping states caused by defects resulting from disordered or incomplete atomic bonding. These states trap part of the carriers from the ionized and uniformly distributed dopants. This process not only reduces the number of carriers but also creates a potential barrier as a result of the electrically charged traps which impede the motion of carriers from one crystallite to another. At a low dopant level, most of the carriers are trapped. As the doping concentrations become denser and most of the trapping states are filled, carrier concentration increases rapidly and resistivity drops sharply. Although a local minimum is also observed in carrier mobility at the maximum potential barrier in this transition region, its change is smaller than that of the carrier concentration by approximately six orders of magnitude. Above this doping level, the potential barrier decreases and resistivity is gradually reduced. This model explains better the sharp changes in resistivity versus doping level, mobility minimum,

and temperature dependence, and the I-V characteristics. Even if the dopants do segregate, the trapping model can still be applied, based on an activate-dopant concentration that can be obtained by subtracting the inactive-dopant concentration from the implanted concentration (Mandurah, et al., 1979). The validity of carrier trapping is maintained by selecting boron as the dopant as well as optimal processing conditions to minimize segregation.

3.2.4. Processing conditions and existing data for polysilicon resistors

The processing parameters that ensure good control and reproducibility are discussed in this section. By comparing the sharp variation of resistivity versus doping concentration in polysilicon to the gradual change in single crystal silicon, resistivity dependence on the doping level in polysilicon is expected to approach that of single-crystal silicon by demonstrating less sensitivity as grain size increases (Gerzberg, 1979; and Lu, et al., 1980). High deposition temperatures or the deposition of thick film can result in a large grain size. However, acceptable surface roughness and the need for high lithography resolution, and smaller device geometry limit the maximum grain size. Other device-processing constraints dictate the highest deposition temperature. The effect of grain size on the ρ versus N curve are investigated here, based on published data (Mandurah, et al., 1979; Seto, 1975) for 1.0 μm and 0.67 μm polysilicon layers with grain sizes of 230 Å and 420 Å and deposited at 750°C and 960°C, respectively, and on data obtained from Lu, et al., (1981) for 1.0 μm and 5.0 μm films deposited at 1050°C and with grain size of 1 μm.

The columnar structure of polysilicon, Fig 3.10, increases the diffusivity of dopants to a much higher degree than does single-crystal silicon (Kamins, et al., 1972). Because the diffusion process strongly depends on grain structure and deposition temperature, doping polysilicon with a diffusion source is difficult to control. Better control is achieved by dopant ion implantation (Seto, 1975) through an oxide layer on top of the polysilicon to avoid loss of dopants during subsequent thermal steps. High-temperature post implantation annealing activates and redistributes the dopants uniformly throughout the film immediately after implantation. It was also observed that the sensitivity of grain growth to annealing temperature is reduced substantially at 1000°C or higher (Wada and Nishimatsu, 1978) and it is also related to deposition temperature. The initial grain size of polysilicon deposited at 600°C to 900°C is small and significant variations in structure and dimensions occur during thermal steps at higher temperature (Mandurah, et al., 1979). However, a high deposition temperature produces relatively large grains that are unlikely to change during thermal annealing and, therefore achieves better stability and control.

Dopant segregation at grain boundaries is undesirable for good resistivity control. Implanted arsenic segregates at annealing temperatures of 800°C to 900°C (Mandurah, et al., 1979). In contrast, the phosphorous and boron dopants in polysilicon deposited at 1225°C do not segregate (Monkowski, et al., 1979). This behavior is explained as follows. At a low annealing temperature of 750°C for 40 min, the diffusion distance of dopants is small and segregation can be minimized (Seager and Castner, 1978). At 800°C to 900°C, this distance becomes larger and, because diffusion along grain

boundaries is higher than in single crystal silicon, segregation may occur. At elevated temperatures, the difference in diffusivities along the boundaries and in single crystals is less pronounced (Distefano and Cuomo, 1977) and, as a result, segregation is minimized. At all annealing temperatures, however, segregation of the boron dopants is least significant compared to phosphorous and arsenic (Mandurah, et al., 1979), and grain growth is much less enhanced (Lu, et al., 1980). Therefore boron dopant was used in this work because of having more stability and less segregation.

The data obtained for polysilicon deposited at different temperatures are plotted in Fig. 3.12 (Lu, 1981). The ρ versus N curve corresponding to the smallest grain is on the right and shifts to the left as size increases. For the smallest grain (230 Å) at a resistivity of 200 Ω-cm, a resistivity change of approximately 67% is observed for a 10% variation in doping concentration which corresponds to a change of 5.4 decades in resistivity for only a 1-decade variation in doping concentration. A more moderate 38% change in resistivity for a 10% deviation in dose of concentration (3.4 decades/decade) is achieved with larger grain polysilicon films formed by a higher deposition temperature. The larger grain sizes are more reproducible and indicate less than a 25% variation in absolute sheet resistance of 2.6 MΩ/□ between wafers.

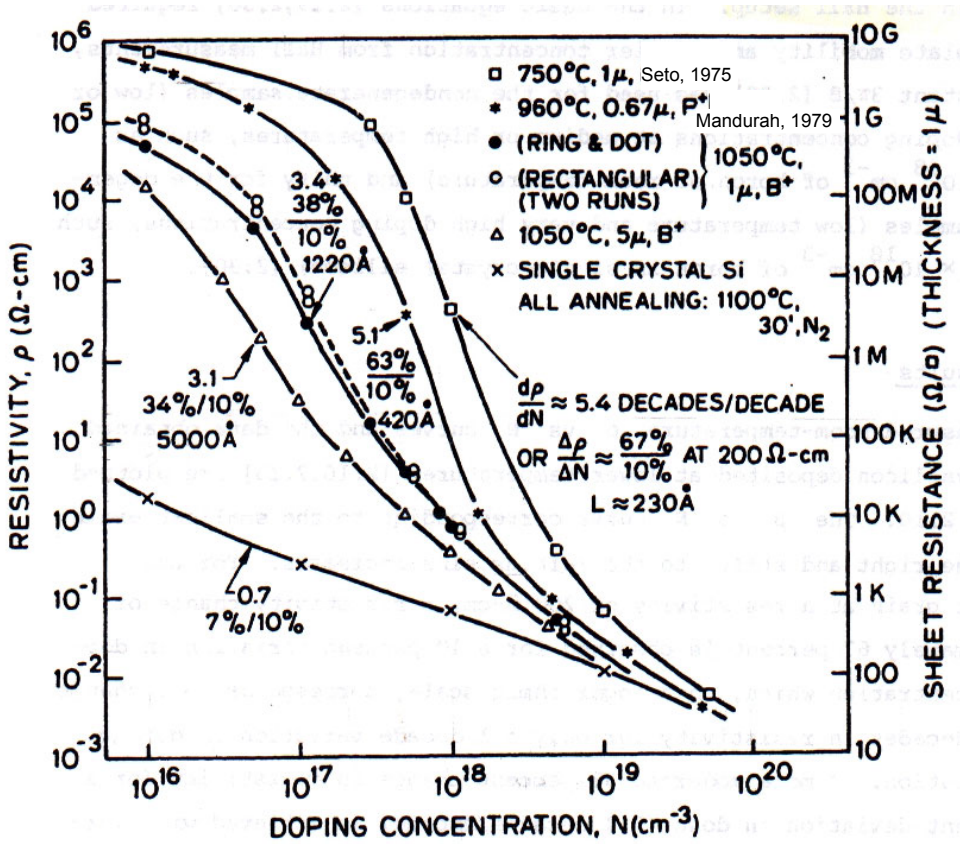

Fig. 3.12. Measured room temperature resistivity versus doping concentration of polysilicon films for various grain sizes. The slope at 200 Ω–cm in each curve is expressed by both decades/decade and percentage change versus 10 percent variation in doping concentration (Lu, 1981).

4. ANALYTICAL CONSIDERATIONS OF MEMS SENSORS

4.1. Pressure sensors

4.1.1. Operation principle of pressure sensors

When a uniform pressure is applied to a silicon microdiaphragm, deflection occurs and the internal strain of the diaphragm changes. Silicon is a piezoresistive material (Smith, 1954) such that its resistance changes when the internal strain varies. If the pressure sensing resistors can be constructed and placed on top of the thin diaphragm, pressure can be measured by monitoring the resistance changes. A Wheatstone bridge circuit has been used to provide voltage outputs for pressure measurement. Four sensing resistors are placed on the diaphragm. A rectangular diaphragm with length to width ratio of 5 is discussed and analyzed. The length and width of diaphragm are 750 μm and 150 μm, respectively.

4.1.2. Diaphragm bending and stress distribution

The fundamental assumptions of the linear, elastic, small-deflection theory of bending for thin plates, which is called the Kirchhoff's plate theory, can be stated as follows (Ventsel and Krauthammer, 2001):

1) The material of the plate is elastic, homogeneous, and isotropic,
2) The plate is initially flat,
3) The deflection (i.e., the normal component of the displacement vector) of the midplane is small compared with the thickness of the plate; the slope of the

deflected surface is therefore very small and the square of the slope is a negligible quantity in comparison with unity,

4) the strain line, initially normal to the middle plane before bending, remains straight and normal to the middle surface during the deformation, and its length is not altered; this means that the vertical shear strains γxz and γyz are negligible and the normal strain εz may also be neglected; this assumption is referred to as the "hypothesis of straight normal,"
5) The stress normal to the middle plane, σz, is small compared with the other stress components and may be neglected in the stress-strain relations,
6) Since the displacements of a plate are small, it is assumed that the middle surface remains unstrained after bending.

The deflection of a flat diaphragm under uniform pressure load can be found by solving the forth-order differential equation

$$\frac{\partial^4 \xi}{\partial x^4} + \frac{\partial^4 \xi}{\partial x^2 \partial y^2} + \frac{\partial^4 \xi}{\partial y^4} = \frac{p}{D} \quad , \tag{4.1}$$

where $\xi = f(x,y)$ denotes the displacement of the natural plane from its original position, p is the pressure loading force in the direction of ξ, and D denotes flexural rigidity of the diaphragm, which depends upon the modulus of elasticity, E, and Poisson's ratio, ν, of the diaphragm material, and the thickness of the diaphragm, h, i.e.,

$$D = \frac{Eh^3}{12\left(1-\nu^2\right)} \quad . \tag{4.2}$$

If Eq. 4.1 is solved for ξ, the strains, ε , in the plate can be calculated using the following expressions:

$$\varepsilon_x = -z\frac{\partial^2 \xi}{\partial x^2} \quad , \tag{4.3}$$

$$\varepsilon_y = -z\frac{\partial^2 \xi}{\partial y^2} \quad , \tag{4.4}$$

$$\varepsilon_z = -z\frac{\partial^2 \xi}{\partial z^2} \quad . \tag{4.5}$$

where x, y, and z represent Cartesian coordinates. Since the strain distribution is known, the stress, σ, in the diaphragm can be calculated as

$$\sigma_x = \frac{E}{1-\nu^2}\left(\varepsilon_x + \nu\varepsilon_y\right) \quad , \tag{4.6}$$

$$\sigma_y = \frac{E}{1-\nu^2}\left(\varepsilon_y + \nu\varepsilon_x\right) \quad , \tag{4.7}$$

$$\tau_{xy} = G\gamma_{xy} = \frac{E}{2(1+\nu)}\gamma_{xy} \quad . \tag{4.8}$$

Since all edges of the diaphragm for pressure sensor are fixed, Fig. 4.1, the boundary conditions are

$$\xi\,|_{x=0,a} = 0 \quad , \tag{4.9}$$

$$\left.\frac{\partial \xi}{\partial x}\right|_{x=0,a} = 0 \quad , \tag{4.10}$$

$$\xi\,|_{y=0,b} = 0 \quad , \tag{4.11}$$

$$\left.\frac{\partial \xi}{\partial x}\right|_{x=0,b} = 0 \quad . \tag{4.12}$$

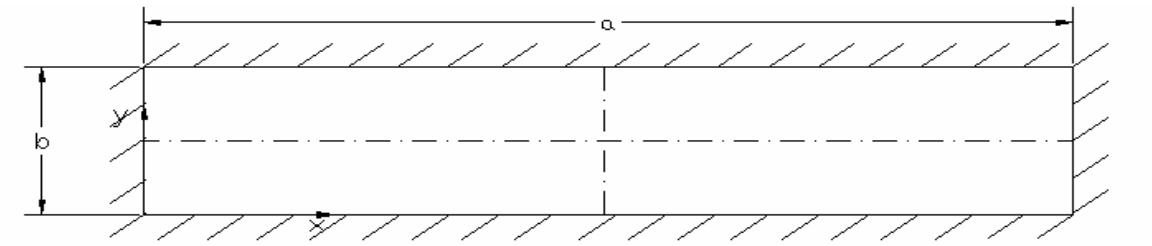

Fig. 4.1. Rectangular diaphragm with all edges fixed.

The differential Eq. 4.1 can be solved using the Fourier series expansion method (Wang, 1953) to obtain

$$\xi = \sum_{m=1}^{\infty}\sum_{n=1}^{\infty} a_{mn}\left(1-\cos\left(\frac{2m\pi x}{a}\right)\right)\left(1-\cos\left(\frac{2n\pi y}{b}\right)\right) \quad , \tag{4.13}$$

where m and n denote number of terms used in determination of deformation of the diaphragm, and a_{mn} are the constant parameters. The constant parameters are determined from the condition that the potential energy of the system, π, defined as a difference between the bending strain energy of the diaphragms, U, and potential energy of the external force, W, i.e.,

$$\pi = U - W \quad , \tag{4.14}$$

is minimum with respect to the parameters a_{mn}. The bending strain energy for this diaphragm is (Timoshenko, 1959)

$$U = \frac{D}{2}\iint\left(\frac{\partial^2\xi}{\partial x^2}+\frac{\partial^2\xi}{\partial y^2}\right)^2 dxdy \quad , \tag{4.15}$$

and if the flat diaphragm is under the action of a uniformly distributed load of intensity p, the potential energy due to the external force is

$$W = \iint P\xi dxdy \quad . \tag{4.16}$$

By substituting Eq. 4.13 into Eqs 4.15 and 4.16, we find that

$$U = \frac{D}{2}\int_0^a\int_0^b \left\{ \sum_{m=1}^{\infty}\sum_{n=1}^{\infty} 4\pi^2 a_{mn} \left[\frac{m^2}{a^2}\cos\left(\frac{2m\pi x}{a}\right)\left(1-\cos\left(\frac{2n\pi y}{b}\right)\right) + \right.\right.$$
$$\left.\left. + \frac{n^2}{b^2}\cos\left(\frac{2n\pi y}{b}\right)\left(1-\cos\left(\frac{2m\pi x}{a}\right)\right)\right]\right\} \quad ,$$

or

$$U = 2D\pi^4 ab\left\{ \sum_{m=1}^{\infty}\sum_{n=1}^{\infty}\left[3\left(\frac{m^4}{a^4}\right) + 3\left(\frac{n^4}{b^4}\right) + 2\left(\frac{m^2}{a^2}\right)\left(\frac{n^2}{b^2}\right) a_{mn}{}^2 + \right.\right.$$
$$\left.\left. + \sum_{m=1}^{\infty}\sum_{r=1}^{\infty}\sum_{s=1}^{\infty} 2\left(\frac{m^4}{a^4}\right) a_{mr}a_{ms} + \sum_{r=1}^{\infty}\sum_{s=1}^{\infty}\sum_{n=1}^{\infty} 2\left(\frac{n^4}{b^4}\right) a_{rn}a_{sn} \right] \right. \quad , \tag{4.17}$$

and

$$W = p\int_0^a\int_0^b \sum_{m=1}^{\infty}\sum_{n=1}^{\infty} a_{mn}\left[1-\cos\left(\frac{2m\pi x}{a}\right)\right]\left[1-\cos\left(\frac{2n\pi y}{b}\right)\right]dxdy = pab\sum_{m=1}^{\infty}\sum_{n=1}^{\infty} a_{mn} \quad . \tag{4.18}$$

The condition of minimum potential energy is

$$\frac{\partial \pi}{\partial a_{mn}} = 0 \quad , \tag{4.19}$$

and therefore Eq. 4.17 gives

$$4D\pi^4 ab\left\{\left[3\left(\frac{m^4}{a^4}\right) + 3\left(\frac{n^4}{b^4}\right) + 2\left(\frac{m^2}{a^2}\right)\left(\frac{n^2}{b^2}\right)\right] a_{mn} + \right.$$
$$\left. + \sum_{r=1, r\neq n}^{\infty} 2\left(\frac{m^4}{a^4}\right) a_{mr}\right\} + \sum_{r=1, r\neq m}^{\infty} 2\left(\frac{n^4}{b^4}\right) a_{rn} - Pab = 0 \quad . \tag{4.20}$$

A code was written, listed in Appendix A, to find the parameters a_{mn} for different values of m and n by using Kramer's method. Correspondingly, the strain at the surface of the diaphragm of a pressure sensor is

$$\varepsilon_x(x,y) = -\frac{4\pi^2 h}{a^2} \sum_{m=1}^{\infty} \sum_{n=1}^{\infty} m^2 a_{mn} \left(1 - \cos\left(\frac{2\pi n y}{b}\right)\right) \cos\left(\frac{2m\pi x}{a}\right) \quad , \tag{4.21}$$

$$\varepsilon_y(x,y) = -\frac{4\pi^2 h}{b^2} \sum_{m=1}^{\infty} \sum_{n=1}^{\infty} n^2 a_{mn} \left(1 - \cos\left(\frac{2\pi n x}{a}\right)\right) \cos\left(\frac{2m\pi y}{b}\right) \quad . \tag{4.22}$$

The stress on the surface of the diaphragm is

$$\sigma_x(x,y) = -\frac{4\pi^2 h}{a^2} \frac{E}{1-\nu^2} \sum_{m=1}^{\infty} \sum_{n=1}^{\infty} a_{mn} \left[m^2 \cos\left(\frac{2m\pi x}{a}\right) + \nu n^2 \cos\left(\frac{2n\pi y}{b}\right) - \left(m^2 + \nu n^2\right) \cos\left(\frac{2m\pi x}{a}\right) \cos\left(\frac{2n\pi y}{b}\right) \right] \quad , \tag{4.23}$$

$$\sigma_y(x,y) = -\frac{4\pi^2 h}{b^2} \frac{E}{1-\nu^2} \sum_{m=1}^{\infty} \sum_{n=1}^{\infty} a_{mn} \left[m^2 \cos\left(\frac{2m\pi y}{b}\right) + \nu n^2 \cos\left(\frac{2n\pi x}{a}\right) - \left(m^2 + \nu n^2\right) \cos\left(\frac{2m\pi y}{b}\right) \cos\left(\frac{2n\pi x}{a}\right) \right] \quad , \tag{4.24}$$

A simplified solution for the maximum stress and deflection of the rectangular diaphragms with all edges fixed is (Roark, 1965)

$$(\sigma_{yy})_{\max} = \beta \frac{pb^2}{h^2} \quad , \tag{4.25}$$

$$(w)_{\max} = -\alpha \frac{pb^4}{Eh^3} \quad , \tag{4.26}$$

where p, b, h and E are the uniform pressure, width, thickness, and modulus of elasticity, respectively. Also, the coefficients α and β are listed in Table 4.1.

Table 4.1. Coefficients for maximum stress and deflection in a rectangular diaphragm.

a/b	1	1.2	1.4	1.6	1.8	2	∞
α	0.0138	0.0188	0.0226	0.0251	0.0267	0.0277	0.0284
β	0.3078	0.3834	0.4356	0.4680	0.4872	0.4974	0.5000

4.1.3. Gauge factor and piezoresistivity

Objects subjected to loads deform. These deformations are represented quantitatively by strains. Strain can be measured by methods as simple as observing the change in the distance between two scribe marks on the surface of a load carrying member, or as advanced as holography (Figiola, Beasley, 1991).

An ideal sensor for the measurement of strain should:

1) have good spatial resolution, implying that the sensor would measure strain at a point,
2) be unaffected by changes in ambient conditions,
3) have a high frequency response for dynamic strain measurements.

A common sensor that nearly attains these ideal characteristics is the bonded resistance strain gauge. Consider a conductor having a uniform cross sectional area, A, and a length, L, made of a material having the electrical resistivity, ρ_e. For this electrical conductor, the electrical resistance, R_e is given by

$$R_e = \frac{\rho_e L}{A} \quad . \tag{4.27}$$

If the conductor is subjected to a normal stress along the axis of the strain gauge, the cross sectional area and the length will change, resulting in a change of the total electrical resistance, R_e. The total change in R_e is due to several effects, as illustrated by the total differential of Eq. 4.27.

$$\frac{dR_e}{R_e} = \frac{dL}{L} + \frac{d\rho_e}{\rho_e} - \frac{dA}{A} \quad , \tag{4.28}$$

which may be expressed in terms of Poisson's ratio, ν_x and ν_y in the *x*-direction and *y*-direction, respectively, as

$$\frac{dR_e}{R_e} = \frac{dL}{L}(1 + \nu_x + \nu_y) + \frac{d\rho_e}{\rho_e} \quad . \tag{4.29}$$

The gauge factor of a material is defined as the fractional change in resistance, R_e, of a material per unit strain, ε, i.e.,

$$GF = \frac{dR_e / R_e}{dL / L} = \frac{dR_e / R_e}{\varepsilon} \quad . \tag{4.30}$$

Equation 4.30 can be expressed in terms of Poisson's ratio, ν, and resistivity, ρ_e, for longitudinal and transverse direction, respectively,

$$\frac{\Delta R_e}{R_e \varepsilon} = 1 + \nu_x + \nu_y + \frac{\Delta \rho_e}{\rho_e \varepsilon} \quad , \tag{4.31}$$

$$\frac{\Delta R_e}{R_e \varepsilon} = -1 + \nu_x - \nu_z + \frac{\Delta \rho_e}{\rho_e \varepsilon} \quad , \tag{4.32}$$

where *x*, *y* represent the two axes perpendicular to the current flow and *z* is the axis parallel to the flow.

A piezoresistive material will change its resistivity if a strain is applied to it. In a manner analogous to the stress, which can be fully described by a 3×3 symmetrical tensor (with only 6 independent variables), the change in the resistivity, Δ, can be described by a third order tensor. A relationship exists between the stress tensor, [*T*] and the change of resistivity tensor, [Δ]. If the second order effect is ignored, the two tensors are linearly related as

$$[\Delta] = [\pi][T] \quad , \tag{4.33}$$

where the tensor [π] is called piezoresistive tensor which is a 6×6 matrix. For cubic type single crystals such as silicon and germanium, the matrix of the piezoresistive tensor based on the principle axes, is (French and Evans, 1989)

$$\pi = \begin{bmatrix} \pi_{11} & \pi_{12} & \pi_{12} & 0 & 0 & 0 \\ \pi_{12} & \pi_{11} & \pi_{12} & 0 & 0 & 0 \\ \pi_{12} & \pi_{12} & \pi_{11} & 0 & 0 & 0 \\ 0 & 0 & 0 & \pi_{44} & 0 & 0 \\ 0 & 0 & 0 & 0 & \pi_{44} & 0 \\ 0 & 0 & 0 & 0 & 0 & \pi_{44} \end{bmatrix} . \tag{4.34}$$

Equation 4.34 shows that there are three coefficients, π_{11}, π_{12}, π_{44}, to describe the piezoresistivity of the single crystal silicon. However, if an orientation other than aligned to a principle axes is required then a coordinate transformation is used. For example, transformation to a coordinate system (x', y', z') which is related to the principle axes system through

$$\begin{bmatrix} x' \\ y' \\ z' \end{bmatrix} = \begin{bmatrix} l_1 & m_1 & n_1 \\ l_2 & m_2 & n_2 \\ l_3 & m_3 & n_3 \end{bmatrix} \begin{bmatrix} x \\ y \\ z \end{bmatrix} , \tag{4.35}$$

where the direction cosines l_i, m_i, n_i are defined as

$$\begin{bmatrix} l_1 & m_1 & n_1 \\ l_2 & m_2 & n_2 \\ l_3 & m_3 & n_3 \end{bmatrix} = \begin{bmatrix} c\phi c\theta c\varphi - s\phi c\varphi & s\phi c\theta c\varphi + c\phi s\varphi & -s\theta c\varphi \\ -c\phi c\theta s\varphi - s\phi c\varphi & -s\phi c\theta s\varphi + c\phi c\varphi & s\theta s\varphi \\ c\phi s\theta & s\phi c\theta & c\theta \end{bmatrix} \tag{4.36}$$

in which $c\phi$ means $\cos(\phi)$, $s\phi$ means $\sin(\phi)$, etc, and ϕ is the Euler's angle for axis rotation. Therefore, the standard equations for longitudinal, π_l, and transverse, π_t, piezoresistance can be expressed as

$$\pi_l = \pi'_{11} = \pi_{11} + 2(\pi_{12} + \pi_{44} - \pi_{11})(l_1^2 m_1^2 + l_1^2 n_1^2 + m_1^2 n_1^2) \quad , \tag{4.37}$$

$$\pi_t = \pi'_{12} = \pi_{12} + (\pi_{11} - \pi_{12} - \pi_{44})(l_1^2 l_2^2 + m_1^2 m_2^2 + n_1^2 n_2^2) \quad . \tag{4.38}$$

Similarly, for the piezoresistance coefficients, S_{11} and S_{12}, which relate the strain in a single crystal material are

$$S_{ii}' = S_{11} + (2S_{12} + S_{44} - 2S_{11})(l_i^2 m_i^2 + l_i^2 n_i^2 + m_i^2 n_i^2) \quad , \tag{4.39}$$

$$S_{ij}' = S_{12} + (S_{11} - S_{12} - \frac{1}{2}S_{44})(l_i^2 l_j^2 + m_i^2 m_j^2 + n_i^2 n_j^2) \quad . \tag{4.40}$$

Then the gauge factor in an arbitrary direction is defined as (French and Evans, 1989)

$$GF = 1 - \Sigma \frac{S'_{ij}}{S_{ii}}(1 - \delta_{ij}) + \frac{\pi_l}{S_{ii}} \quad . \tag{4.41}$$

where S_{ij} and S'_{ij} are the reduced form of the compliance tensor for x, y, z and x', y', z', respectively and other parameters are as previously defined.

4.1.4. Polysilicon strain gauge

Polysilicon in comprised of small crystallites (grains) of single crystal separated by a thin non-crystalline region (grain boundary). Early investigations into the electrical properties of polysilicon revealed a marked difference between its properties and those of the single crystal material (French and Evans 1989). The electrical properties of polysilicon can be described by means of the "carrier-trapping model" originally proposed by (Kamins, 1971). This model starts from the assumption that the grain boundaries comprise a large number of traps and that the doping atoms are uniformly

distributed and ionized. Due to the trapping of carriers, a region of width *W* into the grain is depleted of carriers. This is known as the carrier-trapping model. The initially electrically neutral traps are charged through the trapping of free carries at the grain boundaries, and the effective carrier density is reduced. For this reason, depletion regions occur in the adjacent crystal grains. This results in barriers formed at the grain boundaries. The one-dimensional structure of polysilicon and energy band diagram of the "carrier-trapping model" is shown in Fig. 4.2 (French and Evans, 1989).

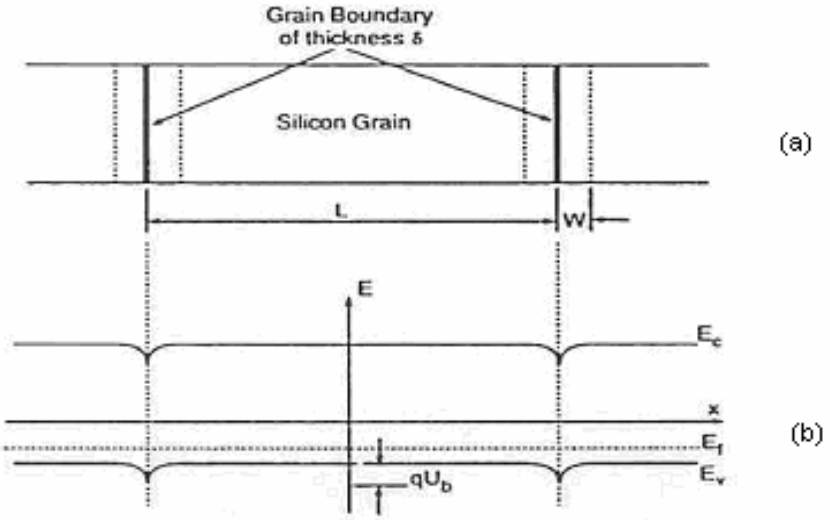

Fig. 4.2. Carrier-trapping model: (a) one-dimensional grain structure, (b) energy band diagram for p-type polysilicon (French and Evans, 1989).

Kamins' model treats the barrier as a Schottky barrier is assumed to be due to thermionic emission. Assuming that the voltage drop across each grain is small and thus the barrier behaves as a linear resistor, the expression for conductivity, σ_b, using this model is given by (Singh, et al., 1985)

$$\sigma_b = \frac{L_{gb} q^2 N_c \nu_r}{KT\left(1+\frac{\nu_r}{\nu_d}\right)} \exp\left(-\frac{q\phi_b}{KT}\right) \quad , \tag{4.42}$$

where q is the elementary charge, N_c is the effective density of states, K is the Boltzmann's constant, T is the temperature, ν_d is the diffusion velocity, and φ_b is the barrier height relative to the Fermi level, L_{gb} is the barrier width $(2\omega + \delta)$, and the recombination velocity, ν_r, is given by

$$\nu_r = \frac{A'T^2}{qN_c} \quad , \tag{4.43}$$

where A' is the general Richardson's characteristic, which can be defined for p-type material and n-type materials, and where

$$A_i' = \frac{4\pi q k^2 m_{ij}}{h^3} \tag{4.44}$$

and

$$A_i' = \frac{4\pi q k^2 \left(l^2 m_y m_z + m^2 m_x m_z + n^2 m_x m_y\right)^{0.5}}{h^3} \quad , \tag{4.45}$$

respectively. In Eqs 4.44 and 2.45, m_{ij} represents the effective mass for the ith and jth valley, h is the Planck's constant, and other parameters are as previously defined.

In the limit of small voltages, the barrier, whose conductivity is defined by Eq. 4.42, can be modeled by linear resistors. Thus the electrical resistivity, ρ_e, can be written in terms of grain and barrier resistivities, ρ_g and ρ_b, respectively, as

$$\rho_e = \frac{\left[L - (2\omega + \delta)\right]\rho_g}{L} + \frac{(2\omega + \delta)\rho_b}{L} \quad , \tag{4.46}$$

where δ is the thickness of the grain boundary, L is the length of the grain, and W is the width of the depletion region. Therefore, the change in resistivity induced by the strain can be found to be

$$\frac{\Delta\rho_e}{\varepsilon} = \frac{\left[L-(2\omega+\delta)\right]}{L}\frac{\Delta\rho_g}{\varepsilon} + \frac{(2\omega+\delta)}{L}\frac{\Delta\rho_b}{\varepsilon} \quad . \tag{4.47}$$

For a single grain, which can be considered single crystal silicon, the gauge factor can be obtained by combining Eqs 4.46 and 4.47 to obtain

$$GF = 1 - \left\{ \sum \frac{S'_{ij}}{S'_{ii}}(1-\delta_{ij}) + \frac{\rho_g \pi_{\mathrm{lg}}}{\left[\dfrac{\rho_g + (2\omega+\delta)\rho_b}{L-(2\omega+\delta)}\right]} + \frac{\rho_b \pi_{lb}}{\left[\rho_b + \dfrac{\left[L-(2\omega+\delta)\right]\rho_g}{(2\omega+\delta)}\right]} \right\} \quad , \tag{4.48}$$

where S'_{ij}, S'_{ii}, π_{lg} and π_{lb} are the reduced form of the compliance tensor, and longitudinal piezoresistive coefficients of the grain and barrier, respectively.

If the gauge factor for a polysilicon film is to be calculated, the texture of the film must be considered. The film structure can consist of grains with either:

1) a random distribution of orientations,

2) a small number of dominant orientations.

In the case of a textured structure a small number of orientations of the crystal axis to the layer are allowed. Thus, Eq. 4.48 becomes (French and Evans, 1989)

$$GF = 1 - \Sigma R_{\alpha\beta\gamma}\left[2\left\langle\frac{S'_{ij}}{S'_{ii}}\right\rangle_{\alpha\beta\gamma} + \left\langle\frac{R_1\pi_{lg}}{S'_{ii}} + \frac{R_2\pi_{lb}}{S'_{ii}}\right\rangle_{\alpha\beta\gamma}\right] \quad , \tag{4.49}$$

where

$$R_1 = \frac{\rho_g}{\left[\frac{\rho_g + (2\omega+\delta)\rho_b}{L-(2\omega+\delta)}\right]} \quad , \tag{4.50}$$

and

$$R_2 = \frac{\rho_b}{\left[\rho_b + \frac{\left[L-(2\omega+\delta)\right]\rho_g}{(2\omega+\delta)}\right]} \quad . \tag{4.51}$$

In Eq. 4.49, $R_{\alpha\beta\gamma}$ is the relative abundance of the <$\alpha\beta\gamma$> orientations and $\left\langle\frac{S'_{ij}}{S'_{ii}}\right\rangle_{\alpha\beta\gamma}$ is given by

$$\left\langle\frac{S'_{ij}}{S'_{ii}}\right\rangle_{\alpha\beta\gamma} = \left.\frac{\int_{\varphi=0}^{\pi/2}\frac{S_{ij}}{S_{ii}}d\varphi}{\int_{\varphi=0}^{\pi/2}d\varphi}\right|_{\theta=\theta_{\alpha\beta\gamma}}^{\phi=\phi_{\alpha\beta\lambda}} \quad , \tag{4.52}$$

with a similar equation being used for $\left\langle\frac{R_1\pi_{lg}}{S'_{ii}} + \frac{R_2\pi_{lb}}{S'_{ii}}\right\rangle_{\alpha\beta\gamma}$.

4.1.5. Strain gauge placement and sensitivity optimization

The most common method of measuring strain is through the change in electrical resistance that materials exhibit under load. The output of a bonded resistance strain

gauge is a change in resistance, ΔR. A Wheatstone bridge is generally used to detect the small changes in resistance that form the output of a strain gauge measurement circuit. In many applications, strain measurements under both static and dynamic loading conditions are desired. A Wheatstone bridge circuit, or a similar bridge circuit, is the most often used means of measuring the resistance changes associated with static and dynamic loading of a strain gauge. A fundamental circuit analysis of an arrangement of strain gauges in a bridge circuit yields the relationship between the input strains and output voltage of the bridge circuit. Consider the case when all four resistances in the bridge circuit of Fig. 4.3 represent active strain gauges (Figiola and Beasley, 1991).

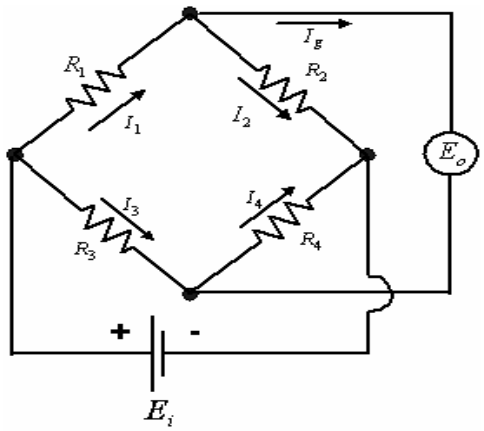

Fig. 4.3. The Wheatstone bridge circuit: E_i is the input voltage, E_o is the output voltage.

The bridge output is given by

$$E_o = E_i\left(\frac{R_1}{R_1 + R_2} - \frac{R_3}{R_3 + R_4}\right) \quad , \tag{4.53}$$

where E_i is the input voltage to the Wheatston bridge, while R_1 *to* R_4 represent resistances of the arms of the bridge. The strain gauges R_1 *to* R_4 are assumed initially to be in a state

of zero strain. If these gauges are now subjected to strains such that the resistances change by dR_i, where i=1, 2, 3 and 4, then the change in the output voltage can be expressed as

$$dE_o = \sum_{i=1}^{4} \frac{\partial E_0}{\partial R_i} dR_i \quad . \tag{4.54}$$

Evaluation of the appropriate partial derivatives from Eq. 4.53 and substitution into Eq. 4.54 yield

$$dE_o = E_i \left[\frac{R_2 dR_1 - R_1 dR_2}{(R_1 + R_2)^2} + \frac{R_3 dR_4 - R_4 dR_3}{(R_3 + R_4)^2} \right] \quad . \tag{4.55}$$

If $R_1 = R_2 = R_3 = R_4$ and $dR_i << R_i$, then Eq. 4.55 leads to

$$\frac{\delta E_o}{E_i} = \frac{1}{4} \left(\frac{\delta R_1}{R_1} - \frac{\delta R_2}{R_2} + \frac{\delta R_4}{R_4} - \frac{\delta R_3}{R_3} \right) \quad . \tag{4.56}$$

Furthermore, the equation for the sensitivity, S, can be expressed as

$$S = \frac{1}{p} \left(\left. \frac{\delta E_o}{E_i} \right|_p - \left. \frac{\delta E_o}{E_i} \right|_{p_o} \right) \quad , \tag{4.57}$$

where p is the applied pressure, p_o is the initial pressure. Since p_o equals to zero at the initial time, there is no change in the resistance of the Wheatston bridge. Thus from Eq. 4.53

$$\frac{\delta E_o}{E_i} = \left(\frac{R_1}{R_1 + R_2} - \frac{R_3}{R_3 + R_4} \right) = \frac{R_1 R_4 - R_2 R_3}{(R_1 + R_2)(R_3 + R_4)} \quad . \tag{4.58}$$

Since $R_1 = R_2 = R_3 = R_4$, Eq. 4.58 equals zero and the term in parenthesis in Eq. 4.56 must also be zero. By substituting Eqs 4.56 and 2.30 into Eq. 4.57, one finds that

$$S = \frac{1}{4p}\left(\varepsilon_1 GF_1 - \varepsilon_2 GF_2 + \varepsilon_4 GF_4 - \varepsilon_3 GF_3\right) \quad . \tag{4.59}$$

Equation 4.59 shows that for a bridge containing four active strain gauges, equal strains on opposite bridge arms add up, whereas equal strains on adjacent arms of the bridge cancel.

These characteristics can be used to increase the sensitivity of the pressure sensor. Therefore, by assuming $\varepsilon_1 GF_1 = \varepsilon_4 GF_4$ and $\varepsilon_2 GF_2 = \varepsilon_3 GF$ Eq. 4.59 changes to

$$S = \frac{1}{2p}\left(\varepsilon_1 GF_1 - \varepsilon_2 GF_2\right) \quad . \tag{4.60}$$

4.2. Relative humidity sensors

4.2.1. Different methods of humidity measurements

Various instruments for measuring humidity are available based on a variety of different measurement methods, including hygrometry based on the use of hygroscopic materials, psychrometry, dew-point measurement, and infrared measurements (Brion, 1986). Each measurement method has its own advantages and drawbacks, some of which are listed in Table 4.2. The choice of the instrument type is based on the application, considering aspects such as size, weight, performance, cost, and ease of maintenance.

4.2.2. Thin-film humidity sensors

Thin-film humidity sensors are widely used in many measurement and control applications, including those in automated process control, meteorology, domestic

appliances, agriculture and medical equipment (Arai and Seiyama, 1989). Table 4.3 summarizes their application areas and their corresponding operating ranges in relative humidity and temperature (Yamazoe, 1986; Traversa, 1995).

As shown in Fig. 4.4, thin-film humidity sensors can be categorized as capacitive (Delapierre, et al.,1983) resistive (Tsuchitani, et al., 1985), mechanical (Gerlach and Sager, 1994; Boltzhauser, et al., 1993) and oscillating types (Howe and Muller, 1986; Nomura, et al., 1993) based on the sensing principle used.

Table 4.2. Comparisons of hygrometers.

Hygrometer	Principle	Advantage	Drawback
Hygrometers using hygroscopic materials	Mechanical property change (length, volume, stress)	No power requirement Low sensitivity to temperature Inexpensive Simple	Non-linear output Hysteresis Drift over time
	Electrical property change (resistivity, capacitance, frequency)	Can be mass produced Simple Inexpensive Small Easy to maintain	Hysteresis Sensitive to contamination
Psychrometer	Relative humidity estimation based on dry-and wet-bulb temperature measurements	No requirement of calibration	Requirement of regular replacement of wick and distilled water requirement of air-flow with high flow rate (3 m/sec)
Dew-point hygrometer	Measurement of dew-point temperature by detecting dew formation on a cooler base	High accuracy wide dynamic range No requirement of calibration	Large size Expensive Large power consumption Regular cleaning of mirror surface
Infrared hygrometer	Selective absorption of distinctive infrared spectrum by water vapor	Can be used with corrosive gases Wide dynamic range	Expensive Possibility of interference with other gas species

Table 4.3. Application of humidity sensors and their operating ranges in terms of the relative humidity and temperature measurements.

Industry	application	Operating Temperature °C	Humidity range (%RH)
Domestic electric appliance	Air conditioning system	5~40	40~70
	Drier for clothing	80	0~40
	Microwave oven	5~100	2~100
	VTR	5~60	60~100
Automobile	Car window	20~80	50~100
Medical service	Medical apparatus	10~30	80~100
	Incubator	10~30	50~80
Industry	Textile mill (spinning)	10~30	50~100
	Drier for ceramic powder	5~100	0~50
	Dehydrate food	50~100	0~50
	ESD control	22	30~70
	Clean room	21	36~39
	Humidity control in factories	5~40	0~50
	Humidifier for industry	30~300	50~100
	Web printing		40~50
	Motor assembly line	17~25	40~55
	Electric device manufacturing	5~40	0~50
Agriculture	Forcing culture	5~40	0~100
	Broiler farming	20~25	40~70
	Cereal stocking	15~20	0~45
Measurement	Thermo-hygrostatic chamber	5~100	0~100
	Raido-sonde	50~40	0~100
	Hygrometer	5~100	0~100
Community safety	Nuclear power reactor	>80	80
	Humidity in boiler	100~400	50~100

Among the different types of humidity sensors, those based on electrical properties such as impedance (resistance) and capacitance, are best suited to modern automatic control systems. Generally speaking, a humidity sensor has to fulfill the following requirements to satisfy the widest range of applications: sensitivity, speed, stability, cost, selectivity, linearity, and power consumption.

The purpose of adopting humidity sensors based on given operating conditions, are quite different depending on the field of application, each field requiring a specific humidity sensor.

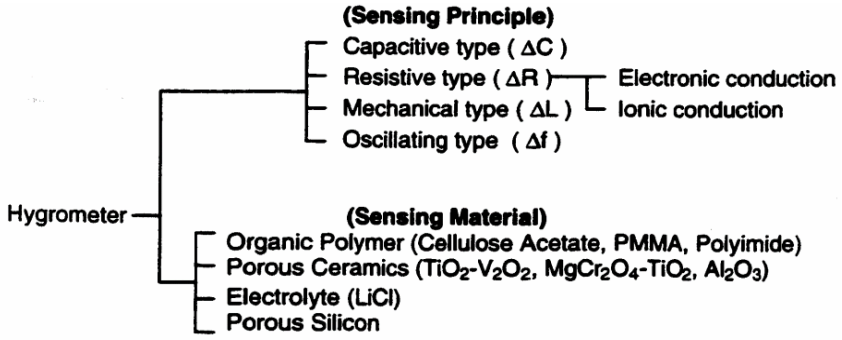

Fig. 4.4. Classification of hygrometers based on the sensing principle and the sensing material (Kang and Wise, 1999).

4.2.3. Sensing film structures: the key to water vapor sensing

The sensitive film is the key to understanding the design and operation of water vapor microsensors. The ideal sensing film will have a high sensitivity to water vapor with a linear response from 0% to 100% RH, short response time, high selectivity (i.e., low or no cross sensitivity to water), and high stability. Many of the materials, such as polyimide and aluminum oxide (Al_2O_3), are widely used in commercial water vapor sensors that are discussed later in this chapter. Table 4.4 summarizes sensing materials, principles, temperatures of operation, humidity ranges and response times for humidity sensors based on impedance or capacitance (Fenner and Zdankiewicz, 2001).

Table. 4.4. Summary of response times for thin-film humidity sensors.

Reference	Year	Principle	Material	Film thickness (μm)	Response time
Hijikigawa, et al., 1983	1983	Resistive	Polymer	10	100 (sec)
Tsuchitani, et al., 1985	1985	Resistive	Ionic copolymer	10	2 (min)
Jadhav, et al., 1985	1985	Resistive	AlOx	120-450 (nm)	20 (sec)
Grange, et al., 1987	1987	Capacitive	Polymer	NA	2 (min)
Shimizu, et al., 1988	1988	Capacitive	Polyimide	<1	15 (sec)
Sadaoka, et al., 1992	1992	Optical	Polymer	5	1 (min)
Boltzhauser, et al., 1993	1993	Capacitive	Polyimide	10	30 (sec)
kuroiwa, et al., 1993	1993	Capacitive	Polyimide	2-5	30 (sec)
Miyazaki, et al., 1994	1994	Resistive	MnO2	300	15 (min)
Roman, et al., 1995	1995	Capacitive	PMMA	5-10	1-2 (min)

The sensing materials are roughly classified into four groups as shown in Fig. 4.4, i.e., organic polymers, porous ceramics, electrolyte, and porous silicon.

Polymers are essentially electrical nonconductors, with bulk resistances 18 orders of magnitude greater than metal. Consequently, when they are used as a sensing film for water vapor sensors, their electrical dielectric and physical properties, increase due to water uptake these changes, or dimensional changes, caused by polymer swelling and can be used as a transduction scheme.

Porous ceramic films are formed on substrates using through the following techniques: (a) conductive inks or pastes deposited and patterned by thick film screen printing techniques, (b) plasma or vapor deposited semiconducting metal oxides, such as tin oxide, (c) in situ, films formed by direct anodization of an aluminum or silicon substrate.

Ceramic films formulated from a mixture of metal oxide salts, such as TiO_2-V_2O_5, or magnesium-aluminum silicate, are usually screen printed onto an alumina substrate. Film thickness is usually greater than 10 μm. Dopants can be added to the mixture as

reaction catalysts to promote the dissociation of absorbed water into hydrogen and hydroxyl ions. The hydroxyl ions decrease the bulk resistivity, which can be measured as a change in AC impedance. Metal oxide films formed by vapor or plasma deposition on a silicon substrate will also operate as impedance-based devices, but will utilize the electron interactions between water and the semiconducting properties of the film. Because water vapor is chemisorbed onto a metal oxide film, thermal energy is required to desorb the water vapor from the film. Metal oxide film thickness is typically less than 5 μm.

Alumina films are formed by directly modifying the top layers of the substrate through anodization or electrochemical etching (for silicon). Changes in capacitance or conductance can be measured, and are a function of the amount of water that is absorbed into the film due to diffusion through the bulk, or by capillary transport of water into the film's pores of the film (Fenner, and Zdankiewicz, 2001).

Lithium chloride is the most popular electrolyte. An electric hygrometer using lithium chloride developed by Dunmore (Dunmore, 1938), operates on the principle that lithium chloride solution immersed in a porous binder changes its ionic conductivity depending on the relative humidity of the surrounding atmospheric air (Yamazo, 1986). In this device, an aluminum tube coated with polystyrene resin is fitted with a pair of wound palladium wires (electrodes), followed by a humidity-sensitive coating of partially hydrolysed polyvinyl acetate impregnated with lithium chloride. The humidity range to be covered by one unit is narrow, depending upon the amount of impregnated lithium chloride. A wide relative humidity range from 10 to 100% can be measured with a set of

units with different sensing characteristics. A small-sized, lightweight humidity sensor, 10 mm long, 4 mm wide, 0.2 mm thick and 70 mg in weight has been made using plant pith as the porous binder. These sensors show rather slow responses to humidity, but have a fairly good stability, and have been used widely in radio-sonde circuits as well as control instruments.

Porous silicon (PS) is electrochemically formed by anodic dissolution of silicon in a hydrofluoric acid (HF) solution. It has been extensively studied since it was discovered by Turner in 1958 (Turner, 1958) and, particularly, since the observations of strong visible luminescence from PS at room temperature, (suggesting promising applications in silicon–based optoelectronic devices (Canham, 1990). Silicon micromachining and microsensors are also applications for PS (Foucaran, et al., 2000).

Owing to its very large surface area to volume ratio (>500 m^2/cm^3), PS can absorb large amounts of foreign molecules on its surface. With the presence of these molecules, many properties associated with PS will change. For example, photoluminescence (PL) efficiently decreases when PS is exposed to various chemicals and the final PL efficiency depends on the dipole moment of the physically absorbed molecules (Lauerhaas, et al., 1992). Likewise, the effective dielectric constant and conductivity of PS layer will change if the PS surface is saturated with some other molecules. Therefore, a capacitance-based (O'Halloran, et al., 1997) or conductance-based (Schechter, et al., 1995) humidity sensor can be made which uses the relative change of dielectric constant or conductivity, when moisture is adsorbed on the surface of a PS layer. The change in the measured capacitance and conductance of a PS humidity sensor would thus depend

on the selection of the frequency of the signal source and the pore size and distribution of the PS layer. The contact geometry on the PS surface is also important and may considerably influence the measurements. This is further aggravated by the unavoidable presence of parasitic capacitance (Das, et al., 2001).

4.2.4. Capacitance for diffusion into a rectangular body

The transient capacitance has been derived for four-sided diffusion into a rectangular body. Figure 4.5 illustrates the moisture diffusion into a rectangular body, which has a length of 2*a*, a width of 2*b*, and a height of *d*.

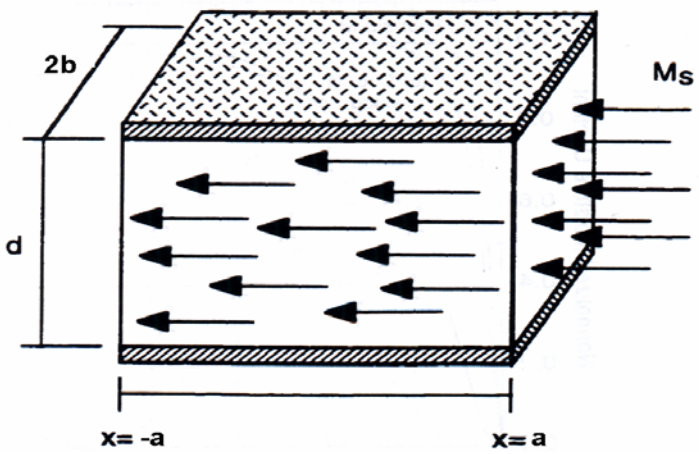

Fig. 4.5. Geometry of a rectangular solid where diffusion into the body takes place from four-sides. The moisture concentration at all surfaces is fixed at M_s.

The mathematical theory of diffusion in isotropic substances is based on the hypothesis that the rate of transfer of a diffusing substance through unit area of a section is proportional to the concentration gradient measured normal to the section, i.e.,

$$F = -D\frac{\partial M}{\partial x} \quad , \tag{4.61}$$

where F is the rate of transfer per unit area of section, M is the concentration of diffusing substance, x is the space coordinate measured normal to the section, and D is called the diffusion coefficient. The fundamental differential equation of diffusion in an isotropic medium is derived from Eq 4.61 as follows.

Consider an element of volume in the form of a rectangular paralleled-piped whose sides are parallel to the axes of coordinates and are of lengths $2dx$, $2dy$, $2dz$. Let the center of the element be at P(x,y,z), where the concentration of diffusing substance is M. Let $ABCD$ and $A'B'C'D'$ be the faces perpendicular to the axis of x as in Fig 4.6.

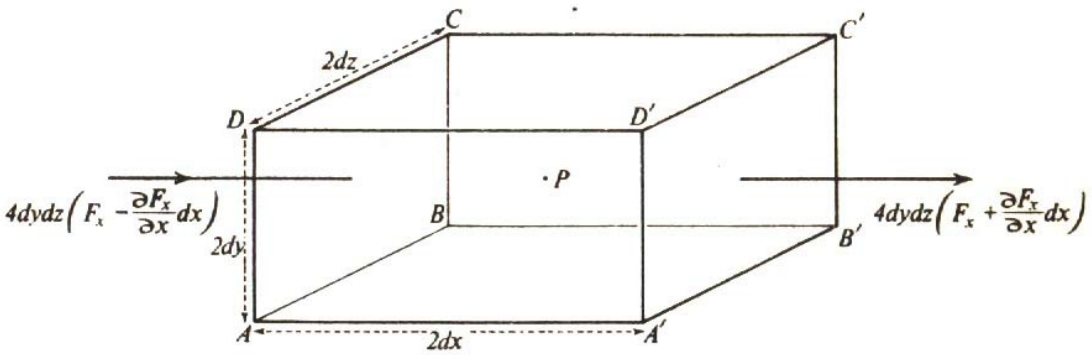

Fig. 4.6. Element of volume (Crank, 1975).

Then the rate at which diffusing substance enters the element through the face $ABCD$ in the plane x-dx is given by

$$4dydz\left(F_x - \frac{\partial F_x}{\partial x}dx\right) \quad , \tag{4.62}$$

where F_x is the rate of transfer through unit area of the corresponding plane through P. Similarly, the rate of loss of diffusion through the face $A'B'C'D'$ is given by

$$4dydz\left(F_x + \frac{\partial F_x}{\partial x}dx\right) \quad . \tag{4.63}$$

The contribution to the rate of diffusing substance in the element from these two faces is thus equal to

$$-8dxdydz\left(\frac{\partial F_x}{\partial x}\right) \quad . \tag{4.64}$$

Following the same procedure, from the other faces we obtain

$$-8dxdydz\frac{\partial F_y}{\partial x} \text{ and } -8dxdydz\frac{\partial F_z}{\partial x} \, . \tag{4.65}$$

But the rate at which the amount of diffusing substance in the element increases is given by

$$-8dxdydz\left(\frac{\partial M}{\partial t}\right) \quad . \tag{4.66}$$

Hence we have

$$\frac{\partial M}{\partial t} + \frac{\partial F_x}{\partial x} + \frac{\partial F_y}{\partial x} + \frac{\partial F_z}{\partial x} = 0 \, . \tag{4.67}$$

If the diffusion coefficient is constant, F_x, F_y, F_z are given by 4.61, and Eq. 4.67 becomes

$$\frac{\partial M}{\partial t} = D\left(\frac{\partial^2 M}{\partial x^2} + \frac{\partial^2 M}{\partial y^2} + \frac{\partial^2 M}{\partial z^2}\right) \quad . \tag{4.68}$$

Equation 4.68 can be solved by specifying the boundary conditions and initial conditions for the concentration. The top and bottom surfaces serve as electrodes for the capacitance readout. Then, there is no gradient of concentration along the *z*-direction. Therefore, the Fick's first law changes to,

$$\frac{\partial M}{\partial t} = D\left(\frac{\partial^2 M}{\partial x^2} + \frac{\partial^2 M}{\partial y^2}\right) \quad . \tag{4.69}$$

At first, the initial condition is assumed to be a constant value (i.e., at the initial time, there is a constant water vapor concentration in the sensitive layer). Since the sensitive layer is abruptly exposed to a humid environment until it reaches the steady state, the boundary conditions are assumed to be constant corresponding to specific relative humidity of the environment. Thus, the solution for this differential equation can be separated into two parts,

$$M = M_1 + M_2 \quad , \tag{4.70}$$

where M_1 and M_2 are the solutions following two equations below with the specific field boundary and initial conditions (Crank, 1975):

$$\begin{aligned} &\frac{\partial M_1}{\partial t} = D\left(\frac{\partial^2 M_1}{\partial x^2} + \frac{\partial^2 M_1}{\partial y^2}\right) \quad , \\ &M_1(x, y, 0) = M_0 \quad , \\ &M_1(x, y, t) = 0 \quad . \end{aligned} \tag{4.71}$$

and

$$\begin{aligned} &\frac{\partial M_2}{\partial t} = D\left(\frac{\partial^2 M_2}{\partial x^2} + \frac{\partial^2 M_2}{\partial y^2}\right) \quad , \\ &M_2(x, y, 0) = 0 \quad , \\ &M_2(x, y, t) = M_s \quad . \end{aligned} \tag{4.72}$$

The solutions to Eqs 4.71 and 4.72 are

$$M_1(x, y, t) = {M_0}^2 \frac{16}{\pi^2}\left[\sum_{m=0}^{\infty}\sum_{n=0}^{\infty} \frac{(-1)^{m+n}\exp\left(-\alpha_{m,n}t\right)}{(2n+1)(2m+1)} \cos\left(\frac{(2m+1)\pi x}{2a}\right)\cos\left(\frac{(2n+1)\pi y}{2b}\right)\right] \quad , \tag{4.73}$$

and

$$M_2(x,y,t) = M_s - M_s \frac{16}{\pi^2}\left[\sum_{m=0}^{\infty}\sum_{n=0}^{\infty} \frac{(-1)^{m+n}\exp\left(-\alpha_{m,n}t\right)}{(2n+1)(2m+1)} \cos\left(\frac{(2m+1)\pi x}{2a}\right)\cos\left(\frac{(2n+1)\pi y}{2b}\right)\right], \tag{4.74}$$

respectively, where

$$\alpha_{m,n} = \frac{D\pi^2}{4}\left[\frac{(2m+1)^2}{a^2} + \frac{(2n+1)^2}{b^2}\right]. \tag{4.75}$$

Since the solution of Eq. 4.69 is the superposition of the solutions to Eqs 4.71, and 4.72, therefore

$$M(x,y,t) = M_s + \left(M_0{}^2 - M_s\right)\frac{16}{\pi^2}\left[\sum_{m=0}^{\infty}\sum_{n=0}^{\infty} \frac{(-1)^{m+n}\exp\left(-\alpha_{m,n}t\right)}{(2n+1)(2m+1)} \cos\left(\frac{(2m+1)\pi x}{2a}\right)\cos\left(\frac{(2n+1)\pi y}{2b}\right)\right] \quad . \tag{4.76}$$

The dielectric constant ε_r changes linearly (Denton, et al., 1990) with moisture absorption so that it can be written as

$$\varepsilon_r(x,y,t) = K_1 M(x,y,t) + K_2 \quad , \tag{4.77}$$

where K_1 and K_2 are constants determined by the specific liquid vapor under condensation (Horie and Yamashita, 1995). The capacitance of the body, C, is calculated as

$$C = \int_{-b}^{b}\int_{-a}^{a} \frac{\varepsilon_0\varepsilon_r(x,y,t)}{d}\,dxdy \quad , \tag{4.78}$$

where a, b, d, ε_0, and ε_r are the half length, half width, thickness, permittivity, and relative permittivity, respectively. By substituting Eq. 4.77 into Eq. 4.78 and simplifying, the capacitance is obtained as

$$C = \frac{4\varepsilon_0 K_2 ab}{d} + \frac{\varepsilon_0 K_1}{d} \int_{-b}^{b} \int_{-a}^{a} M(x,y,t)\,dxdy \quad , \tag{4.79}$$

or

$$C = \frac{4\varepsilon_0 K_2 ab}{d} + \frac{\varepsilon_0 K_1}{d} \int_{-b}^{b} \int_{-a}^{a} M_s + \left(M_0{}^2 - M_s\right)\frac{16}{\pi^2} \times \left[\sum_{m=0}^{\infty} \sum_{n=0}^{\infty} \frac{(-1)^{m+n} \exp\left(-\alpha_{m,n} t\right)}{(2n+1)(2m+1)} \cos\left(\frac{(2m+1)\pi x}{2a}\right) \cos\left(\frac{(2n+1)\pi y}{2b}\right) \right] dxdy \quad . \tag{4.80}$$

In order to simplify, the capacitance is normalized with respect to the final steady-state capacitance value, i.e.,

$$C_{nor} = \frac{C - C_0}{C_f - C_0} \quad , \tag{4.81}$$

where C_0, and C_f are initial and final capacitances, respectively. By substituting Eq. 4.79 into Eq. 4.80, the final equation for C_{nor} is determined to be

$$C_{nor} = \frac{\sum_{m=0}^{\infty} \sum_{n=0}^{\infty} \frac{(-1)^{m+n}}{(2n+1)(2m+1)} \int_{-a}^{a} \int_{-b}^{b} \cos\left(\frac{(2m+1)\pi x}{2a}\right) \cos\left(\frac{(2n+1)\pi y}{2b}\right) - \sum_{m=0}^{\infty} \sum_{n=0}^{\infty} \frac{(-1)^{m+n}}{(2n+1)(2m+1)} \exp(-\alpha_{m,n} t) \int_{-a}^{a} \int_{-b}^{b} \cos\left(\frac{(2m+1)\pi x}{2a}\right) \cos\left(\frac{(2n+1)\pi y}{2b}\right)}{\sum_{m=0}^{\infty} \sum_{n=0}^{\infty} \frac{(-1)^{m+n}}{(2n+1)(2m+1)} \int_{-a}^{a} \int_{-b}^{b} \cos\left(\frac{(2m+1)\pi x}{2a}\right) \cos\left(\frac{(2n+1)\pi y}{2b}\right)} \quad . \tag{4.82}$$

4.3. Temperature sensors

4.3.1. Quantitative model for polycrystalline silicon resistors

Polysilicon is a three-dimensional material with grains having a wide distribution of sizes and irregular shapes. For simplicity it is assumed that polysilicon is composed of identical cubic grains with a grain size L and that its transport properties are one dimensional, Fig. 4.7. The applied voltage V_a over all N_g grains between two resistor contacts is assumed to be equally dropped across all grains (grain voltage $V_g = V_a/N_g$).

The single-crystal silicon energy band structure is assumed applicable inside the crystallites. For convenience, the intrinsic Fermi level E_{i0} at the center of the grain is chosen to be zero. The electronic energy is chosen to be positive in the upward and negative in the downward directions, Fig. 4.7. The thickness of the grain boundary Δ is much smaller than L, and the boundary contains Q_t traps per unit area that are initially neutral and become charged at a certain monoenergetic level E_T (with respect to E_{i0}) after carrier trapping. The properties for doped and undoped material are explained in this section.

4.3.1.1. Undoped material

It is generally believed that the chemical potential of polysilicon grain boundaries lies somewhere near the middle of the forbidden band gap. If no other dopant impurities are added to the deposited polysilicon, the energy band is relatively uniform throughout the film and its behavior is similar to that of uniform intrinsic single-crystal silicon except for the grain boundary effects.

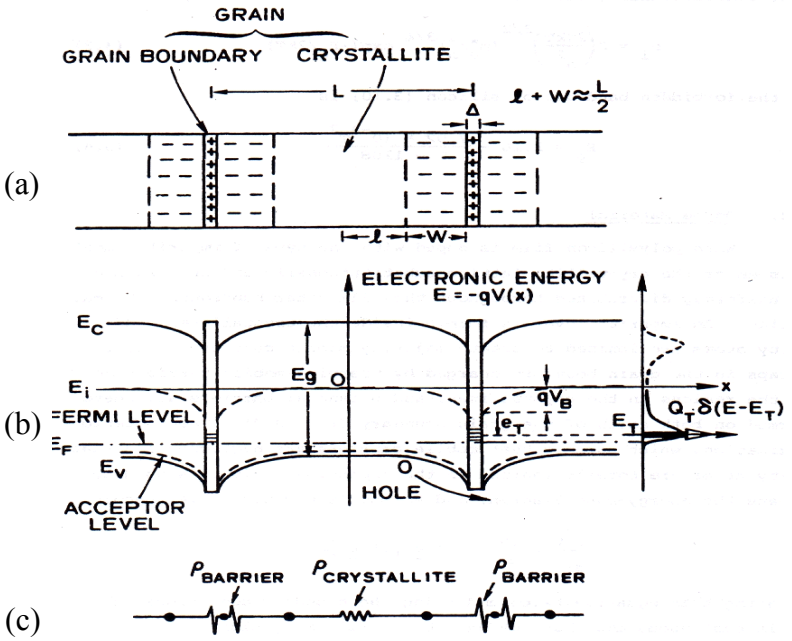

Fig. 4.7. Modified polysilicon trapping model; only the partially depleted grain is shown; when completely depleted, there is no neutral region that extends throughout the grain; when undoped, there is no depletion region and Fermi level is believed to lie near the middle of the band gap: (a) one-dimensional grain structure, (b) energy band diagram for p-type dopants, (c) grain boundary and crystallite circuit (Lu, 1981).

The resistivity of polysilicon, therefore, is

$$\rho = \rho_c\left(1-\frac{\Delta}{L}\right)+\rho_{GB}\left(\frac{\Delta}{L}\right) \quad , \tag{4.83}$$

where ρ_{GB}, ρ_c, Δ, and L are the grain boundary resistivity, single-crystal resistivity, thickness of the grain boundary, and grain length. Single-crystal resistivity, ρ_c, is defined as (Sze, 1969)

$$\rho_c = \frac{1}{qn_i(\mu_n+\mu_p)} \quad , \tag{4.84}$$

where μ_n and μ_p are electron and hole mobilities, respectively, q is elementary charge, and n_i (atoms/cm^3)is the intrinsic carrier concentration defined as

$$n_i = 2\left(\frac{2\pi kT}{h^2}\right)(m_e^* m_h^*)^{\frac{3}{4}} \exp\left(\frac{-E_g}{2kT}\right) \tag{4.85}$$

with T, k, h, m_e^*, m_h^*, and E_g being the temperature, Boltzmann's constant, Planck's constant, electron effective mass, hole effective mass, and the forbidden band gap of silicon (Sze, 1969) which can be computed from

$$E_g = 1.16 - \frac{7.02\times10^{-4}T^2}{T+1108} \quad , \tag{4.86}$$

where E_g is in eV.

4.3.1.2. Doped material

When polysilicon film is doped with one type of impurity, most dopants enter the crystallite lattice substantially and are assumed to be uniformly distributed throughout the film after subsequent thermal annealing. An impurity level is formed inside the crystallites, and impurity atoms are ionized to create the majority mobile carriers (Pearson and Bardeen, 1949). The traps in the grain boundary charged by trapped mobile carriers deplete the regions in the crystallites, and potential barriers are thereby formed on both sides of the grain boundary, Fig. 4.8. The depletion approximation, which assumes that mobile carriers are neglected and that impurity atoms are totally ionized in the depletion region, is used to calculate the energy-band diagram and Poisson's equation (Seto, 1975) becomes

$$\frac{d^2V}{dx^2} = \pm\frac{qN}{\varepsilon}, \qquad l \le |x| \le \frac{L}{2} \quad , \tag{4.87}$$

where N, q, and ε are doping concentration, elementary charge, and single-crystal silicon permittivity, respectively. Integrating Eq. 4.87 twice and using the boundary conditions that $V(x)$ is continuous and that $\frac{dV}{dx} = 0$ at $x = l$, the potential $V(x)$ is

$$V(x) = \pm \frac{qN\left(|x| - l\right)^2}{2\varepsilon}, \qquad l \le |x| \le \frac{L}{2} \quad . \tag{4.88}$$

The potential barrier height V_B is the difference between $V(L/2)$ and $V(0)$, i.e.,

$$V_B = \pm \frac{qNW^2}{2\varepsilon} \quad , \tag{4.89}$$

where + denotes p-type dopants, – indicates the n-type, and W is the depletion-region width ($L/2$-l).

4.3.1.3. Resistivity and mobility

Polysilicon resistivity is composed of three serial components: one is the result of the potential barrier, the second is due to the bulk resistivity of the crystallite, and the third represents the contribution from actual grain boundary and is negligible because of the very narrow boundary width (Seto, 1975; Hirose, et al., 1979). Barrier conductivity is the consequence of two components: thermionic emission resulting from those carriers with an energy high enough to surmount the potential barrier and field emission stemming from carriers with less energy than the barrier height, but capable of tunneling quantum mechanically through the barrier.

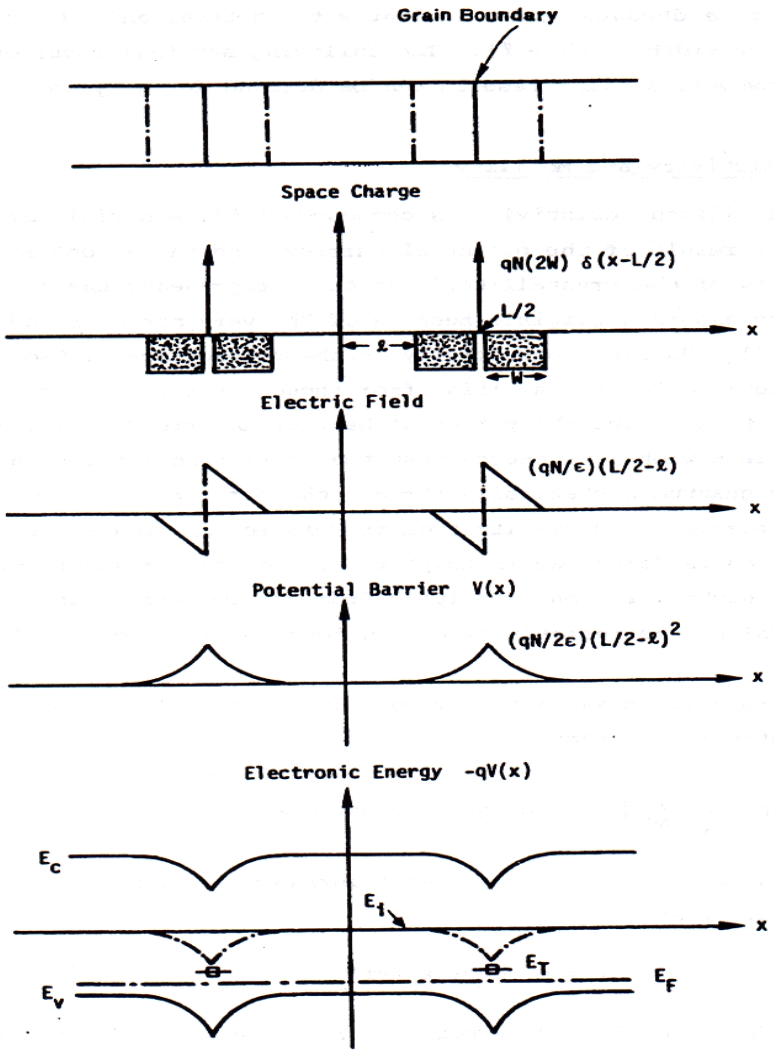

Fig. 4.8. Diagram of a polysilicon grain including charge density, electric field intensity, potential barrier, and energy band diagram (Lu, 1981).

For simplicity only the barrier conductivity from thermionic emission is derived which the field emission is ignored. The bulk resistivity of the neutral crystallite region, resulting from lattice and impurity scattering, is equal to the resistivity of single-crystal silicon (Runyan, 1965; and Wolf, 1969).

Thermionic-emission theory for metal-semiconductor Schottky barriers demonstrates that (Sze, 1969)

$$J = qp(0)\left(\frac{kT}{2\pi m_h^*}\right)^{0.5} \exp\left(\frac{-qV_B}{kT}\right)\left[\exp\left(\frac{qV}{kT}\right)-1\right] \quad , \tag{4.90}$$

where V_B is potential barrier height and the hole concentration $p(0)$ in the equilibrium neutral region (Baccarani, et al.,1978) can be expressed as

$$p(0) = n_i \exp\left(\frac{-E_F}{kT}\right) \quad , \tag{4.91}$$

where E_F is the Fermi energy level with respect to E_{io}. In polysilicon, however, semiconductor material exists on both sides of the barrier (Seto, 1975; Baccarani, et al., 1978; Korsh and Muller, 1978; and Tarng, 1978). The voltage across the barrier V_{ba} is assumed to be equally divided on each side of the junction, and the transport equation (Korsh and Muller, 1978; Tarng, 1978) then becomes

$$J = 2qp(0)\left(\frac{kT}{2\pi m_h^*}\right)^{0.5} \exp\left(\frac{-qV_B}{kT}\right)\sinh\left(\frac{qV_{ba}}{2kT}\right) \quad , \tag{4.92}$$

where $p(0)$ is the hole concentration at the center of the grain, as defined by Eq. 4.91. If $V_{ba} << 2kT/q$, then

$$J = q^2 p(0)\left(\frac{1}{2\pi m_h^* kT}\right)^{0.5} \exp\left(\frac{-qV_B}{kT}\right)V_{ba} \quad . \tag{4.93}$$

Over the linear J-V range, barrier resistivity (defined as the electric field divided by current density) is written as

$$\rho_B = \frac{V_{ba}}{J(2W)} = \frac{1}{2Wq^2 p(0)}(2\pi m_h^* kT)^{0.5} \exp\left(\frac{qV_B}{kT}\right) \quad , \tag{4.94}$$

and, similarly, crystallite-bulk resistivity takes the form of

$$\rho_c = \frac{V_c}{J(L-2W)} \quad , \tag{4.95}$$

where V_c is the voltage across the crystallite neutral region. Total resistivity, which includes ρ_B and ρ_c is

$$\rho = \frac{V_g}{JL} = \rho_B\left(\frac{2W}{L}\right) + \rho_c\left(1 - \frac{2W}{L}\right) \quad . \tag{4.96}$$

Substituting Eqs 4.94 and 4.95 into Eq. 4.96 this equation results in a general expression for polysilicon resistivity. Interpretation of carrier mobility in nonhomogeneous polysilicon is based on the assumption that an effective mobility μ_{eff} exists such that

$$\rho = \frac{1}{q\bar{p}\mu_{eff}} \quad , \tag{4.97}$$

where the average carrier concentration $\bar{p}$ is defined as

$$\bar{p} = \frac{\int_{-L/2}^{L/2} p(x)dx}{L} \quad , \tag{4.98}$$

with $p(x)$ being the carrier concentration at point x determined by Fermi-Dirac statistics (Pike and Seager, 1979) to be

$$p(x) = n_i \exp\left(-\frac{qV(x) + E_F}{kT}\right) \quad . \tag{4.99}$$

By combining Eqs 4.96 and 4.97, μ_{eff} (including both barrier and bulk motilities) can be obtained.

4.3.1.4. Calculations of W, V_B, E_F, $p(0)$, and $\bar{p}$

This section derives the quantities W, V_B, E_F, $p(0)$, and $\bar{p}$ required for the calculation of ρ and μ_{eff}. For small bias, E_F is assumed to be constant throughout the grain. The effective trapping state density Q_T^+ (ionized trap density in the grain boundary) is related to the number of traps Q_T through the Fermi-Dirac statistics at temperature T (Seto, 1975; Spenke, 1958) as follows:

$$Q_T^+ = \frac{Q_T}{1 + 2\exp\left[\dfrac{(E_F - E_T)}{kT}\right]} \quad , \tag{4.100}$$

where the degeneracy factor is 2 because the traps are assumed to be identical and without interaction, and each can trap one hole of either spin. It is also assumed that E_T is located at a constant energy e_T with respect to E_i at the grain boundary, which is bent down by $-qV_B$ in relation to E_{io}. Therefore,

$$E_T = e_T - qV_B \quad . \tag{4.101}$$

Combining Eqs. 4.100 and 4.101 the above two equations and the charge–neutrality condition, which equates the number of ionized dopants in the depletion region to the number of charged traps, we obtain

$$2NW = \frac{Q_T}{1 + 2\exp\left[\dfrac{(E_F - e_T + qV_B)}{kT}\right]} \quad . \tag{4.102}$$

Because Q_T and L are finite, there is a certain doping concentration N^* at which the grains are totally depleted if $N \le N^* \ (2W = L)$. Otherwise, the grains are only

partially depleted $2W < L$. At $N = N^*$, the Fermi level does not yet differ from that in the neutral region and is

$$E_F = -kT \ln\left(\frac{N^*}{n_i}\right) \quad . \tag{4.103}$$

Based on Eqs 4.89, 4.102, and 4.103, and $(2W = L)$, N^* is iteratively determined[1] to be

$$N^* = \frac{Q_T}{L} - 2n_i \exp\left(\frac{-e_T}{kT}\right)\exp\left(\frac{q^2 N^* L^2}{8\varepsilon kT}\right) \quad . \tag{4.104}$$

For a completely depleted region, $N \le N^*$, when $(2W = L)$, we obtain

$$V_B = \frac{qNL^2}{8\varepsilon} \quad , \tag{4.105}$$

and

$$E_F = e_T - qV_B + kT \ln\left(\frac{1}{2}\left(\frac{Q_T}{LN} - 1\right)\right) \quad . \tag{4.106}$$

Then, based on Eqs 4.88, 4.98, and 4.99, the average carrier concentration is

$$\overline{p} = n_i \exp\left(\frac{-E_F}{kT}\right)\left\{\left(\frac{1}{qL}\right)\left(\frac{2\pi\varepsilon kT}{N}\right)^{0.5} erf\left[\frac{qL}{2}\left(\frac{N}{2\varepsilon kT}\right)^{0.5}\right]\right\} \quad , \tag{4.107}$$

which demonstrates that Seto's derivation (Seto, 1975) overestimated p by a factor of $\exp(qV_B/kT)$.

In partially depleted region, $N > N^*$, in midrange of the doping concentrations at medium and high temperatures where silicon is nondegenerate (Pearson and Bardeen,

[1] The partial ionization of dopants is not taken into account because N^* generally occurs in a medium-doping range where the difference can be neglected so as to yield analytical solutions.

1949), the crystallite has both depletion and neutral regions. In the neutral region, the ionized impurity concentration at temperature T (Sze, 1969; Spenke, 1958) is

$$N^+ = \frac{N}{1+2\exp\left[\frac{(E_A - E_F)}{kT}\right]} \quad , \tag{4.108}$$

where E_A is the acceptor impurity level within the forbidden band gap and, for boron (Pearson and Bardeen, 1949), becomes

$$E_A = \frac{-E_g}{2} + 0.08 - 4.3\times10^{-8} N^{\frac{1}{3}} \quad . \tag{4.109}$$

Combining Eqs 4.91, 4.108, and the condition $p(0) = N^+$ yields

$$n_i \exp\left(\frac{-E_F}{kT}\right) = \frac{N}{1+2\exp\left[\frac{(E_A - E_F)}{kT}\right]} \quad . \tag{4.110}$$

By using Eqs 4.89, 4.91, 4.102 and $p(0) = N^+$, W can be calculated to be

$$W = \frac{Q_T}{2N\left[1+2\left(\frac{n_i}{N^+}\right)\exp\left(\frac{-e_T}{kT}\right)\exp\left(\frac{q^2 N W^2}{2\varepsilon kT}\right)\right]} \quad , \tag{4.111}$$

which is significantly different from the expression obtained by Seto (1975). This difference is a result of the discrepancy between Q_T used by Seto and Q_T^+ used by Lu (1981). For a medium doping concentration and for a large grain size (>400Å), Q_T^+ becomes much smaller than Q_T. If Q_T is used rather than Q_T^+, N^* is much larger than that calculated in Eq. 4.104, and a discontinuity occurs near N^* in the ρ versus N curve, Fig. 4.9.

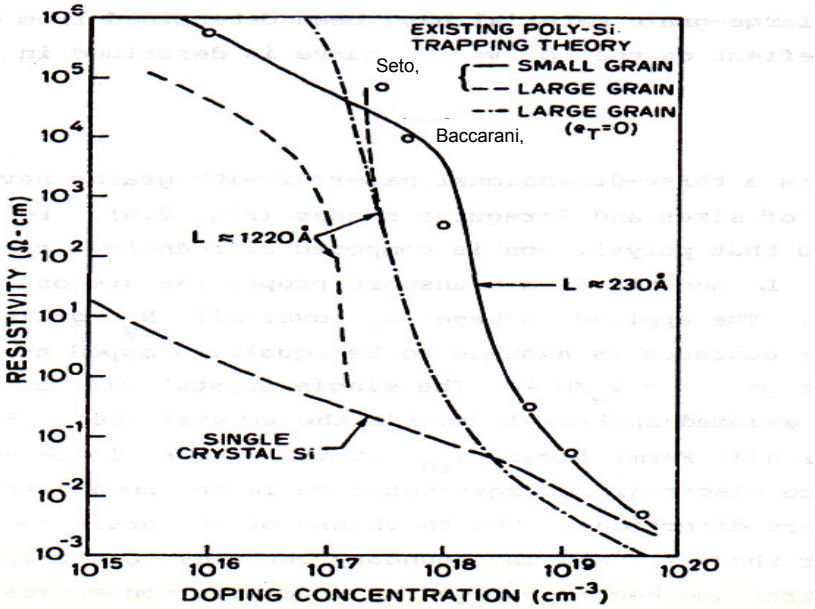

Fig. 4.9. Theoretical room temperature resistivity versus doping concentration of polysilicon film with a grain size of 1220 Å (Lu, 1981).

After W is determined, the carrier concentration in the depletion region becomes

$$p = n_i \exp\left(\frac{-E_F}{kT}\right)\left\{\left(1-\frac{2W}{L}\right)+\left(\frac{1}{Lq}\right)\left(\frac{2\pi\varepsilon kT}{N}\right)^{0.5} erf\left[qW\left(\frac{N}{2kT\varepsilon}\right)^{0.5}\right]\right\} \quad . \quad (4.112)$$

For a very heavy doping concentration (such as $\geq 6.5\times10^{18}$ atoms/cm^3) of boron in silicon, $E_A \approx -E_g/2$ indicates that the valence and impurity bands overlap and the sample will degenerate (Pike and Seager, 1979; Pearson and Bardeen, 1949). Because most impurity atoms are ionized and the depletion region becomes very narrow, the approximation $\bar{p} \approx p(0) \approx N$ is sufficient. The Fermi energy level can be calculated by means of the Fermi integral instead of the Maxwell-Boltzmann approximation (Sze,

1969; Ghandhi, 1977). Figure 4.10 from Lu (1981) plots the measured results of resistivity versus doping concentration obtained by Lu and Seto.

One must also determine m_h^*, ρ, n_i, E_g, E_A, L, Q_T, and e_T. The values of single crystal silicon are assumed for the first five parameters (Muller and Kamins, 1977). Equations 4.85, 4.86, and 4.109 were used to calculate the temperature effect of n_i, E_g, and E_A, respectively. L can be determined by TEM measurements and Q_T and e_T can be obtained from the ρ versus $1/kT$ curves. L, Q_T, e_T terms are derived for undoped and doped materials.

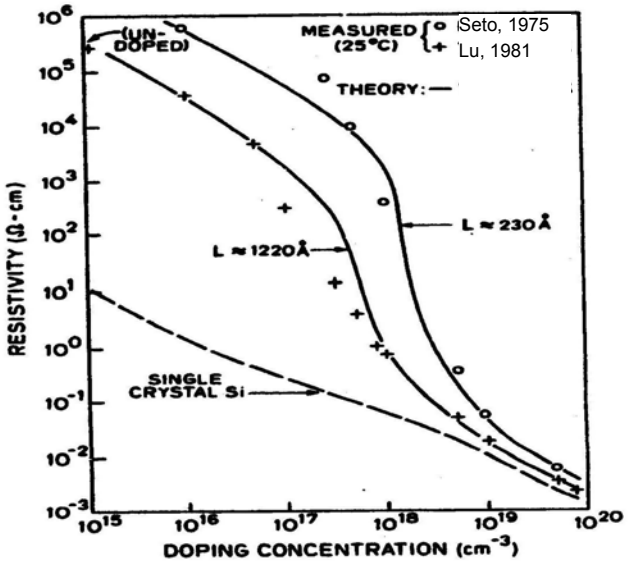

Fig. 4.10. Measured and theoretical resistivities versus doping concentration at room temperature for polysilicon films with various grain sizes and for single crystal (Lu,1981).

The behavior of ρ versus $1/kT$ curves as seen in Fig. 4.11 is nearly Arrhenius (Bassett, 1970) from 25°C to 144°C in undoped and all-doped samples. The activation energy from ρ versus $1/kT$ can be defined as

$$E_a = \frac{\partial(\ln \rho)}{\partial\left(\frac{1}{kT}\right)} \quad . \tag{4.113}$$

Experimental values of E_a as a functional N are illustrated in Fig 4.12. In undoped samples, it is assumed that μ_n and μ_p are proportional to $T^{-3/2}$ (Wolf, 1969). By neglecting the ρ_{GB} term in Eq. 4.83, $E_a \approx E_g/2$; in silicon, $E_g \approx 1.12$ eV. In an undoped sample, therefore, E_a is predicted to be 0.56 eV which is in good agreement with the experimental value of 0.55 eV. In addition, at $T = 300$°C, $n_i = 1.45\times10^{10}$ atoms/cm^3, $\mu_n =$ 1400 cm^2/Vsec, and $\mu_p = 525$cm^2/Vsec (Muller and Kamins, 1977), and ρ_c is calculated to be 2.3×10^5 Ω-cm. The experimentally measured resistivity of undoped polysilicon, which depends on deposition conditions and grain size, is approximately 2 to 8×10^5 Ω-cm.

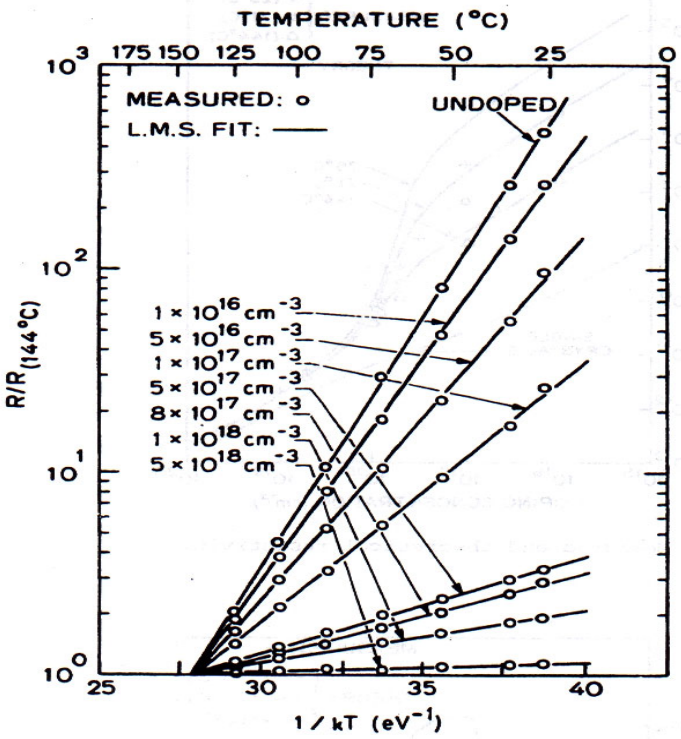

Fig. 4.11. Measured resistivity versus $1/kT$ in samples with different doping concentrations at 25°C and 144°C. The solid lines denote the linear least-term square approximation to the data (Lu, 1980).

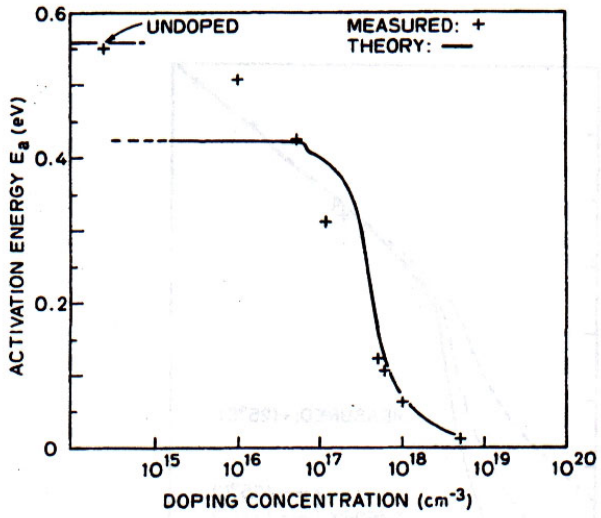

Fig. 4.12. Experimental and theoretical activation energy versus doping concentration (Lu, 1981).

In doped samples, the distribution of grain size can be obtained by dark-field TEM. The number of grains is in proportional to resistor length, and this fact supports the assumption that the transport in polysilicon is nearly one-dimensional through cubic grains. The parameter Q_T and e_T can be affected by the following parameters (Lu, 1981)

For $N \leq N^*$, inserting Eqs 4.85, 4.91, 4.106 and $2W = L$ into Eq. 4.94 results in

$$\rho \propto T^{-1} \exp\left[\frac{\left(\frac{E_g}{2} + e_T\right)}{kT}\right] \quad , \tag{4.114}$$

and, from Eq 4.110,

$$E_a \approx \frac{E_g}{2} + e_T + kT \quad , \tag{4.115}$$

where E_a and E_g are in eV. For $N > N^*$, the following conditions are considered. If N is close to N^*, $Q_T^+ << Q_T$, and V_B becomes a complicated function of temperature as dose ρ, and E_a cannot be expressed in a useful analytical form.

When N increases, $Q_T^+ \approx Q_T$ and $p(0)$ becomes a weak function of temperature. From Eq. 4.94,

$$\rho \propto T^{0.5} \exp\left(\frac{qV_B}{kT}\right) \quad , \tag{4.116}$$

and, from Eq. 4.110

$$E_a \approx qV_B - \frac{1}{2}kT \quad . \tag{4.117}$$

If the sample is more heavily doped, the resistivity contains barrier and bulk components and, therefore, its temperature behavior is affected by both components.

The experimental data (Lu, 1981) demonstrate that the second condition ranges from 5×10^{17} to 1×10^{18} atoms/cm^3 and is suitable for determining Q_T. Therefore, E_a, e_T, and Q_T for different doping concentration and grain size are determined experimentally (Lu, 1981; Seto, 1975) with the results summarized in Tables 4.5 and 4.6.

Table. 4.5. Trapping state energy and density with different doping concentrations (Lu, 1981).

N	E_a	e_T	Q_T
(atoms/cm^3)	(eV)	(eV)	(atoms/cm^2)
1 x 10^{16}	0.51	-0.076	NA
5 x 10^{16}	0.43	-0.156	NA
1 x 10^{17}	0.32	-0.266	NA
5 x 10^{17}	0.115	NA	1.8x10^{12}
8 x 10^{17}	0.1	NA	2.1x10^{12}
1 x 10^{18}	0.06	NA	1.9x10^{12}

Table. 4.6. Trapping state energy and energy barrier height with different doping concentrations (Seto, 1975).

N	E_B	Q_T
(atoms/cm^3)	(eV)	(atoms/cm^2)
1 x 10^{18}	0.0335	2.98 x 10^{12}
1 x 10^{18}	0.022	3.41 x 10^{12}
1 x 10^{18}	0.005	3.64 x 10^{12}

N^* calculated at room temperature is approximately 7.3×10^{16} cm^{-3}. Although $N = 1\times10^{17} > N^*$ its E_a is close to the completely depleted conditions and can still be applied for estimating e_T. After L and Q_T are determined, the value of e_T should be adjusted to produce the best fit of the ρ versus N, μ versus N, and ρ versus $1/kT$ curves (Lu, 1981).

Once the parameters are determined, data for ρ versus N and μ versus N can be more accurately modeled by introducing f (Lu, 1981) into Eq. 4.94, i.e.,

$$\rho_B = \frac{1}{f}\frac{1}{2Wq^2 p(0)}(2\pi m_h^* kT)^{\frac{1}{2}} \exp\left(\frac{qV_B}{kT}\right) \quad . \tag{4.118}$$

Figure 4.13 is a flow chart of the computer program for this modeling, and the parameter values chosen to fit the data are listed in Table 4.7. The trapping-state energy remains at approximately the same level as the grain size is varied, and Q_T decreases with increasing grain size. This can be expected as a result of a reduction in the degree of disorder in the material as it changes from polycrystalline toward single crystal.

Table. 4.7. Parameter values to fit data of polysilicon films with different grain sizes.

Data Source	e_T	Q_T	L	f
	(eV)	(atoms/cm^2)	(Å)	
Seto (1975)	-0.18	$3.34\text{x}10^{12}$	230	0.12
Lu (1981)	-0.17	$1.9\text{x}10^{12}$	1220	0.06

4.3.2. Design criteria and scaling limits for monolithic polysilicon resistors

Some conceptual and fabrication limitations influence modeling of polysilicon as a temperature sensor. In order to save the space on the die after scaling, the following should be satisfied: measurable resistivity with good control, a small voltage coefficient, and small parasitic capacitance. Since the polysilicon resistor is used as a temperature sensor in this work, it should have high temperature sensitivity. Based on the existing model (Lu, 1981; Seto, 1975), this section proposes a quantitative design criterion for a MEMS temperature sensor using polysilicon resistors. The parameters that limit the scaling of these devices are identified.

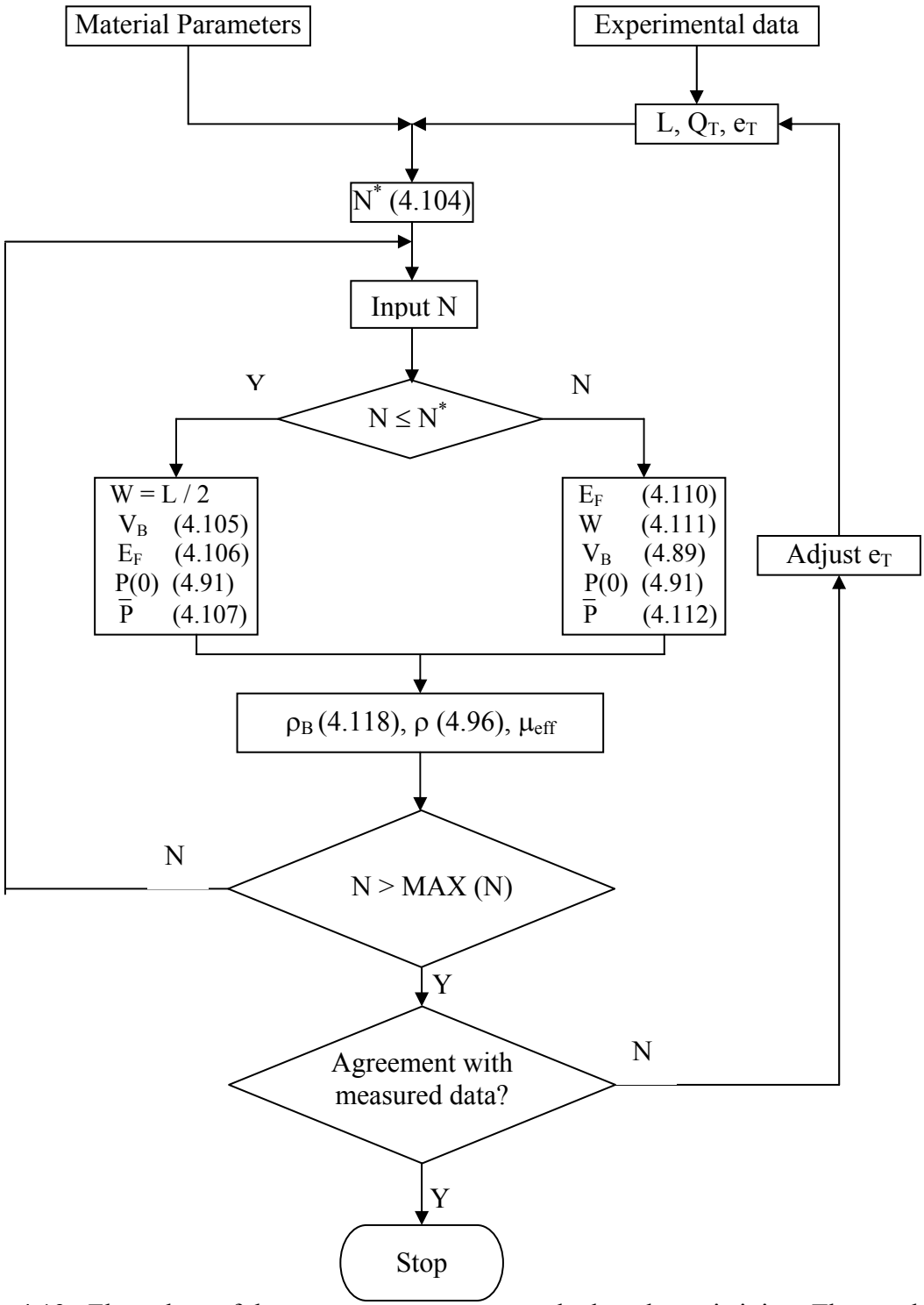

Fig. 4.13. Flow chart of the computer program to calculate the resistivity. The numbers in the parentheses are the equation numbers.

4.3.2.1. Voltage coefficient of resistance

The voltage coefficient of resistance (VCR) is a measure of the nonlinearity of resistors and is defined as the sensitivity of resistance to voltage. The dc and ac voltage coefficients are expressed as (Lu, 1981)

$$VCR_{dc} = \frac{\left(\frac{dR}{R}\right)}{\left(\frac{dV}{V_a}\right)} \quad , \tag{4.119}$$

$$VCR_{dc} = \frac{\left(\frac{dr}{r}\right)}{\left(\frac{dV}{V_a}\right)} \quad , \tag{4.120}$$

where $R = V_a/I$ is the dc resistance at applied voltage V_a, and r is the ac (or small-signal), resistance at V_a is expressed as

$$r = \frac{dV}{dI} \quad , \qquad \text{at} \quad V = V_a . \tag{4.121}$$

Although polysilicon resistors have a high degree of linearity compared to the other resistors, this linearity is limited by the thermionic field emission of majority carriers which is a nonlinear process that governs the transport mechanism. Based on Eqs 4.111 and 4.119, the VCR_{dc} can be written as

$$VCR_{dc} = 1 - \frac{qV_a}{2N_g kT} \coth\left(\frac{qV_a}{2N_g kT}\right) \quad , \tag{4.122}$$

and, based on Eqs 4.111, 4.120, and 4.121, the VCR_{ac} can be also expressed as

$$VCR_{ac} = -\frac{qV_a}{2N_g kT}\tanh\left(\frac{qV_a}{2N_g kT}\right) \quad . \tag{4.123}$$

The grain voltage is $V_g \approx V_a/N_g$, where N_g is the number of grains between the contacts. Equations 4.122 and 4.123 indicate that the nonlinearity of polysilicon resistors approaches zero when $V_g << 2kT/q$. A lower applied bias, longer resistor, or smaller grain size can reduce V_g to enhance linearity. Figures 4.14 and 4.15 from Lu (1981) are design graphs for both dc and ac VCR_{dc} versus V_g at room temperature, respectively. At higher V_g, the absolute values of VCR increase and the resistance values become smaller in comparison to the zero-biased values. For example, at $V_g \approx 0.22$ V, Fig. 4.14, the resistance value is approximately 10% of its zero-biased value, and a 1% change in applied bias can cause an approximately –3.5% variation in resistance.

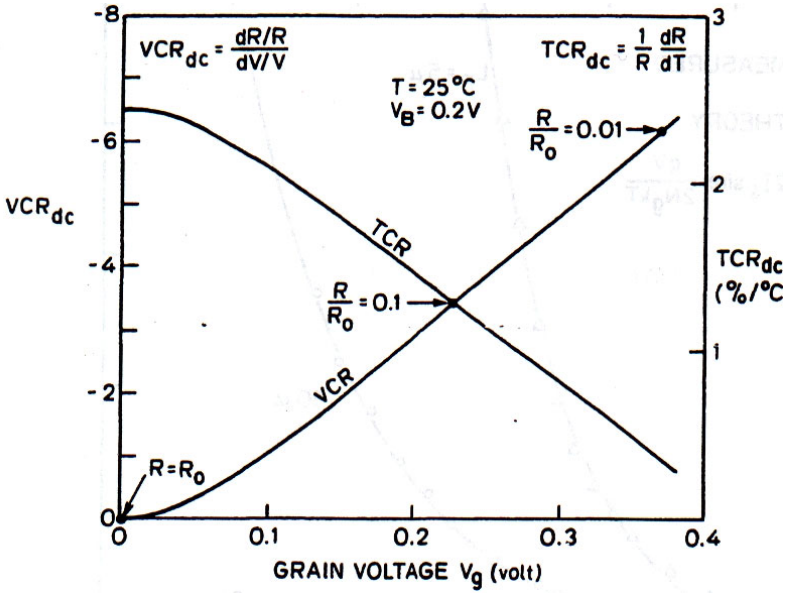

Fig. 4.14. The dc voltage and temperature coefficients and the ratio of R to zero bias R_o in polysilicon resistors versus grain voltage (Lu, 1981).

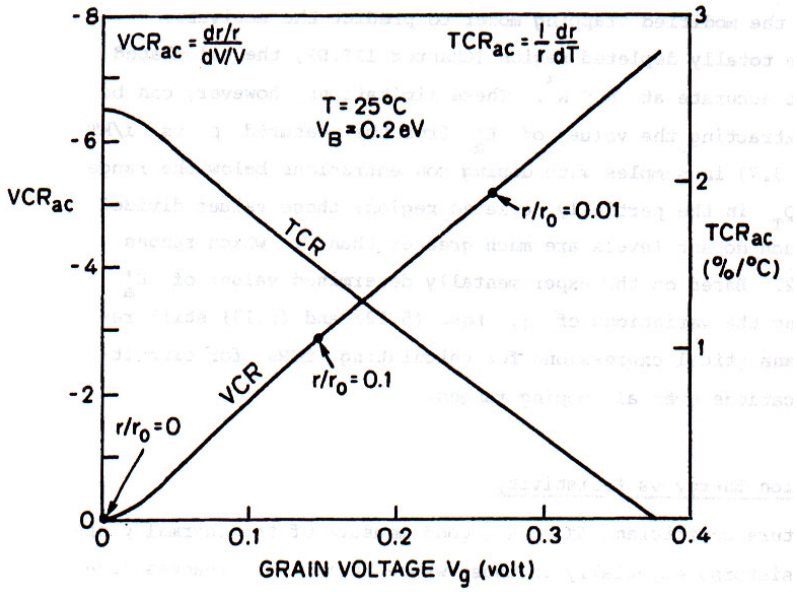

Fig. 4.15. The ac voltage and temperature coefficients and the ratio of r to zero bias r_o in polysilicon resistors versus grain voltage (Lu,1981).

4.3.2.2. Temperature coefficient of resistance

The temperature coefficient of resistance (*TCR*) is a measure of the thermal sensitivity of resistors and is defined as the ratio of resistance change versus temperature variation to resistance value. The dc and ac temperature coefficients resistance are defined as

$$TCR_{dc} = \frac{1}{R}\frac{dR}{dT} \quad , \tag{4.124}$$

$$TCR_{ac} = \frac{1}{r}\frac{dr}{dT} \quad . \tag{4.125}$$

It has been reported that both negative and positive TCRs were measured for polysilicon under different processing condition (King, et al., 1973). Since polysilicon resistivity is composed of barrier resistivities and crystallite bulk resistivity, the thermal properties are combinations of both barrier and bulk resistivities. Barrier resistivities are

the result of thermionic emission processes and have a negative *TCR*. However, bulk resistivity, i.e., the resistivity of single-crystal silicon and a function of carrier concentration and mobility, has a positive *TCR*. Bulk resistivity is greater than barrier resistivity when the samples have large grains and/or high doping concentration. Therefore, the polysilicon will have positive *TCR*s. In medium or lightly doped samples and/or small grain sizes, barrier resistivities dominate and the polysilicon has a negative *TCR*. These characteristics are obtained from Eq. 4.96. In addition, since the polysilicon resistors are generally operating in the temperature range of 0°C to 150°C, the following derivation is primarily based on the trapping model, which was explained in section 4.4. *TCR*s at any doping concentration can be exactly calculated by using Eqs 4.124 and 4.128 and the definitions of *R* and *r*. The results (Lu, 1981) obtained in Eqs 4.92 and using $J = \frac{I}{A}$, *I* can be rewritten as

$$I = 2Aqp(0)\left(\frac{kT}{2\pi m_h^*}\right)^{0.5} \exp\left(\frac{-qV_B}{kT}\right)\sinh\left(\frac{qV_a}{2N_g kT}\right) \quad , \tag{4.126}$$

To obtain a deeper insight, the *TCR*s were derived analytically over specific doping concentration ranges (Lu, 1981). Therefore, *I* for this specific range can be obtained by,

$$I = kT^{\gamma} \exp\left(\frac{-E_a'}{kT}\right)\sinh\left(\frac{qV_a}{2N_g kT}\right) \quad , \tag{4.127}$$

where γ is a constant and E'_a in the exponential term is different from the activation energy E_a which are defined later. Using $R = V_a/I$ and inserting Eq. 4.127 into Eq 4.124 we obtain

$$TCR_{dc} = -\frac{1}{T}\left[\frac{E'_a}{kT} + \gamma - \frac{qV_a}{2N_g kT}\coth\left(\frac{qV_a}{2N_g kT}\right)\right] \quad , \tag{4.128}$$

and, similarly, inserting Eqs 4.121 and 4.127 into 4.125 yields

$$TCR_{dc} = -\frac{1}{T}\left[\frac{E'_a}{kT} + \gamma - \frac{qV_a}{2N_g kT}\tanh\left(\frac{qV_a}{2N_g kT}\right)\right] \quad . \tag{4.129}$$

Equations 4.128 and 4.129 can be used to calculate TCR_{dc} and TCR_{ac} in a totally depleted grain, where $E_a' = E_g/2 + e_T$ and $\gamma = 2$ and, in a partially depleted sample where $Q_T^+ \approx Q_T$, $E_a' = qV_B$ and $\gamma = 1/2$. In a partially depleted sample, assuming that $V_B = 0.2$ V, the above calculated values of TCR_{dc} and TCR_{ac} at room temperature were plotted versus V_g in Figs 4.14 and 4.15, respectively.

4.3.2.3. Optimization of properties of polysilicon resistors

Because of the high sensitivity of resistance to processing conditions and the complicated physical transport properties, utilization of polysilicon resistors is not as simple as with ohmic resistors. If the dose of doping concentration is $\leq 5 \times 10^{14}$ atoms/cm^2, then using Fig 4.16, large negative TCR can be obtained in the range of 4 %/°C (depending on the thermal process, and grain size) (Luder, 1986). When the dose of doping concentration is greater than 5×10^{13} atoms/cm^2 the normalized resistivity is a

straight line over the whole temperature range (4ºC to 144ºC). In the other region where the doping concentration is less than 5×10^{13} atoms/cm^2, the relationship is found to be linear only for a temperature greater than 50ºC. For doses < 5×10^{13} stoms/cm^2, the resistivity is nearly independent of doping concentration for phosphorus doped samples, but for boron doped samples, it decreases with increasing doping concentration. In the intermediate doping concentration range, 5×10^{13} atoms/cm^2 $\le N \le 5\times10^{14}$ atoms/cm^2, the characteristics are well explained by the trapping model. When the doping concentrations are greater than 5×10^{14} atoms/cm^2, the temperature depended is less significant than that predicted. These properties can be used for designing the temperature sensors. Therefore, the doses in the range between 5×10^{13} to 5×10^{14} atoms/cm^2 are selected for this work, and doping concentrations are calculated in this range as following.

The spatial distribution of dopant into the substrate surface tends to follow a Gaussian (or normal) distribution as illustrated on the right side of Fig. 4.16.

According to Ruska (1987), the concentration of dopant $N(x)$ may be determined from the following equation:

$$N(x) = \frac{Q}{\sqrt{2\pi}\Delta R_p} \exp\left[\frac{-(x - R_p)^2}{2\Delta R_p{}^2}\right] \quad , \tag{4.130}$$

where R_p is the projected range, ΔR_p is the scatter or "straggle", and Q is the dose of the ion beam (atoms/cm^2). The doping ranges for selected dopant in silicon substrate are given in Table 4.8.

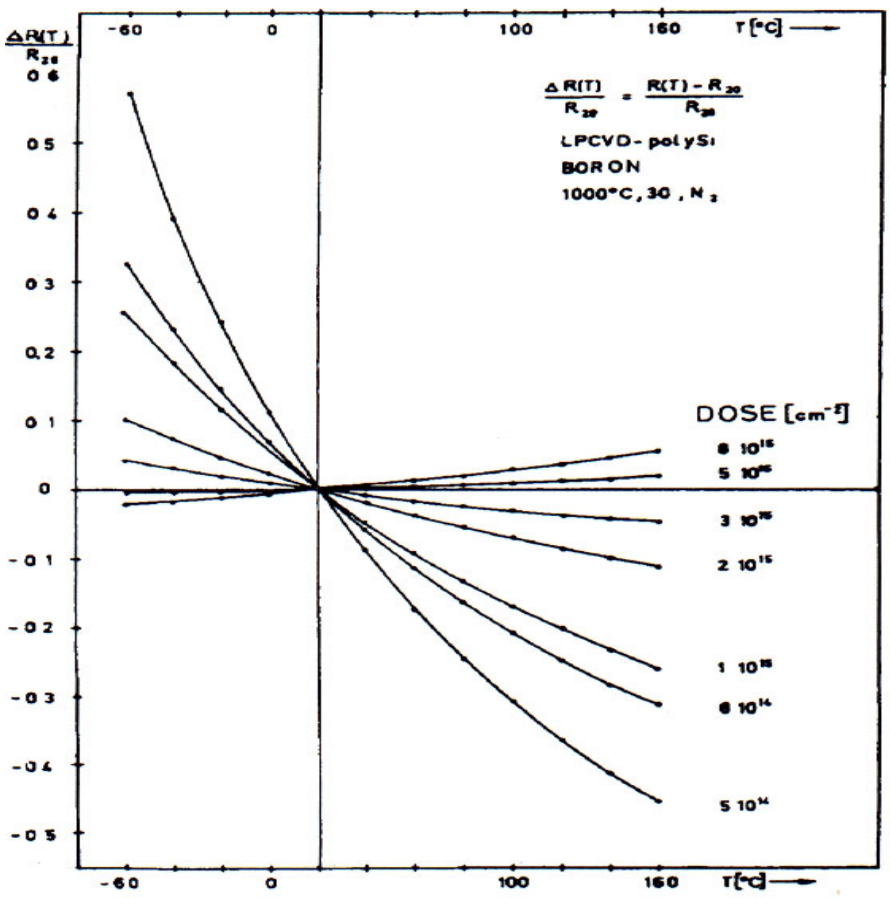

Fig. 4.16. Relative change of resistance as a function of temperature T in LPCVD polysilicon layers with boron implantation dose as a parameter (Luder, 1986).

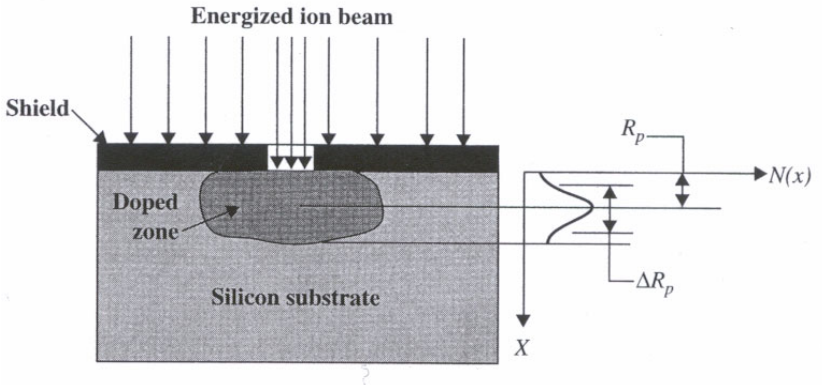

Fig. 4.17. Distribution of dopant through a shield (Ruska, 1987).

Table. 4.8. Ion implantation of common dopants in silicon (Ruska, 1987).

Ion	Range, R_p, nm	Straggle, ΔR_p, nm
At 30 keV energy level		
Boron (B)	106.5	39.0
Phosphorus (P)	42.0	19.5
Arsenic (AS)	23.3	9.0
At 100 keV energy level		
Boron (B)	307.0	69.0
Phosphorus (P)	135.0	53.5
Arsenic (AS)	67.8	26.1

Boron implantation with high energy level (100keV) is used in this work. Therefore, the doping concentration will be in the range of 9×10^{17} atoms/cm^3 to 9×10^{18} atoms/cm^3.

The parameters related to these requirements are based on resistor dimensions, applied voltage, doping concentration, and grain size. The code (Appendix B) was written based on the flowchart of Fig 4.13 to calculate the resistivity of polysilicon.

4.3.2.3.1. Physical limits

In order to minimize the small dimensions, at least one grain boundary must be contained within the resistor, which necessitates a minimum resistor length corresponding to approximately two grains. The smallest grain size is determined by electrical breakdown of the material. For example, with a supply voltage of 0.5 V (lowest voltage predicted by NMOS scaling) (Ratnakumar, et al., 1980), the maximum tolerable electric field of an intrinsic silicon material of approximately 3×10^5 V/cm (Sze, 1969) requires a minimum grain size greater than 85 Å (i.e., the minimum resistor length

larger than 170Å). In addition, it has been reported that high current can melt the grain boundary layer to reduce resistivity (Kato, et al., 1980) or can change the structure of highly resistive polysilicon to lower resistivity irreversibly.

4.3.2.3.2. Circuit limits

The ultimate two-grain structure cannot meet the circuit requirements. Using Figs 4.14 and 4.15, lower and upper limits on grain voltage can be set from the circuit specifications on VCR. For example, a circuit has a supply voltage with instability of 10% (dV/V=10%) and the current variation caused by this bias accuracy restricted to below 20% to avoid circuit malfunction. From the relationship defined by $dI/I=dV/V-dR/R$ and the definition of VCR_{dc}, the above condition requires an absolute tolerance of VCR_{dc} <1. However, VCR and TCR are maximum when V_g is 0.1V according to Figs 4.14 and 4.15. In addition, VCR and especially TCR are the major factors in designing of the temperature sensor, therefore the maximum V_g is determined to be approximately 0.1 V. Thus for a 5 V supply voltage across the polysilicon resistor, and using $V_g = V/N_g$, the number of grains is found to be $N_g \geq 50$. Similarly, if the supply voltage is scaled down to 0.5V, five grains are sufficient to maintain the maximum grain voltage of 0.1V.

The smallest resistors length can be achieved with a minimum grain size of 250Å. Thus, the smallest resistor length for 50 grains is 1.5 μm. If the supply voltage is scaled down to 0.5V, five grains are sufficient to maintain the maximum grain voltage of 0.1 V and the minimum device size becomes 0.15 μm.

Because linear applications generally demand more stringent linearity then do digital applications, the minimum device length should be longer.

4.3.2.4. Determination of parasitic capacitance

In polysilicon resistor with length L_R, width W_R, and thickness t_R on an oxide layer of thickness h_{ox}, resistance, R_e, takes the form of

$$R_e = \frac{\rho L_R}{W_R h_R} \quad . \tag{4.131}$$

The two parasitic capacitances associated with this resistor are the lateral intrinsic capacitance of polysilicon and the vertical oxide capacitance to the substrate, which are defined as

$$C_L = \varepsilon_{poly} \frac{W_R h_R}{L_R} \quad , \tag{4.132}$$

$$C_V = \varepsilon_{SiO_2} \frac{W_R L_R}{h_{ox}} \quad , \tag{4.133}$$

where ε_{poly} and ε_{SiO2} are the permittivities of polysilicon and oxide, respectively.

Defining a device-scaling factor as $SF \geq 1$ and reducing all dimensions, this SF factor increases R and lowers C_L and C_V. To maintain a constant R_e, resistivity should be reduced by the same factor. In a polysilicon resistor, C_L is less important than C_V because of longer L_R and smaller h_R and h_{ox}. When scaling down to small geometry, however, C_L becomes significant, which can be seen in the ratio of

$$\frac{C_L}{C_V} = \frac{\varepsilon_{poly}}{\varepsilon_{SiO_2}} \frac{h_{ox} h_R}{{L_R}^2} \quad . \tag{4.134}$$

In the state-of-the-art polysilicon resistors $L_R = W_R = 5$ μm, $h_{ox} = 0.5$ μm, and $h_R = 0.3$ μm, then,

$$\frac{C_L}{C_V} = \frac{\varepsilon_{poly}}{167\varepsilon_{SiO2}} \quad , \tag{4.135}$$

and $C_V \approx 1.7 \times 10^{-15}$ F. Scaling L_R and W_R down to 0.5 μm and $h_R = 0.1$ μm, then $C_L/C_V = \varepsilon_{poly}/5\varepsilon_{SiO2}$ and $C_V \approx 8.5\times 10^{-17}$ F. As a result, C_L cannot be neglected in small-dimension polysilicon resistors, especially over low frequency ranges.

5. COMPUTATIONAL CONSIDERATIONS OF MEMS SENSORS

5.1. Pressure sensors

5.1.1. Computational model

Knowing strain distribution in the diaphragm under bending, the sensitivity of the pressure sensor can be optimized by placing the polysilicon strain gauges at the locations of the maximum strains, as described in section 4.1. The maximum S_y can be determined using Eq. 5.1 for maximum pressure (2 atm) and dimensions of the diaphragm.

In addition to the analytical developments of section 4.1, a computational finite element method (FEM) model was developed using COSMOS/M software (SRAC, 2003). Because of symmetry of the diaphragm, half-model was used, Fig. 5.1.

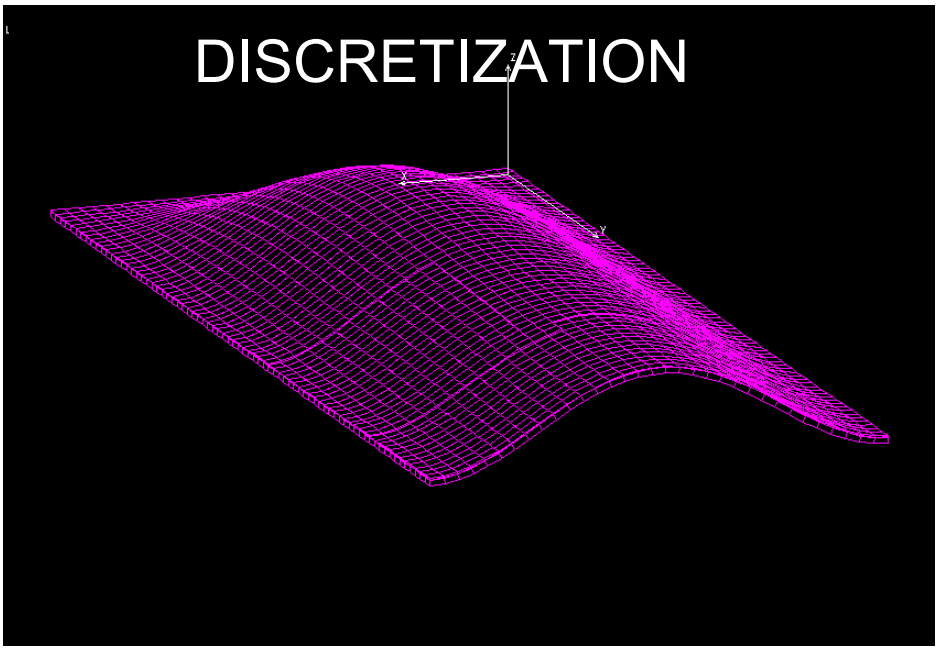

Fig. 5.1. Half model of FEM analysis of MEMS pressure sensor.

5.1.2. Determination of convergence

By considering the analytical value for maximum stress (σ_{anal} = 562.5 MPa, based on Eq. 4.25), the number of elements for the finite element analysis was increased until the computed stress approached the analytical value. The percentage difference between these values was calculated using the following equation:

$$\%Diff = \frac{\sigma_{anal} - \sigma_{comp}}{\sigma_{anal}} 100\% \quad , \tag{5.1}$$

where σ_{anal} is the analytically determined maximum stress in the diaphragm and σ_{comp} is the computationally determined maximum stress in the diaphragm using FEM model based on a specific number of elements.

5.1.3. Determination of deformations

Since the magnitude of the maximum deformation is expected to be on the order of thickness of the diaphragm, one has to consider large deformation (geometrically nonlinear) in the analysis. Therefore, to determine the area of uniform distribution of strain in *y*-direction along the centerline, the analytical solution needs to consider large deflections of a clamped rectangular diaphragm in bending under normal pressure. Results published by Levy and Greenman (1942) and Ramberg, et al., (1942) indicate that clamped rectangular diaphragms with a length to width ratio greater than 1.5 should be regarded, for purpose of analysis, as an infinitely long diaphragm. Since this ratio is equal to 5, for the diaphragm used in this thesis, calculation for an infinite diaphragm

should be performed. Figure 5.2 shows the stress ratio versus pressure ratio for the clamped diaphragms with a Poisson ratio of 0.316, which have large deformation. The pressure ratio, R_p, and the stress ratio, R_s, used in Fig. 5.2, are defined as

$$R_p = \frac{pa^4}{Eh^4} \quad , \tag{5.2}$$

$$R_s = \frac{S_y a^2}{Eh^2} \quad , \tag{5.3}$$

where p, a, E, h and S_y are the uniform pressure, the width of diaphragm, the modulus of elasticity, the thickness of the diaphragm, and the stress in y-direction, respectively. Results obtained using Eqs 5.2 and 5.3 are presented in section 7.1.

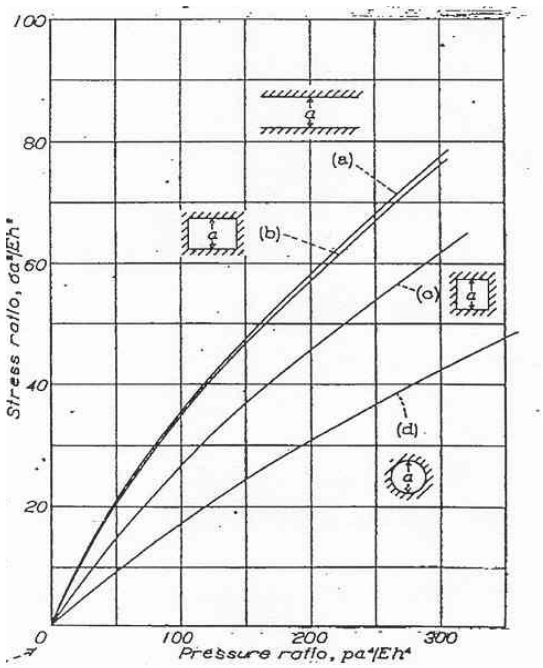

Fig. 5.2. Stress ratio versus pressure ratio for: (a) infinitely long rectangular plate, (b) rectangular plate of 3:2 ratio, (c) square plate and (d) circular plate (Levy and Greenman, 1942; Ramberg, et al., 1942).

5.1.4. Determination of strains and stresses

Strain and stress fields in the diaphragm of the MEMS pressure sensor were determined using the computational model. Results of these computations are presented in section 7.1.

5.2. Relative humidity sensors

5.2.1. Computational model

The solution of transient mass diffusion in the humidity sensor was obtained by comparison with the transient heat conduction. Conduction of heat inside a solid with constant thermal conductivity is represented by the following differential equation:

$$\frac{\partial T}{\partial t} = \frac{k}{\rho c}\left(\frac{\partial^2 T}{\partial x^2} + \frac{\partial^2 T}{\partial y^2} + \frac{\partial^2 T}{\partial z^2}\right) \quad , \tag{5.4}$$

where ρ, k, c, and T are the thermal conductivity (W/m-K), density (kg/m^3), and specific heat (J/kg-K), and temperature (K), respectively. The term $\frac{k}{\rho c}$ in Eq 5.4 is called the thermal diffusivity κ (m^2/sec). Therefore, Eq 5.4 can be rewritten as

$$\frac{\partial T}{\partial t} = \kappa\left(\frac{\partial^2 T}{\partial x^2} + \frac{\partial^2 T}{\partial y^2} + \frac{\partial^2 T}{\partial z^2}\right) \quad . \tag{5.5}$$

Also, diffusion of mass inside a solid can be described by

$$\frac{\partial M}{\partial t} = D\left(\frac{\partial^2 M}{\partial x^2} + \frac{\partial^2 M}{\partial y^2} + \frac{\partial^2 M}{\partial z^2}\right) \quad , \tag{5.6}$$

where D and M are the diffusion constant (m^2/sec) and mass concentration ($1/m^3$), respectively. Comparing Eqs 5.5 and 5.6 the thermal diffusivity κ and the temperature T correspond to the diffusion constant D, and the mass concentration M, respectively. As a result of solutions to the heat conduction equation can be used for describing the mass concentration. In the simulation, the density and the specific heat have been set to 1 so that the conductivity becomes equal to the thermal diffusivity and diffusion constant. The transient moisture inside the sensor elements has been simulated using the commercial finite-element-method (FEM) simulator, COSMOS/M (SRAC, 2003). In this simulation, the sensitive layer is considered with a length, width, and thickness equal to 1000 μm, 10 μm, and 2 μm, respectively. Usually, the photosensitive polyimide has diffusion constant between 5×10^{-9} and 5×10^{-8} cm^2/sec. The diffusion constant for Ultradel 7501 (Amoco, 1992) was obtained experimentally to be 3×10^{-8} by Kang (1999). Since the metal electrodes are at the top and bottom of the polyimide sensitive layer, the moisture diffusion flux from top to bottom are zero. Therefore, the diffusion within different layers in the z-direction (i.e., thickness direction) does not change. Thus, the plane 2D model can be used for this simulation instead of a 3D model. The initial moisture diffusion rate is assumed to be zero, and the moisture diffusion from four-sides of the plate is considered. The simulation is done for different number of elements.

5.2.2. Determination of convergence

The computational model of section 5.2.1 was used to determine convergence, results of which are presented in section 7.2.

5.2.3. Determination of moisture concentration

Following convergence analysis, the computational model of the relative humidity sensor was used to determine moisture concentration, as discussed in section 7.2.

5.3. Temperature sensors

5.3.1. Computational model

Using equation presented in section 4.3, a computational model for analysis of temperature sensors was developed and is listed in Appendix C.

5.3.2. Determination of resistivity of polysilicon

The computational model of section 5.3 was used to determine resistivity of polysilicon. Representative results of this determination are presented in section 7.3.

6. EXPERIMENTAL CONSIDERATIONS

6.1. Optoelectronic holography methodology

Optoelectronic holography (OEH) methodologies have been successfully applied to different fields of nondestructive testing (NDT) of objects (Pryputniewicz, 1995). OEH methodologies are noninvasive, remote, and with full-field-of-view capable of providing qualitative and quantitative information on shape and deformation of objects subjected to a large variety of boundary conditions and loadings (Furlong and Pryputniewicz, 2000). Implementation of recent technological advances in coherent light sources, computing, imaging, and detector technologies to the OEH has dramatically increased the versatility of the OEH methodologies and added the possibility of using them in microscope based setups to study MEMS structures and to investigate micromechanics of materials used for MEMS fabrication (Furlong and Pryputniewicz, 2001a).

6.1.1. Data acquisition and processing

One OEH approach used to perform shape measurement investigations of objects consists of acquiring and processing two sets, $I(x, y)$ and $I'(x, y)$, of phase-stepped intensity patterns, recorded before and after, respectively, event effects which are to be measured (Furlong and Pryputniewicz and, 2001b). The first set of phase-stepped intensity patterns is described by

$$I_n(x,y) = I_B(x,y) + I_M(x,y)\cos\left[\Delta\phi(x,y) + \theta_n\right] \quad , \tag{6.1}$$

where

$$I_B(x,y) = I_o(x,y) + I_r(x,y) \tag{6.2}$$

is the background irradiance, and

$$I_M(x,y) = 2\left[I_o(x,y)I_r(x,y)\right]^{0.5} \tag{6.3}$$

is the modulation irradiance. In Eqs 6.1 to 6.3 I_o (x, y) and I_r (x, y) are the object (Furlong and Pryputniewicz, 2002) and reference beams irradiances, respectively,

$$\Delta\phi(x,y) = \phi_o(x,y) - \phi_r(x,y) \quad , \tag{6.4}$$

with $\varphi_o(x,y)$ representing a random phase due to light scattering from the object of interest and $\varphi_r(x,y)$ representing a uniform phase from a smooth reference beam wave front. θ_n is the applied nth phase step, the value of which is obtained during calibration procedures applied according to the specific phase stepping algorithm that is implemented, and (x,y) represents Cartesian coordinates of the image space.

The second set of phase-stepped intensity patterns is described by

$$I'_n(x,y) = I_B(x,y) + I_M(x,y)\cos\left[\Delta\phi(x,y) + \Delta\Omega(x,y) + \theta_n\right] \quad . \tag{6.5}$$

In Eq. 6.5, $\Delta\Omega$ (x,y) is the change in the optical phase that occur between acquisition of the two sets of phase-stepped intensity patterns, the value of which relates to the shape or changes in state of deformation of the MEMS pressure sensor (Hanson, et al., 2001). With the OEH, the two sets of phase-stepped intensity patterns are processed in the display and data modes (Furlong, et al., 2002).

In the display mode, secondary interface patterns, $Q_D(x,y)$ are generated, displayed at video rates, and are modulated by a cosinusoidal function of the form

$$Q_D = 4I_M(x,y)\cos\left[\frac{\Delta\Omega(x,y)}{2}\right] = \left\{\left[I_1(x,y) - I_3(x,y) + I_1'(x,y) - I_3'(x,y)\right]^2 + \left[I_2(x,y) - I_4(x,y) + I_2'(x,y) - I_4'(x,y)\right]^2\right\}^{0.5} \quad , \tag{6.6}$$

which represents an 8-bit resolution video image obtained after application of four phase steps: $\theta_n = 0, \pi/2, \pi, 3\pi/2$. The display mode is used for adjusting, in real-time, the experimental parameters for quantitative OEH investigations. Such parameters include (Pryputniewicz, et al., 2000a; Pryputniewicz, et al., 2001c):

1) beam ratio $r = avg[I_r]/avg[I_o]$, which is important to characterize and set in order to obtain appropriate fringe visibility and also to avoid optical saturation of the CCD array detector of the CCD camera,
2) phase step θ_n, which is obtained by calibration and used in order to acquire accurate phase-stepped intensity patterns, $I_n(x,y)$, based on which further processing is conducted.

The data mode is used for quantitative investigations, which involve the determination of $\Delta\Omega(x,y)$, related to the shape and/or deformation, of MEMS pressure sensor. The distribution $\Delta\Omega(x,y)$, modulo 2π, is determined using double-float point arithmetic as (Pryputniewicz, et al., 2000b; Pryputniewicz, et al., 2001d)

$$\Delta\Omega = \tan^{-1}\left[\frac{2(I_2 - I_4)}{2I_3 - I_1 - I_5}\right] \quad , \tag{6.7}$$

where (x,y) arguments have been omitted for clarity. Equation 6.7 corresponds to the implementation of the algorithm with 5-phase-steps $\theta_n = 0, \pi/2, \pi, 3\pi/2, 2\pi$. Application of such an algorithm minimizes errors in determination of $\Delta\Omega(x,y)$ due to possible phase

stepping miscalibration. Recovery of continuous spatial phase distributions $\Delta\Omega(x,y)$ requires the application of efficient phase unwrapping algorithms (Furlong 1999; Furlong and Pryputniewicz, 2001c). Using parallel illumination and observation, the deformation can be approximated as (Pryputniewicz, et al., 2002a; Pryputniewicz, et al., 2003)

$$L_z = \frac{\lambda}{4\pi}\Delta\Omega \quad , \tag{6.8}$$

where L_z is the component of deformation in the direction parallel to the direction of observation and λ is the wavelength of the laser used (Pryputniewicz, et al., 2001f; Pryputniewicz, et al., 2002b).

6.1.2. The OELIM system

Figure 6.1 depicts major components of an optoelectronic holography microscope (OEHM), specifically setup to perform high-resolution shape and deformation measurements of MEMS components (Pryputniewicz, et al., 2000d; Pryputniewicz, et al., 2001). In the configuration shown in Fig. 6.1, the coherent light source is a tunable laser diode (LD) with an operational wavelength centered at 640 nm, 3 mW output power, and TTL modulation capabilities. The output of the LD is directed through a 10x beam expander (BE) and through a beam splitter cube (BS). The BS splits light into reference beam (RB) and object beam (OB). The RB is directed to the piezo-electric phase stepper (PS) and to the CCD detector of a high-speed, high spatial resolution digital camera (CA). The object beam (OB) is directed to the MEMS. Reflected object beam, carrying shape and/or deformation information of the MEMS, is imaged by means of a long-

working distance microscope objective (MO) and condensing lens (CL). After the CL, OB is directed via the BS to the CCD detector of the CA. Spatial intensity distributions detected by the CA are transmitted to an image and video-processing computer (IPC) (Brown and Pryputniewicz, 2000; Pryputniewicz, et al., 2001g). The IPC is capable of synchronizing acquisition of digital video information with data acquisition boards that control modulation of the LD and PS, instrumentation for subjecting MEMS to various loads, as well as positioning of the X-Y-Z stage (XYZ) (Pryputniewicz, 2001).

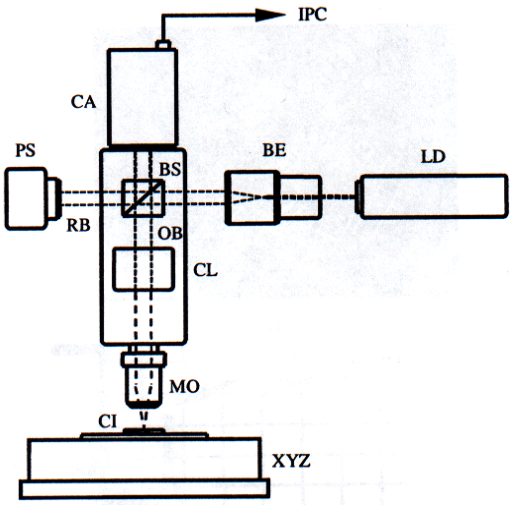

Fig. 6.1. Optoelectronic laser interferometric microscope (OELIM) specifically setup to perform high-resolution shape and deformation measurements of MEMS.

Figure 6.2 shows the MEMS pressure sensor sample from front side and backside. As it can be seen, there is a hole in the back of the diaphragm which is designed for pressurizing the sensor.

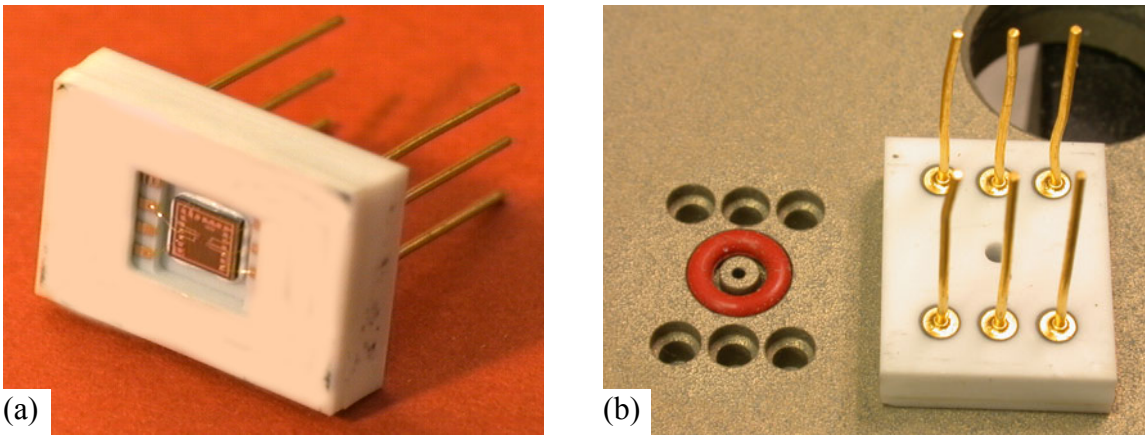

(a) (b)

Fig. 6.2. MEMS pressure sensor: (a) top view, (b) back view.

After the sensor was mounted in the loading fixture, it was assembled on the positioner as a part of the OELIM system.

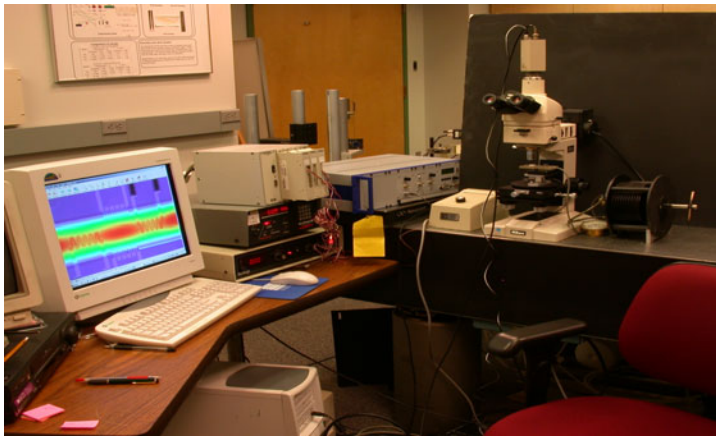

Fig. 6.3. Overall view of the OELIM system for studies of MEMS pressure sensors.

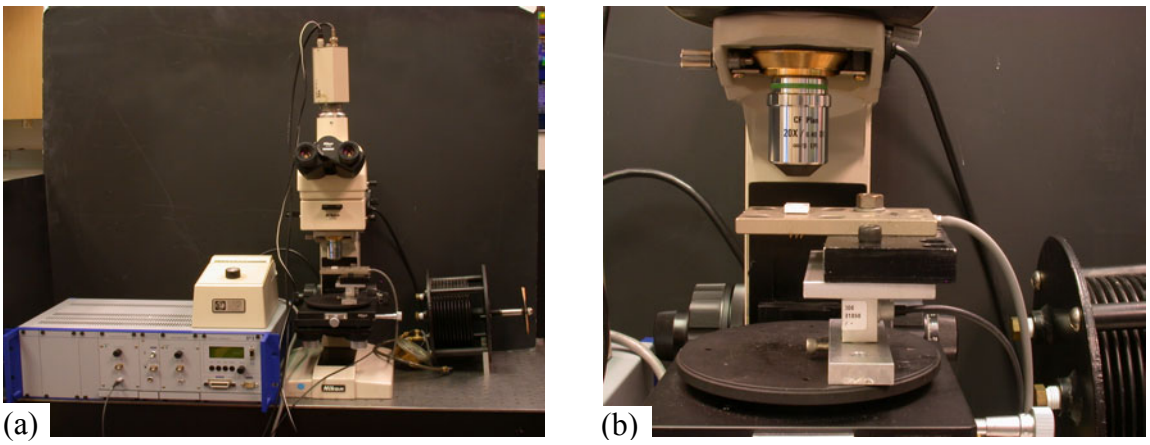

(a) (b)

Fig. 6.4. OEHM system for studies of MEMS sensors: (a) overall view of the imaging and controls subsystems, (b) close up of the MEMS sensor on the positioner and under the microscope objective.

7. REPERESENTATIVE RESULTS AND DISCUSSION

7.1. Pressure sensors

7.1.1. Convergence of stress as a function of number of elements

Using the maximum S_y obtained from the analytical solution (562.5 MPa), the number of elements used in the computational model was optimized for linear static model. After converging the maximum stress to the constant value while maintaining the %Difference under 1%, based on Eq. 5.1, for number of elements greater than 50000.

Table 7.1. Summary of convergence analysis for FEM determined stress in *y*-direction using linear static model at the diaphragm.

Elements				Stress	
Length	Width	Thick	Total elements	S_y max	*% Diff*
10	2	2	40	0.032	668212.5
20	4	2	160	213.86	72.2107921
40	8	2	640	368.29	24.716935
80	16	2	2560	459.32	10.5982757
160	32	2	10240	508	3.34645669
240	48	2	23040	525	0.76190476
240	48	4	46080	529	1.86389414
320	64	4	81920	538.86	1.14872137
400	80	4	128000	545.05	1.67140629
600	120	4	288000	554.16	1.50498051
Analytical solution				562.5	

Using the maximum S_y obtained from the analytical solution, the number of elements used in the computational model was optimized for a Poisson ratio of (ν = 0.24).

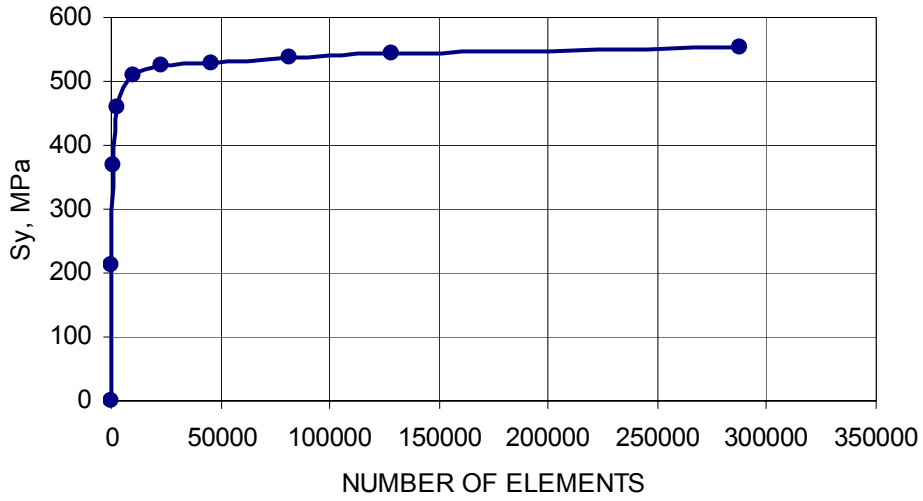

Fig. 7.1. Computational convergence of S_y as a function of number of elements.

After converging the maximum stress to the constant value while maintaining the %Difference under 1%, based on Eq. 5.1, for number of elements greater than 22000, I repeated the same procedure for $\nu = 0.316$ in order to compare the analytical with computational solutions. Table 7.1 and Fig. 7.1 show the maximum stress in y-direction for the diaphragm versus number of elements. In Table 7.1 the relative difference is calculated by using the change in S_y between two segmental steps in which the number of elements has been increased. It can be seen, that when 20,000 or more elements are used the maximum S_y is nearly constant. As one can see in Table 7.1, there is 2.7% difference between the analytical and computational solutions.

Table 7.2. Summary of convergence analysis for FEM determined stress in *y*-direction using nonlinear static model; quarter-model of the diaphragm was used because of the symmetry.

Elements				Stress	
Length	Width	Thick	Total elements	S_y max	*% Diff*
10	2	2	40	209.54	
20	4	2	160	323.06	54.17581
40	8	4	1280	398.55	23.36718
80	16	4	5120	441.79	10.84933
160	32	4	20480	467.36	5.787818
200	40	4	32000	473.5	1.313762
250	50	4	50000	478.99	1.159451
300	60	4	72000	483.17	0.87267
Computational solution with ν= 0.316				497.78	2.777344
Analytical solution with ν = 0.316				512	

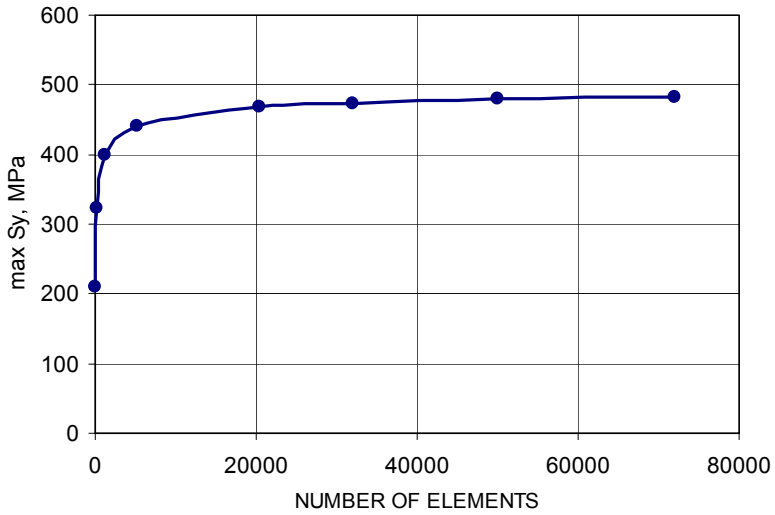

Fig. 7.2. Computational convergence of S_y as a function of number of elements.

Considering a pressure of 2 atm and ν = 0.316, a maximum S_y of 512 MPa was obtained for the clamped diaphragm using nonlinear static analysis based on Fig. 5.3. Please note, the maximum S_y based on the nonlinear analysis (512 MPa) is much lower than that based on the linear analysis (562.5 MPa).

The overall uncertainty in S_y was calculated based on Eq. 5.3 using a code developed as part of this thesis and listed in Appendix C (Pryputniewicz, 1992)

$$\delta S_y = \left\{ \left(\frac{dS_y}{dR_s} \delta R_s \right)^2 + \left(\frac{dS_y}{dE} \delta E \right)^2 + \left(\frac{dS_y}{dh} \delta h \right)^2 + \left(\frac{dS_y}{da} \delta a \right)^2 \right\}^{0.5} \quad . \tag{7.1}$$

based on Eq.7.1, the percentage overall uncertainty was calculated as

$$\%\delta S_y = 100 \frac{\delta S_y}{S_y} \quad , \tag{7.2}$$

where δS_y, δR_s, δE, δh, and δa are the uncertainties of stress in y-direction, the stress ratio, modulus of elasticity, thickness, and the width of the diaphragm.

The computer code for evaluation of Eqs 7.1 and 7.2 is listed in Appendix C. The percentage of uncertainty for S_y is 7%, for the set of results used in Appendix D. The highest contribution to the overall uncertainty in S_y is due to the uncertainty in the thickness of the diaphragm.

7.1.2. Stress distributions in a diaphragm

Figure 7.3 shows the strain distributions in x-direction and y-direction. Notice, the strain changes sign (from negative to positive) from the center of the diaphragm to the edges. Because of this, some polysilicon strain gauges are placed at the center, and some are placed at the edges. So when the diaphragm deforms under the loading pressure, resistances of the gauges placed at the center change in opposite directions to those of the gauges at the edges. Thus a full Wheatstone bridge can be made out of the isotropic polysilicon material. Figure 7.3 clearly indicates that the vertical strain component

(perpendicular to the edge) is much larger than the transverse (parallel to the edge). From the comparison between these figures, the maximum stress occurs at the center of the longer edges for the rectangular diaphragm. Therefore two of the strain gauges should be placed vertically at the center of the longer edges. In other to determine placement the other strain gauges in the center of the diaphragm, the strains in y-direction and x-direction along the horizontal centerline of the diaphragm should be compared. Since S_y is much greater than S_x, the other strain gauges should be placed on the centerline of diaphragm parallel to the y-direction.

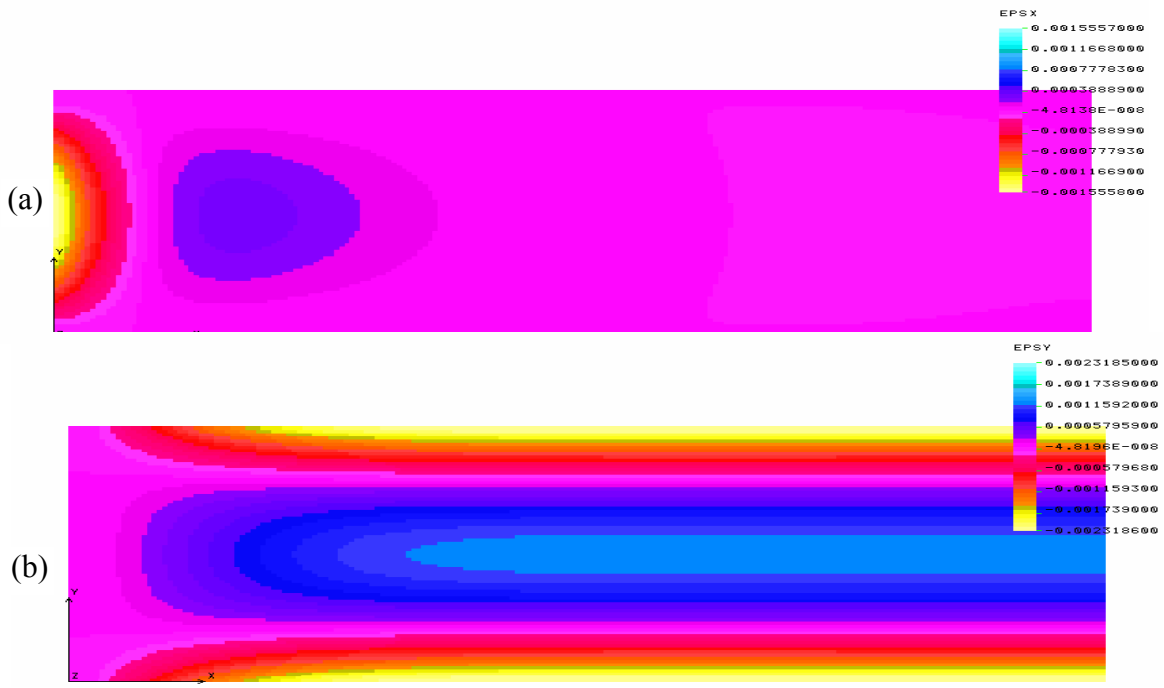

Fig. 7.3. The strain in the rectangular diaphragm, because of symmetry, only half of the diaphragm is shown: (a) x-direction, (b) y-direction.

To finalize location of the strain gauges along the centerline of the diaphragm, we need to know where the stress is uniform. Figures 7.4 to 7.8 show the distribution of S_y

along the centerline of the diaphragm while applying pressure step by step from 0.4 to 2 atm using the model with 20000 elements. As one can observe, stress along the centerline is not uniform, but changes nonlinearly within 15% of the length of the diaphragm at either end of it. Therefore, the strain gauges should be placed in the areas outside of the 15% regions at either end of the diaphragm.

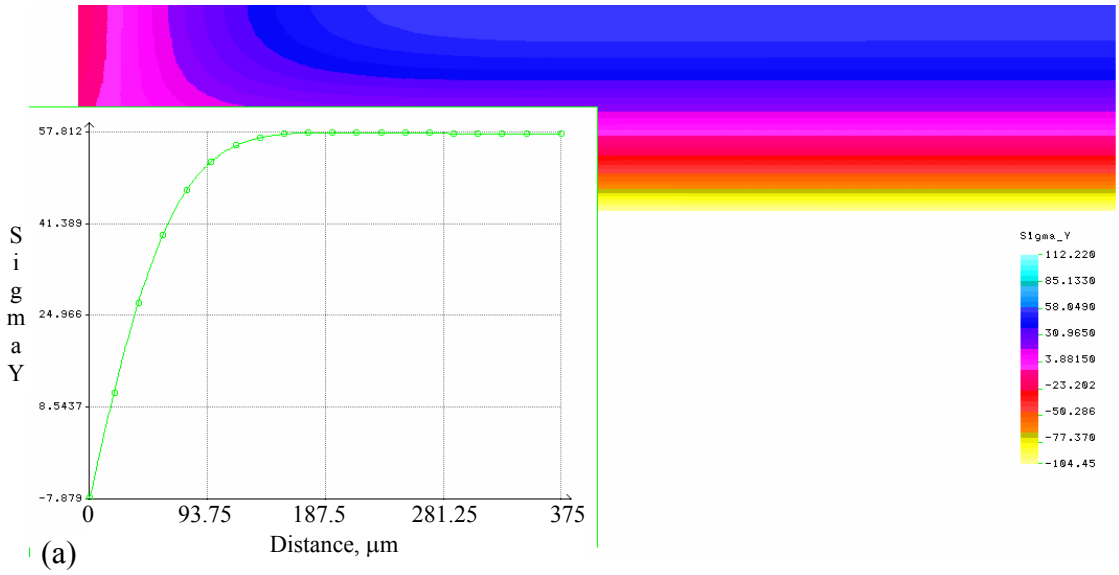

(a)

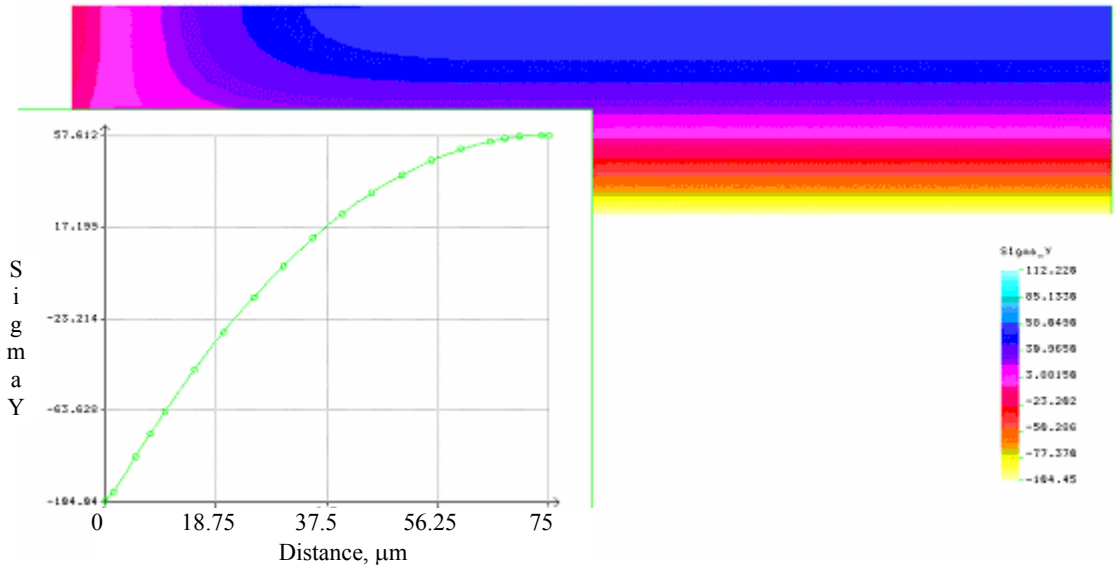

(b)

Fig. 7.4. Stress distribution versus distance along the centerline for step-1 (p = 0.4 atm): (a) at y = 75μm, (b) at x = 375 μm.

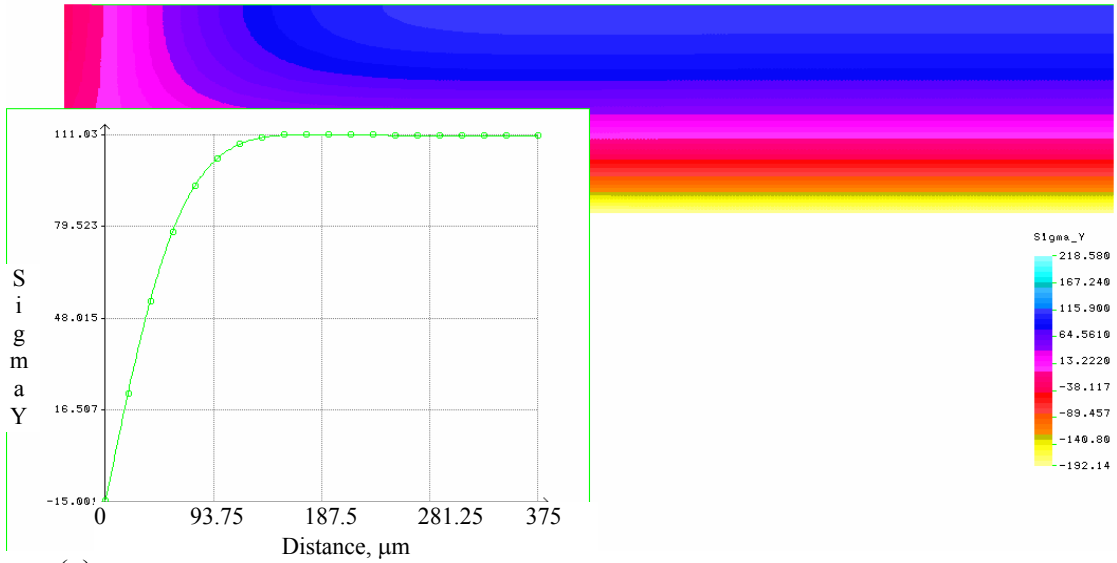

(a)

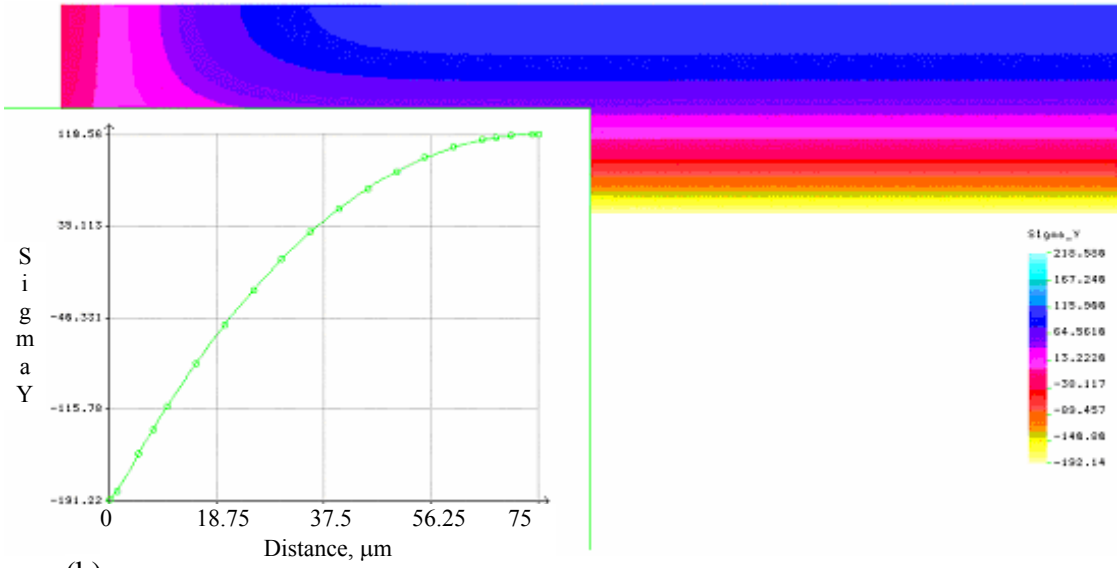

(b)

Fig. 7.5. Stress distribution versus distance along the centerlines for step-2 (p = 0.8 atm): (a) at y = 75 µm, (b) at x = 375 µm.

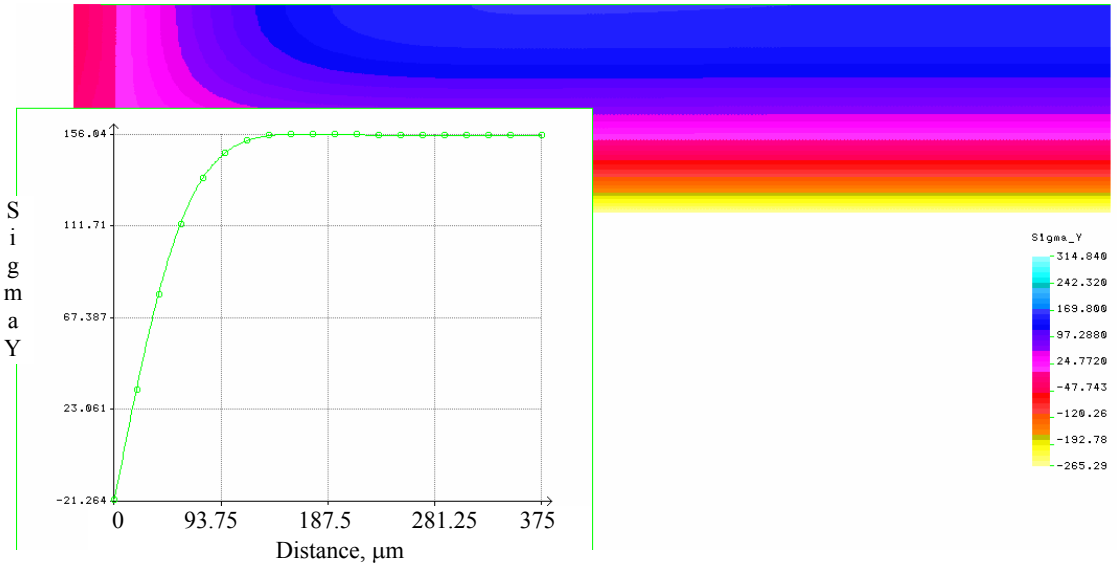

(a)

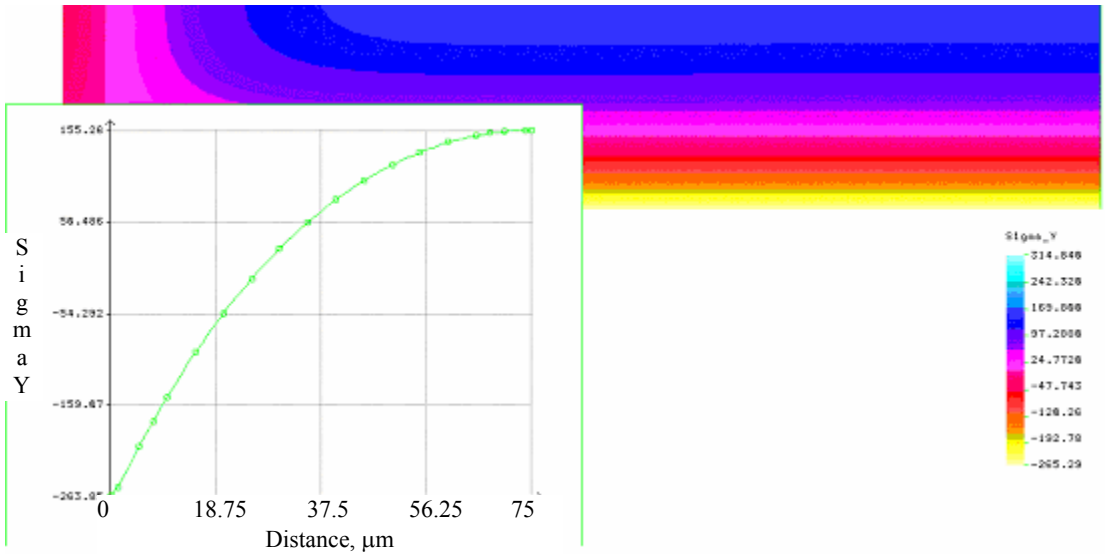

(b)

Fig. 7.6. Stress distribution versus distance along the centerline for step-3 (p = 1.2 atm): (a) at y = 75 µm, (b) at x = 375 µm.

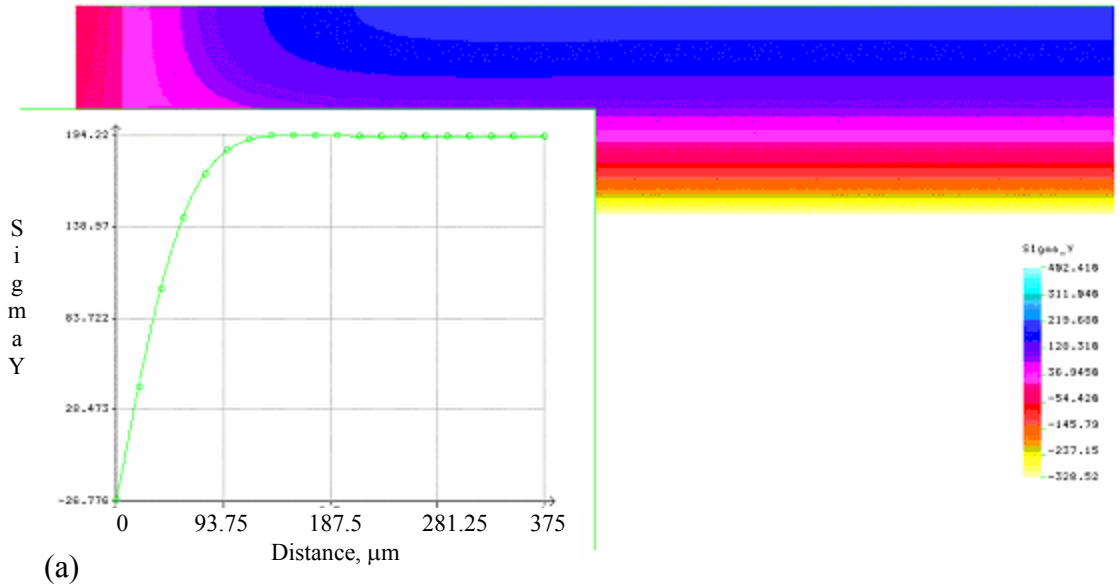

(a)

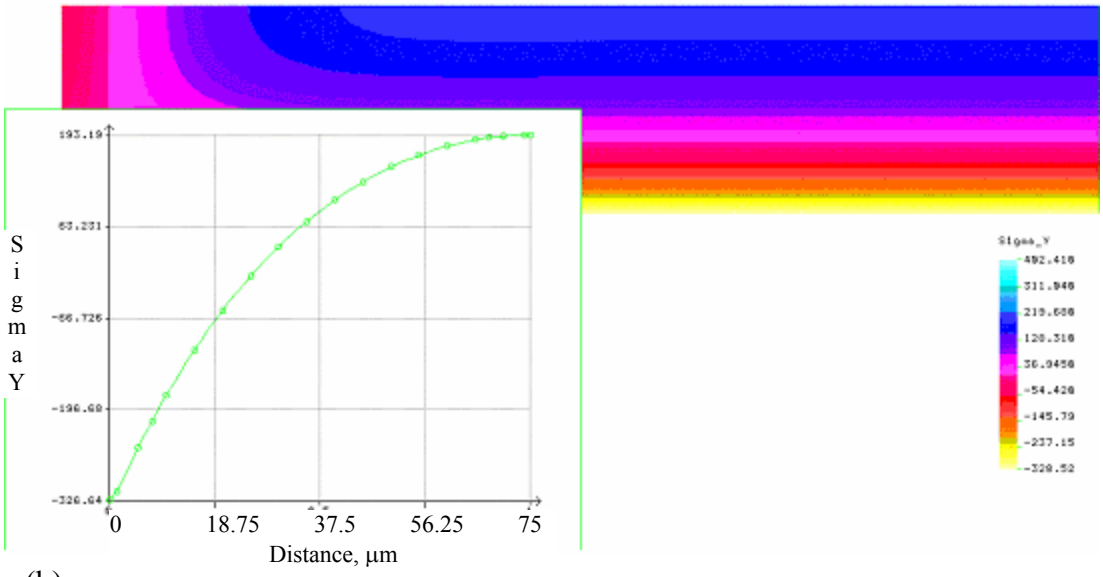

(b)

Fig. 7.7. Stress distribution versus distance along the centerline for step-4 (p = 1.6 atm): (a) at y = 75 μm, (b) at x = 375 μm.

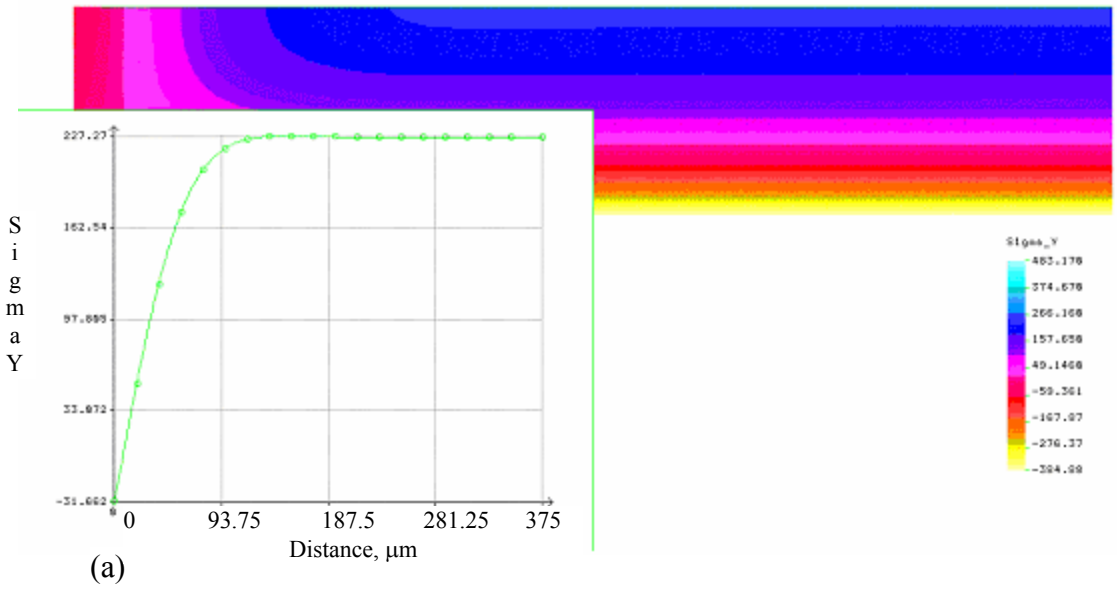

(a)

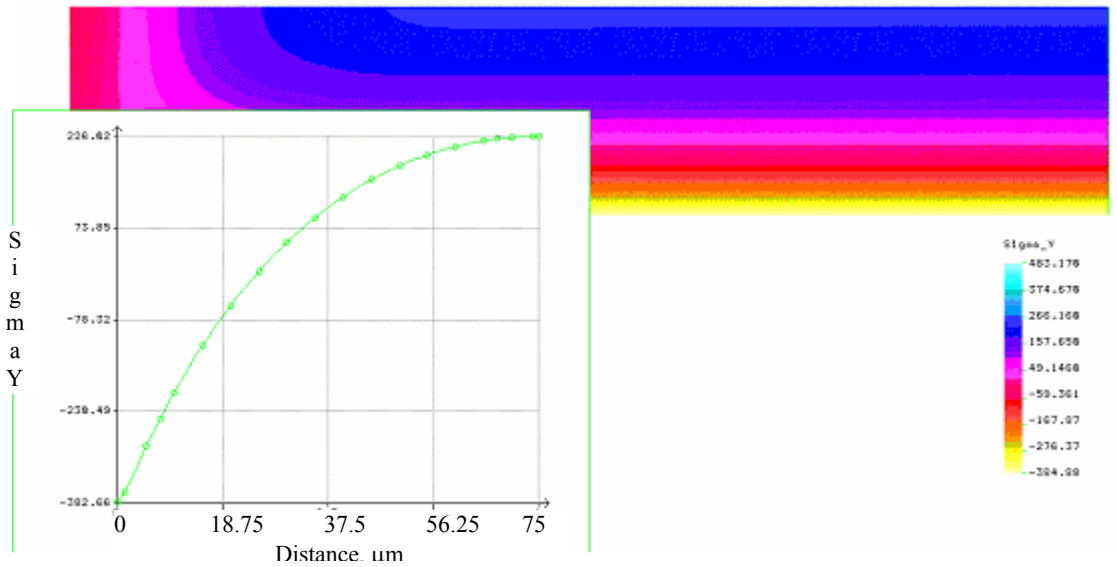

(b)

Fig. 7.8. Stress distribution versus distance along the centerline for step-5 (p = 2 atm): (a) at y = 75 µm, (b) at x = 375 µm.

7.1.3. Gauge sensitivity as a function of characteristic parameters

The average longitudinal and transverse strains for a gauge placed vertically at the center of longer edges and at the center of the diaphragm can be calculated as

$$\bar{\varepsilon}_{l1} = \bar{\varepsilon}_{l4} = \frac{1}{l}\int_0^l \varepsilon_y(x,y)\Big|_{x=0.5a}\, dy \quad , \tag{7.3}$$

$$\bar{\varepsilon}_{t1} = \bar{\varepsilon}_{t4} = \frac{1}{w}\int_{\frac{a}{2}-\frac{w}{2}}^{\frac{a}{2}+\frac{w}{2}} \varepsilon_x(x,y)\Big|_{y=0.5l}\, dx, \tag{7.4}$$

$$\bar{\varepsilon}_{l2} = \bar{\varepsilon}_{l3} = \frac{1}{l}\int_{\frac{b}{2}-\frac{l}{2}}^{\frac{b}{2}+\frac{l}{2}} \varepsilon_y(x,y)\Big|_{x=x_1}\, dy \quad , \tag{7.5}$$

$$\bar{\varepsilon}_{t2} = \bar{\varepsilon}_{t3} = \frac{1}{w}\int_{x_1-\frac{w}{2}}^{x_1+\frac{w}{2}} \varepsilon_x(x,y)\Big|_{y=0.5b}\, dx \quad , \tag{7.6}$$

where $l = \int dy, w = \int dx$, a, b, x_1, $\varepsilon_x(x,y)$, $\varepsilon_y(x,y)$ are the length and width of the polysilicon strain gauge, length and width of the diaphragm, the distance from the short edges of the diaphragm to the middle of strain gauges that are placed along the centerline, Fig. 7.9, and strains in the x-direction and y-direction of the diaphragm, respectively. Figures 7.10 and 7.11 show the average longitudinal and transverse strains for strain gauges, which are placed at the longer edges and along the centerline as a function of the strain gauge length. As it can be observed in these figures, the length of the strain gauge should be as small as possible.

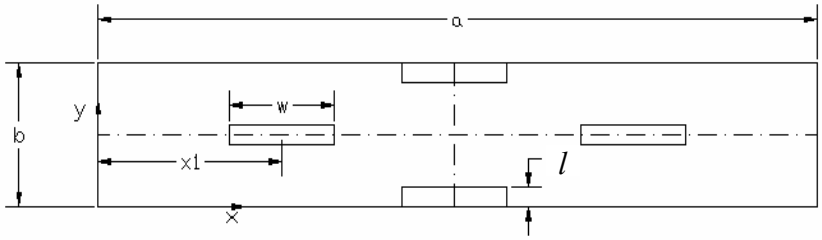

Fig. 7.9. The MEMS pressure sensor diaphragm with strain gauges.

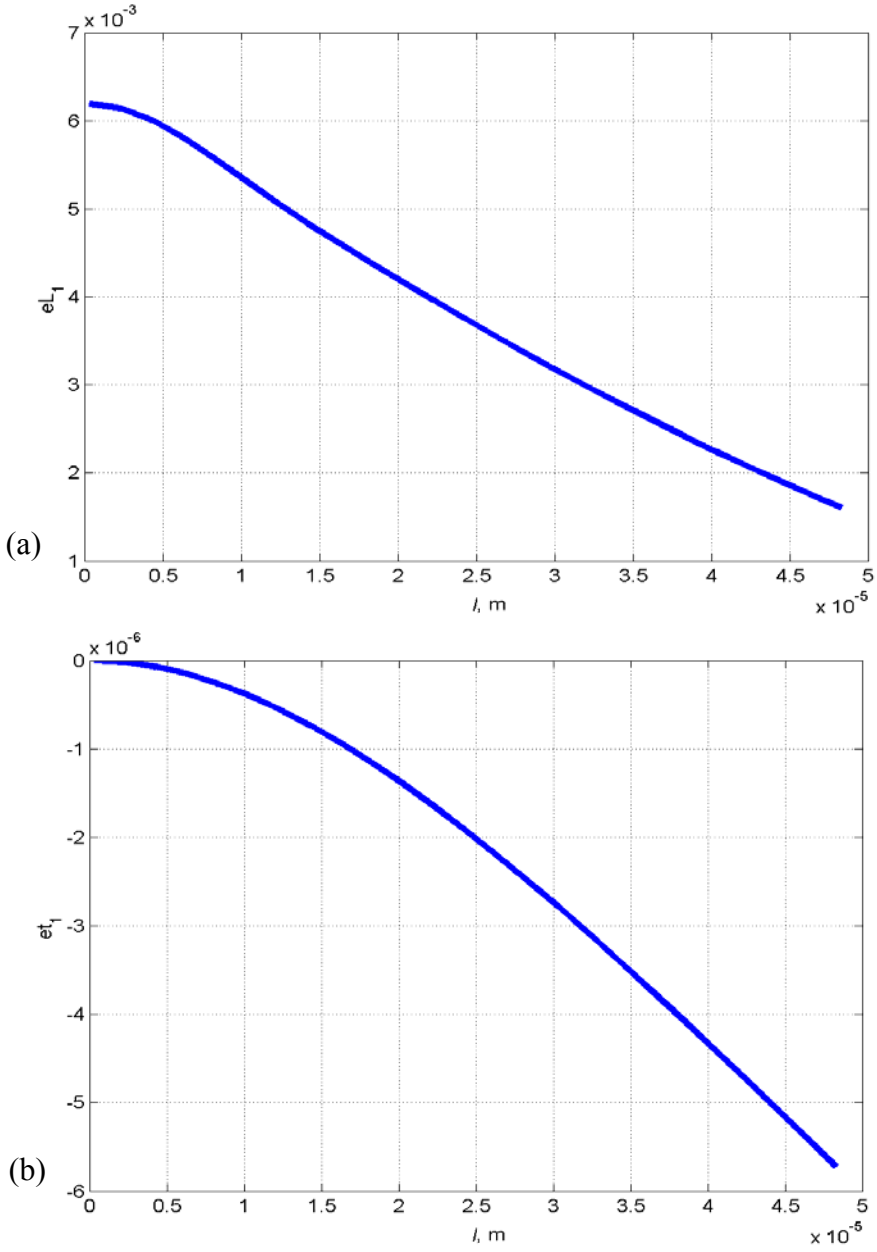

Fig. 7.10. Average longitudinal and transverse strains versus length of the strain gauges at the center of longer edge.

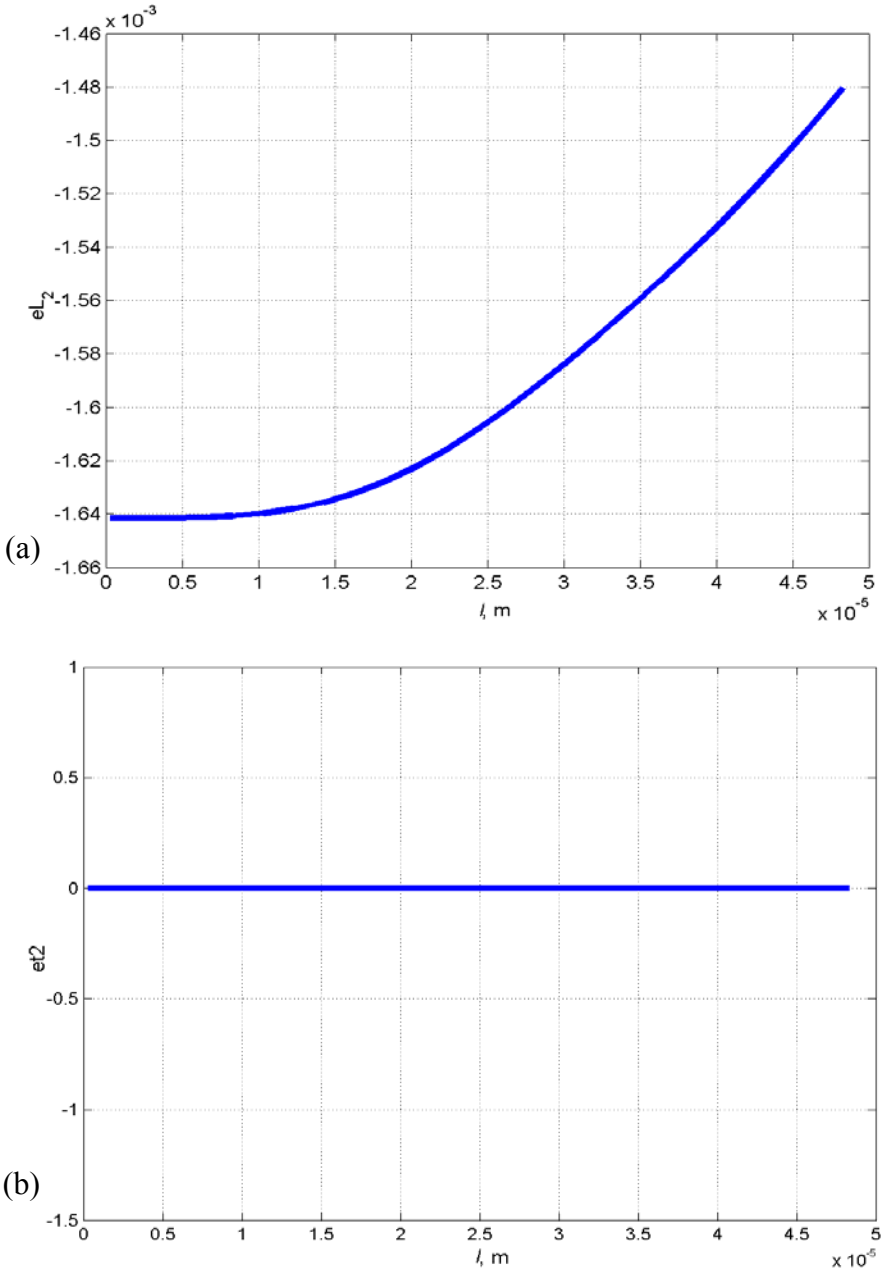

Fig. 7.11. Average longitudinal (a) and transverse (b) strains versus length of the strain gauges along the centerline of the diaphragm.

By substituting Eqs 7.3 to 7.6 into Eq. 4.60, it can be found that

$$S=\frac{\pi t}{P}\left(\sum_{m=1}^{\infty}\sum_{n=1}^{\infty}\left[\left(\frac{na_{mn}}{lb}\right)\left(GF_l+\frac{1}{2\nu}\right)Sa+\left(\frac{2ma_{mn}}{aw}\right)\left(GF_t+\frac{1}{2\nu}\right)Sb\right]\right) \quad , \tag{7.7}$$

where

$$Sa=1-\cos(m\pi))\sin\left(\frac{2n\pi l}{b}\right)-2\left(1-\cos\left(\frac{2m\pi x_1}{a}\right)\right)\cos(n\pi)\sin\left(\frac{n\pi l}{b}\right)$$

and

$$Sb=\left(1-\cos\left(\frac{n\pi l}{b}\right)\right)\sin\left(\frac{m\pi w}{a}\right)\cos(m\pi)-(1-\cos(n\pi))\sin\left(\frac{m\pi w}{a}\right)\cos\left(\frac{2m\pi x_1}{a}\right).$$

Equation 7.7 is a relationship between sensitivity and the dimensions of the strain gauge that can be seen in Figs 7.12 and 7.13. From these figures, it is apparent that the length and width of strain gauge should be as small as possible.

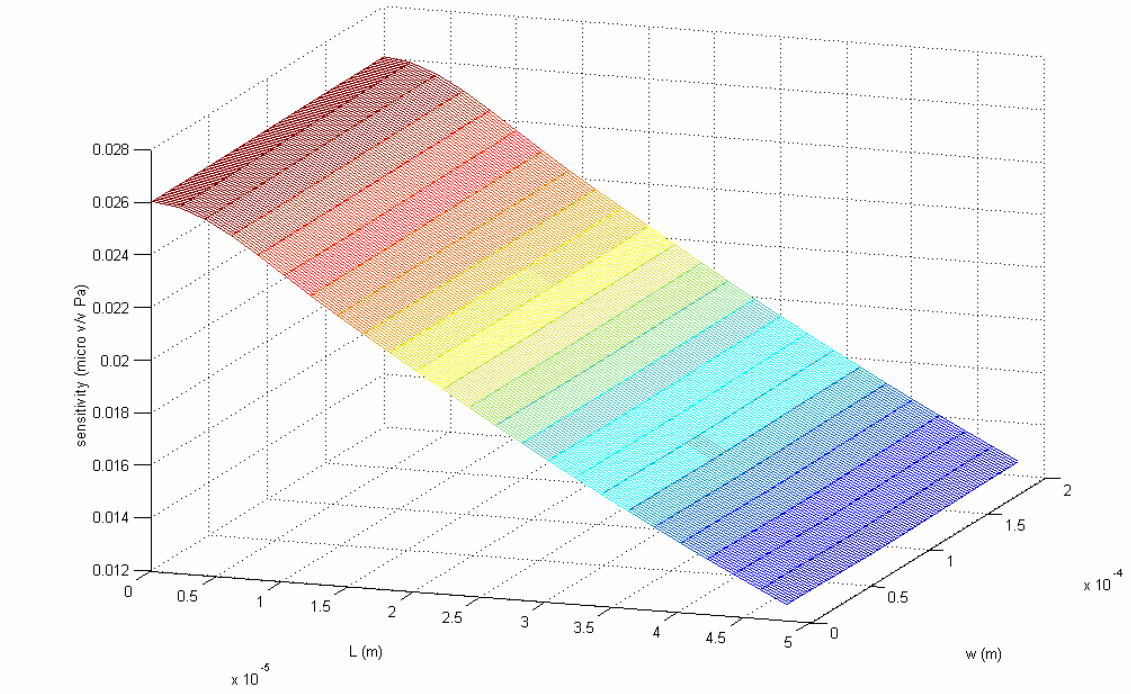

Fig. 7.12. Sensitivity versus length and width of a strain gauge for $GF_l = GF_t = 20$.

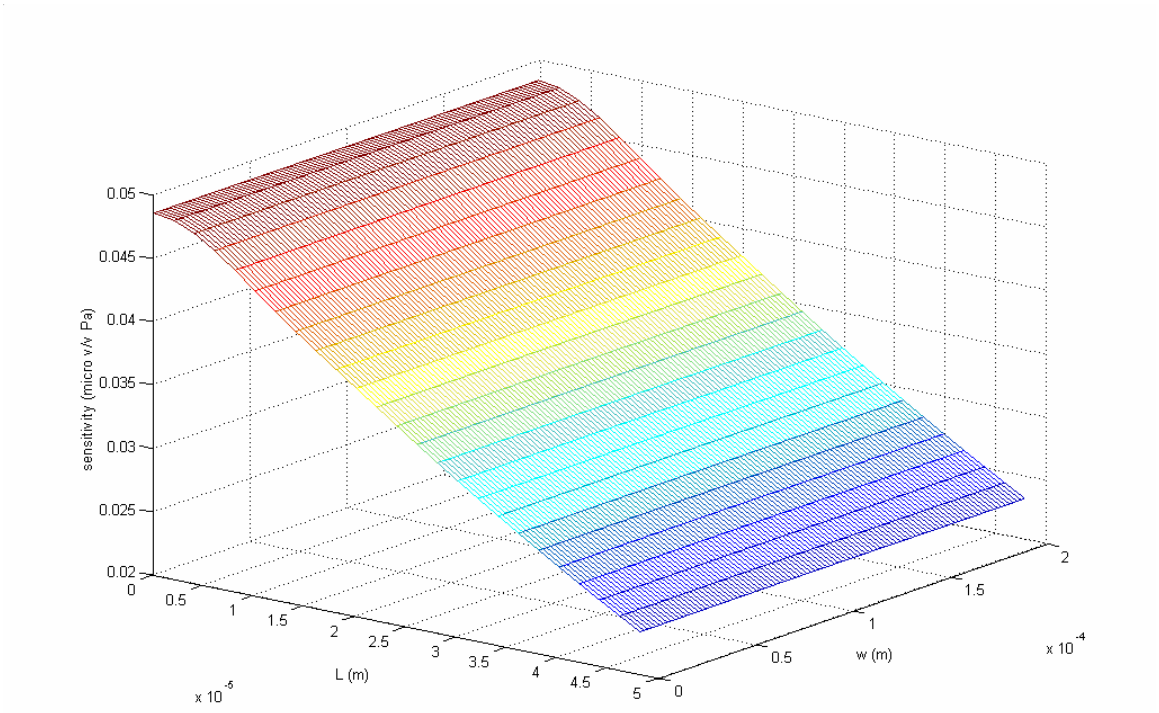

Fig. 7.13. Sensitivity versus length and width of a strain gauge for GF_l= 39, GF_t = -15.

7.1.4. Gauge placement

However, the size of the gauge is limited by several factors:

1) the photolithography capability in the fabrication process,
2) the total resistance of the gauge required for the electrical measurements,
3) a negative effect of reducing gauge size is that the resistance mismatch of the Wheatstone bridge becomes more pronounced.

As can see from Figs 7.12 and 7.13, if the length of the strain gauge is 10% of the width of the diaphragm and the width of strain gauge is 10% of the length of diaphragm, the sensitivity of the pressure sensor is high. Furthermore, the number of terms in Eq. 7.7 influences the accuracy of the sensitivity calculation. The code, listed in Appendix A,

can calculate the sensitivity for different number of terms. In addition, the sensitivity was calculated for two different cases denoted by S_1 and S_2. Table 7.3 and Fig. 7.14 show that the sensitivity converges to a constant value after 10 terms.

Table 7.3. Summary of the results of the sensitivities S_1 and S_2 as functions of the number of terms used in their calculation.

Number of m, n	S_1	S_2
1	0.0204	0.0371
2	0.0207	0.0349
3	0.0249	0.0431
4	0.0209	0.0389
5	0.022	0.0409
6	0.0223	0.0396
7	0.0226	0.0402
8	0.0219	0.0398
9	0.022	0.0401
10	0.0222	0.0399
12	0.0221	0.0399
15	0.0222	0.04
20	0.0222	0.0399
25	0.0222	0.04

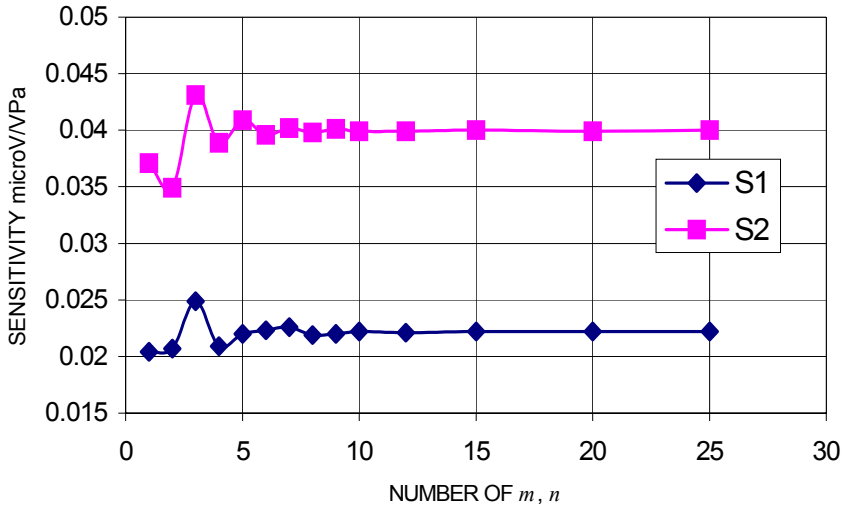

Fig. 7.14. The sensitivity versus number of terms in the series.

7.1.5. Deformation fields of the diaphragm

Figure 7.15 shows deformations of the diaphragm in *z*-direction (parallel to the direction of the applied pressure) under a uniform pressure load of 2 atm.

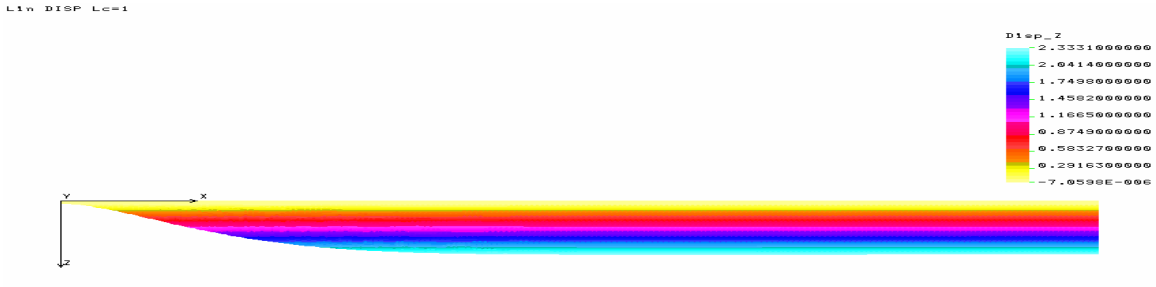

Fig. 7.15. Deformation of the diaphragm in *z*-direction.

7.1.6. OELIM measured deformations of the diaphragm

A representative diaphragm including piezoresistive strain gauges forming a Wheatston bridge, of a MEMS pressure sensor of the type studied in this thesis, is shown in Fig. 7.16. Using OELIM methodology, deformations of the MEMS pressure sensor diaphragm were measured as a function of pressure load (Pryputniweicz, et al., 2001). Figure 7.17 shows representative OELIM fringe pattern corresponding to a gauge pressure of 0 atm. The deformation field, corresponding to the fringe pattern of Fig. 7.17, is shown in Figs 7.18 and 7.19. In particular, Fig. 7.18 clearly depicts the effects that strain gauges have on the deformation of the diaphragm. The maximum deformation is shown to be 0.27 μm. Since, there is no external load at $p_g = 0$, the deformations should be zero. Therefore, the measured deformation does not correlate with analytical and computational. This deformation in the experimental solution comes from residual stresses due to fabrication process.

The same procedure was repeated for each 0.2 atm increment gauge pressure. OELIM fringe pattern is shown in Fig. 7.20 and Fig. 7.21 for the gauge pressures equal to 1 and 2 atm, respectively. 2D contour representations of deformations based on the fringe patterns of Figs 7.20 and 7.21 are shown in Figs 7.22, 7.23, respectively. The 3D representatives of the deformations corresponding to the figure patterns shown in Figs and are displayed in Figs 7.24 and 7.25 , respectively. It can be seen, the maximum deformation is shown to be 1.11 μm at p_g = 1 atm and 1.65 at p_g = 2atm. This measured deformation compares well with the FEM determined deformation.

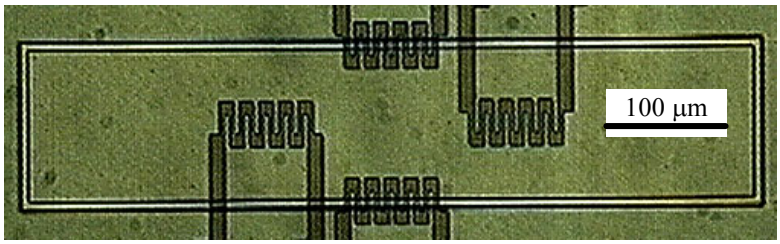

Fig. 7.16. Diaphragm of the MEMS pressure sensor.

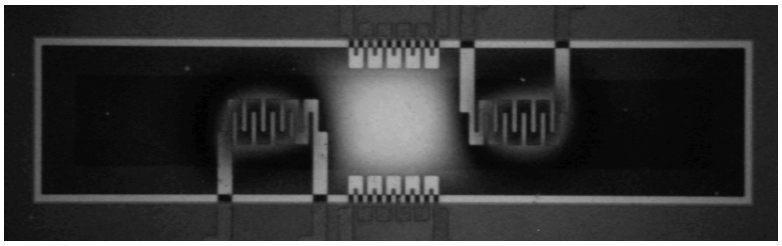
Fig. 7.17. OELIM fringe pattern of the diaphragm shown in Fig. 7.16. when subjected to p_g = 0 atm.

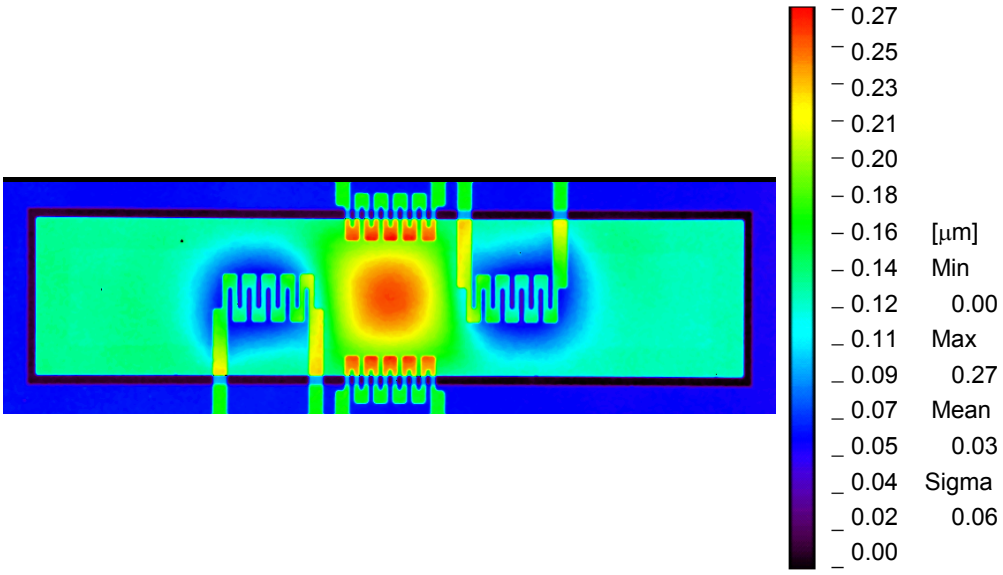

Fig. 7.20. 2D contour representation of deformations based on the fringe pattern shown in Fig. 7.17.

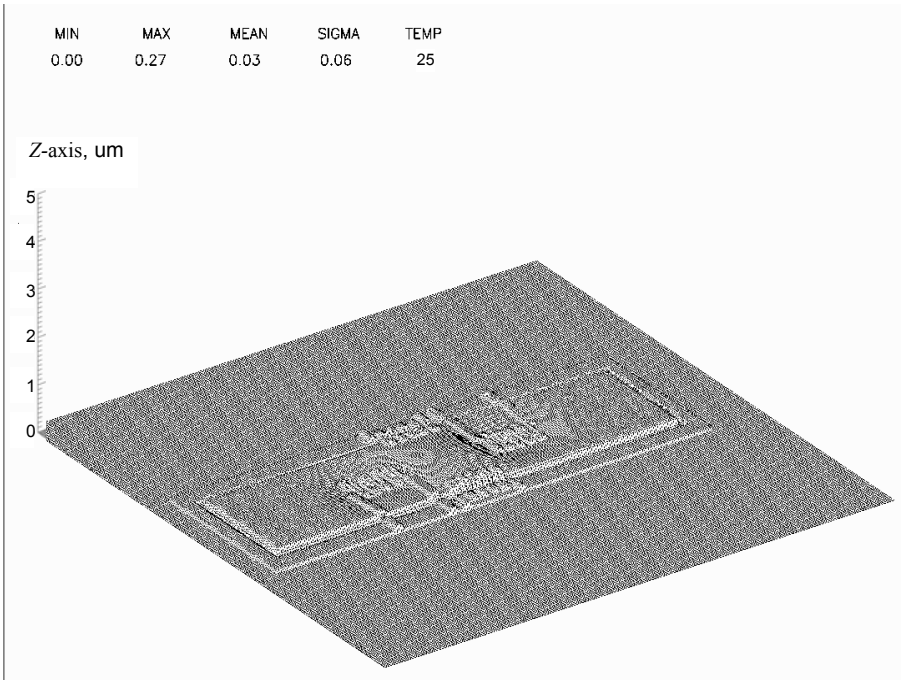

Fig. 7.21. 3D wireframe representation of deformations based on the fringe pattern shown in Fig. 7.17.

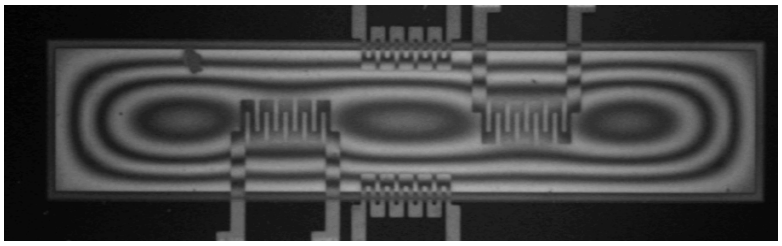

Fig. 7.22. OELIM fringe pattern of the diaphragm shown in Fig. 7.16. when subjected to p_g = 1 atm.

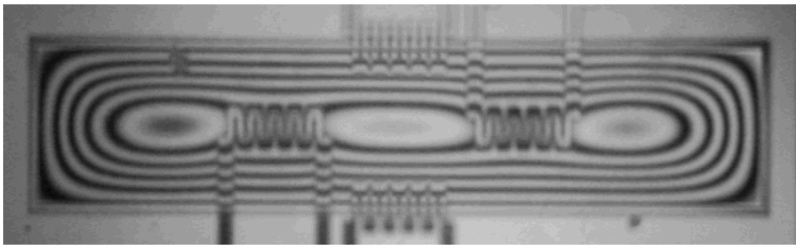

Fig. 7.23. OEHM fringe pattern of the diaphragm shown in Fig. 7.16. when subjected to a pressure of 2 atm.

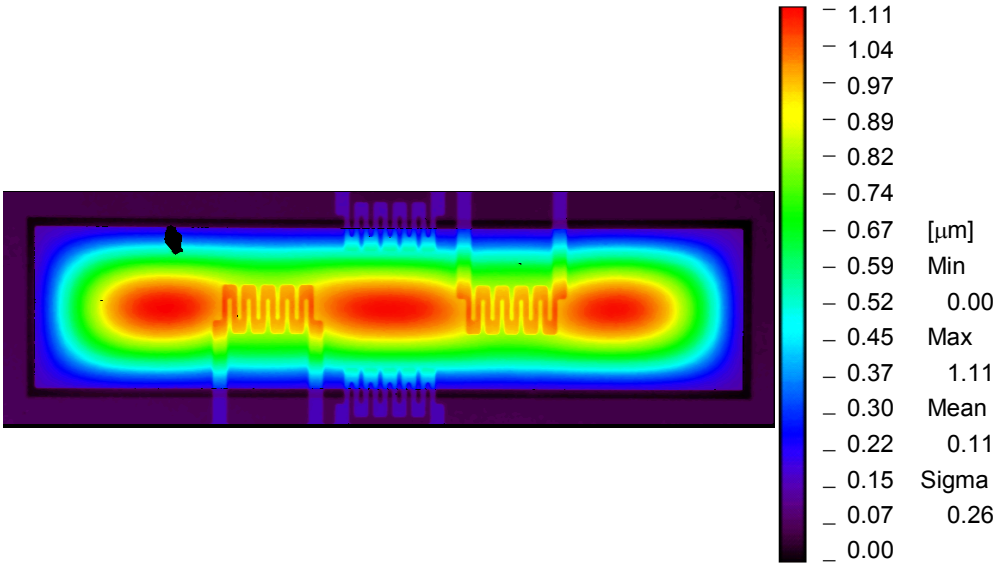

Fig. 7.24. 3D wireframe representation of deformations based on the fringe pattern shown in Fig. 7.22.

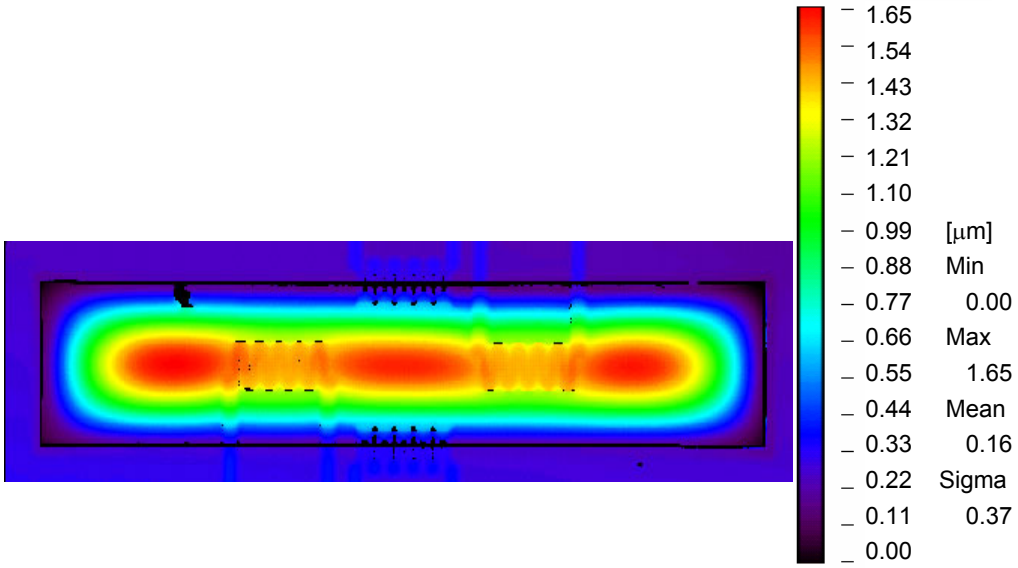

Fig. 7.25. 2D contour representation of deformations based on the fringe pattern shown in Fig. 7.23.

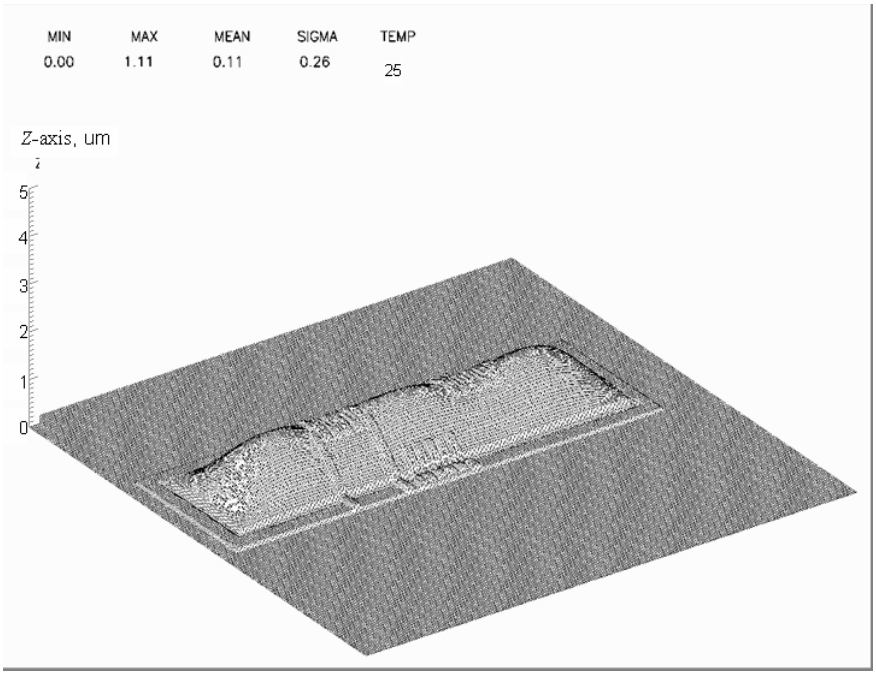

Fig. 7.26. 3D wireframe representation of deformations based on the fringe pattern shown in Fig. 7.22.

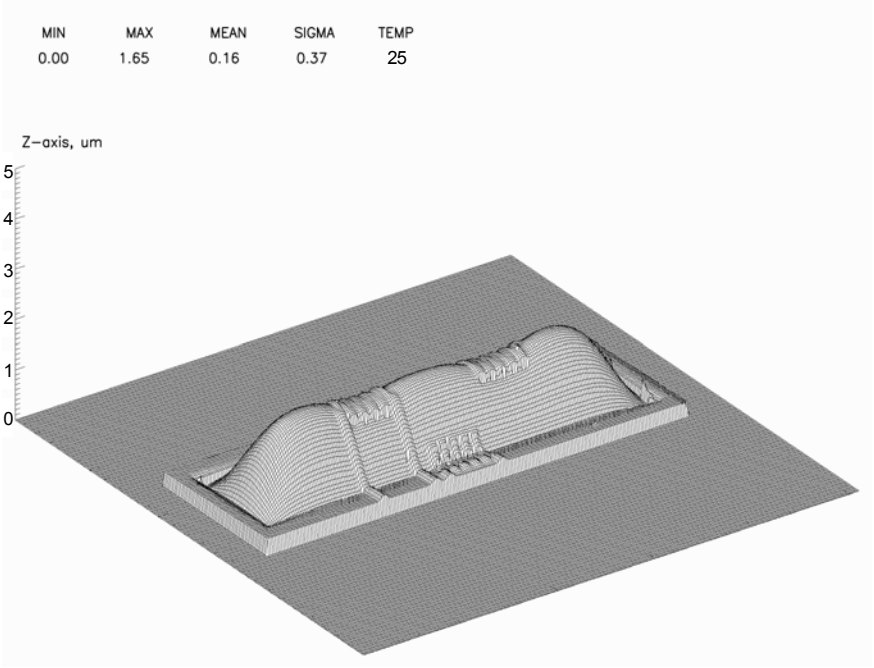

Fig. 7.27. 3D wireframe representation of deformations based on the fringe pattern shown in Fig. 7.23.

7.1.7. Geometry and dimensions of the MEMS pressure sensor

Based on the results presented in section 7.1.1 to 7.1.5, the diaphragm of the MEMS pressure sensor should be 2 μm thick, 150 μm wide, and 750 μm long. Also, to assume highest sensitivity of the piezoresistive strain gauges they should be 75 μm long and 15 μm wide and placed as shown in Fig. 7.9.

7.2. Relative humidity sensors

7.2.1. Convergence of capacitance as a function of time

Figure 7.28 shows the normalized moisture concentration versus number of elements. This figure illustrates that the concentration inside the plate converges to a final value when using greater than 500 elements are used in the model.

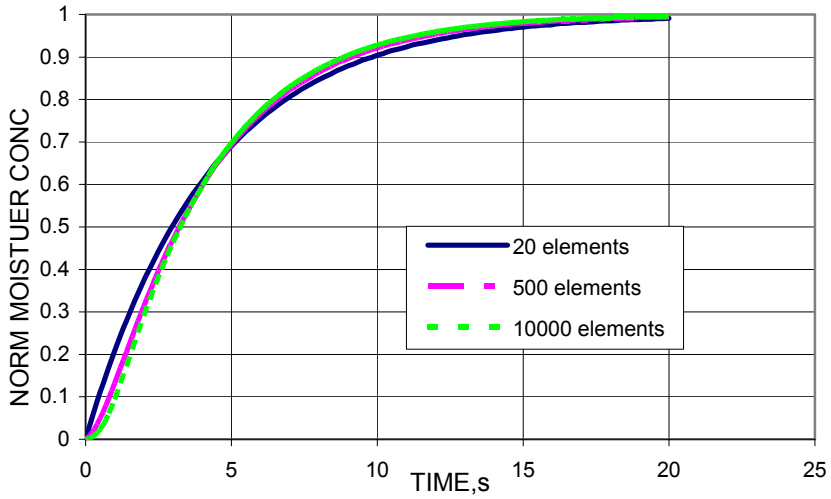

Fig. 7.28. Normalized moisture concentration versus time for a different number of elements used in modeling of the sensitive layer at x = 5 μm, y = 500 μm and h = 1μm.

Figure 7.29 shows the normalized moisture concentration along the centerline distance for each finger. Figure 7.30 shows the normalized concentration of moisture at the lowest concentration point inside each finger as a function of time, when the diffusion constant is 3×10^{-8} cm^2/sec. From this figure, the time the lowest concentration point takes to reach the steady state can be determined. The lowest concentration point is at the center of the modeled region for the four-sided diffusion. It is observed that the time

constant ($t_{60\%}$) is 4 sec. In Fig. 7.31, the sensitive layer in conjunction with a stripped upper electrode was modeled. It is observed that the sensor will have a much shorter response time as a result of diffusion from the top electrode.

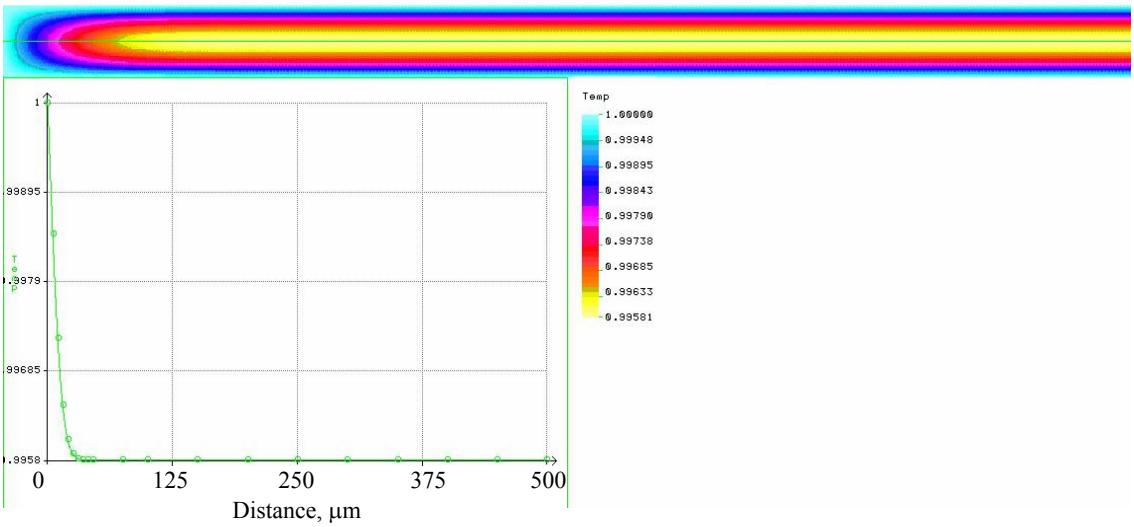

Fig. 7.29. Normalized moisture concentration versus distance in the length direction.

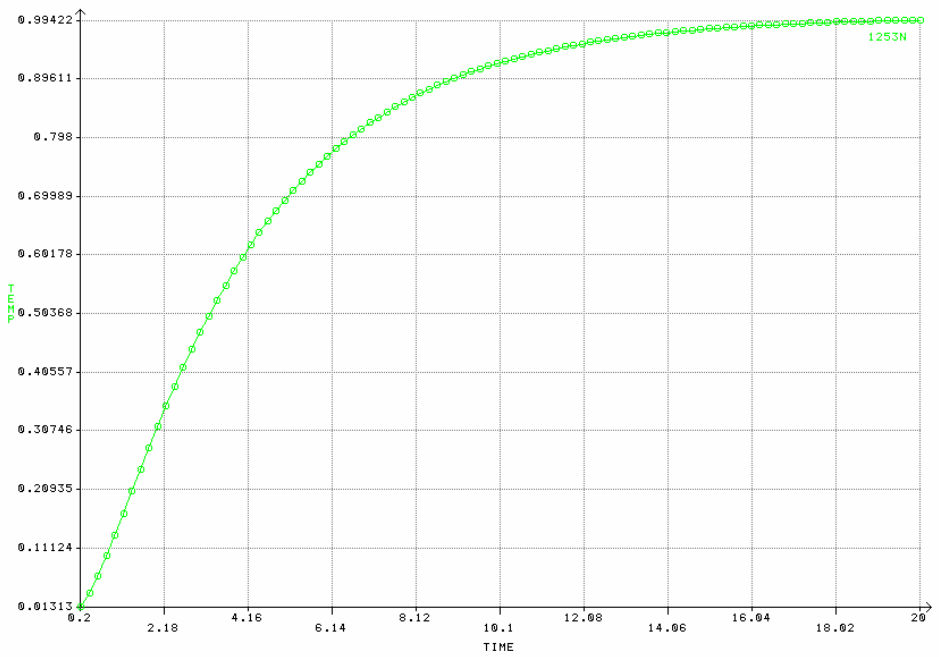

Fig. 7.30. Computational solution for concentration versus response time in each finger (2D model) at the center of each finger.

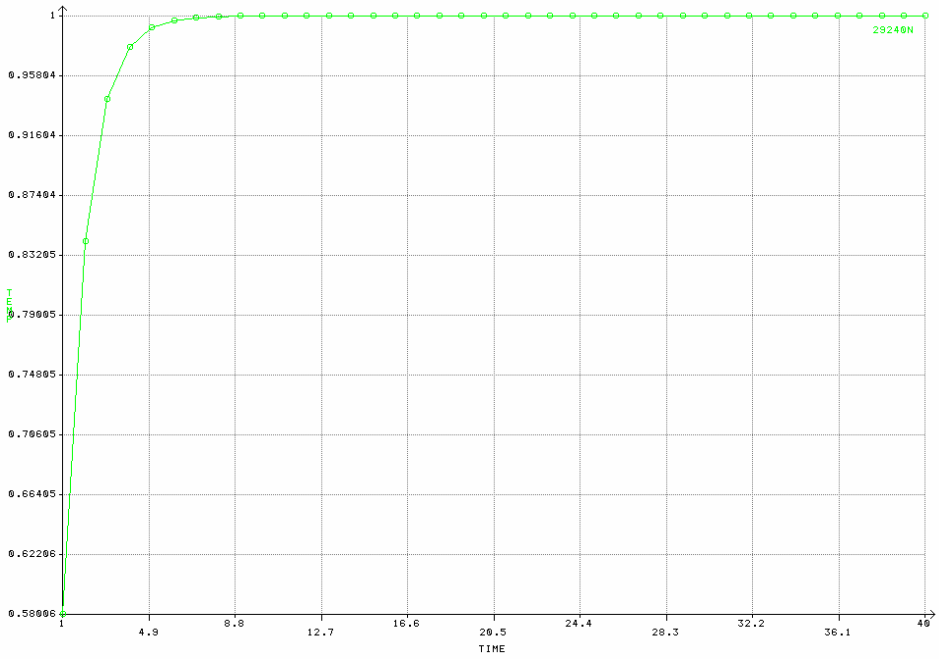

Fig. 7.31. Computational solution for moisture concentration versus response time in the whole sensitive layer with using striped electrode at top.

7.2.2. Sensitivity as a function of characteristic parameters

In Eq. 4.82, C_{nor} is an exponential function of time, and it depends on the length and width of the sensitive layer. To optimize design of the humidity sensor, a compromise is needed between short response time and high sensitivity. For a first step, a square with area of 1 mm^2 is assumed for the sensitive layer. Figure 7.32 shows the relationship between the C_{nor} and the response time. It can be observed that the sensitivity is 0.0531pF/%RH, but the response time is too long (i.e., the time constant ($t_{63\%}$) is 3 hrs and 3 mins). Therefore, changes are needed in the dimensions.

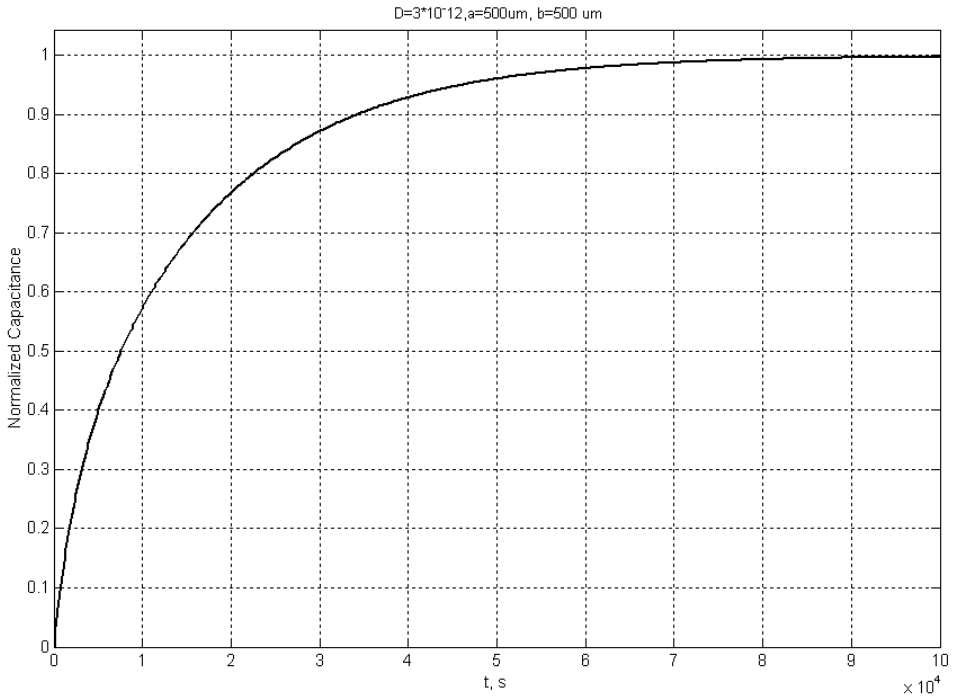

Fig. 7.32. The normalized capacitance versus time with using $L = b = 1000$ μm as a sensitive layer.

For the second step, the top electrode is assumed to consist of strips instead of a single rectangular surface. These strips should be formed in such a way that they form

parallel capacitances. Therefore, the capacitance of the whole structure can be calculated as

$$C = \varepsilon_0 \varepsilon_r \frac{2a(nb_1)}{d} \quad , \tag{7.8}$$

where $2a$, b_1, d, and n are the length of the strips, the strip width, the thickness of the sensitive layer, and the number of the strips, respectively. Thus the sensitivity of this sensor can be calculated to be

$$S = \frac{\Delta C}{\Delta Rh} = \frac{C_{100\%} - C_{0\%}}{100} \quad , \tag{7.9}$$

where $C_{100\%}$ and $C_{0\%}$ are capacitances when the relative humidity is equal to 100% and 0%, respectively. The changes in relative humidity affect ε_r.

Since the thickness of the sensitive layer does not influence in the response time (because there is no diffusion from the top to the bottom layers) and a smaller thickness increases sensitivity according to the Table 7.5 and Fig. 7.33, the thickness should be as small as possible.

Table 7.5. The relationship between the thickness of the sensitive layer and sensitivity.

a (μm)	b_1 (μm)	b_s (μm)	d (μm)	ε_0 (pNm^2/C^2)	$\varepsilon_{r0\%}$	$\varepsilon_{r100\%}$	n	C_0 (pF)	C_f (pF)	S (pF/%RH)	$t_{90\%}$ (s)	$t_{60\%}$ (s)
1000	10	10	10.00	8.85	2.8	4	50	1.24	1.77	0.0177	7.3	2.6
1000	10	10	5.00	8.85	2.8	4	50	2.48	3.54	0.0354	7.3	2.6
1000	10	10	2.50	8.85	2.8	4	50	4.96	7.08	0.0708	7.3	2.6
1000	10	10	2.00	8.85	2.8	4	50	6.20	8.85	0.0885	7.3	2.6
1000	10	10	1.50	8.85	2.8	4	50	8.26	11.80	0.1180	7.3	2.6
1000	10	10	1.00	8.85	2.8	4	50	12.39	17.70	0.1770	7.3	2.6
1000	10	10	0.75	8.85	2.8	4	50	16.52	23.60	0.2360	7.3	2.6
1000	10	10	0.50	8.85	2.8	4	50	24.78	35.40	0.3540	7.3	2.6
1000	10	10	0.25	8.85	2.8	4	50	49.56	70.80	0.7080	7.3	2.6

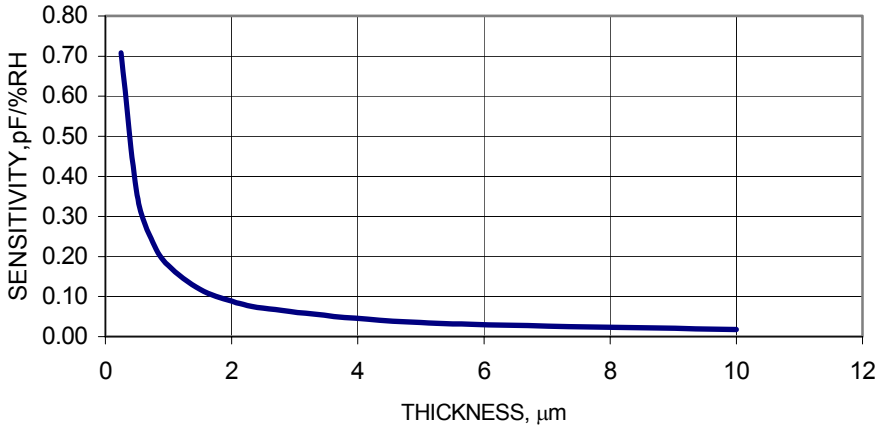

Fig. 7.33. Sensitivity versus different thickness of sensitive layer for L = 1000 μm and b = 10μm.

The thickness depends on the material and the fabrication process. Since one wants to use photosensitive polyimide (Amoco, 1992), the thickness of this material can be as small as 2 μm, using spin coating for the fabrication process.

The forgoing analyses demonstrate that increasing the length, and width, the sensitivity increases and so does the response time increases, too. Since, the objective of this thesis is to design a microsensor for humidity measurements, which will be subsequently integrated with other sensors, there are limitations in the length and width dimensions. Table 7.6 and Fig. 7.34 show the effects of different lengths on the sensitivity and the response time, while keeping the width and thickness constant. Because of the limitation in the allowable space, the length cannot be greater than 1000 μm.

Table 7.6. The relationship between the length of sensitive layer and sensitivity.

a (μm)	b_1 (μm)	b_s (μm)	d (μm)	ε_0 (pNm^2/C^2)	$\varepsilon_{r0\%}$	$\varepsilon_{r100\%}$	n	C_0 (pF)	C_f (pF)	S (pF/%RH)	$t_{90\%}$ (s)	$t_{60\%}$ (s)
3000	10	10	2	8.85	2.8	4	150	55.76	79.65	0.2390	7.3	2.6
2500	10	10	2	8.85	2.8	4	125	38.72	55.31	0.1659	7.3	2.6
2000	10	10	2	8.85	2.8	4	100	24.78	35.40	0.1062	7.3	2.6
1500	10	10	2	8.85	2.8	4	75	13.94	19.91	0.0597	7.3	2.6
1000	10	10	2	8.85	2.8	4	50	6.20	8.85	0.0266	7.3	2.6
750	10	10	2	8.85	2.8	4	38	3.48	4.98	0.0149	7.3	2.6
500	10	10	2	8.85	2.8	4	25	1.55	2.21	0.0066	7.3	2.6
250	10	10	2	8.85	2.8	4	12	0.39	0.55	0.0017	7.3	2.6
100	10	10	2	8.85	2.8	4	5	0.06	0.09	0.0003	7.3	2.6
50	10	10	2	8.85	2.8	4	2.5	0.02	0.02	0.0001	7.3	2.6

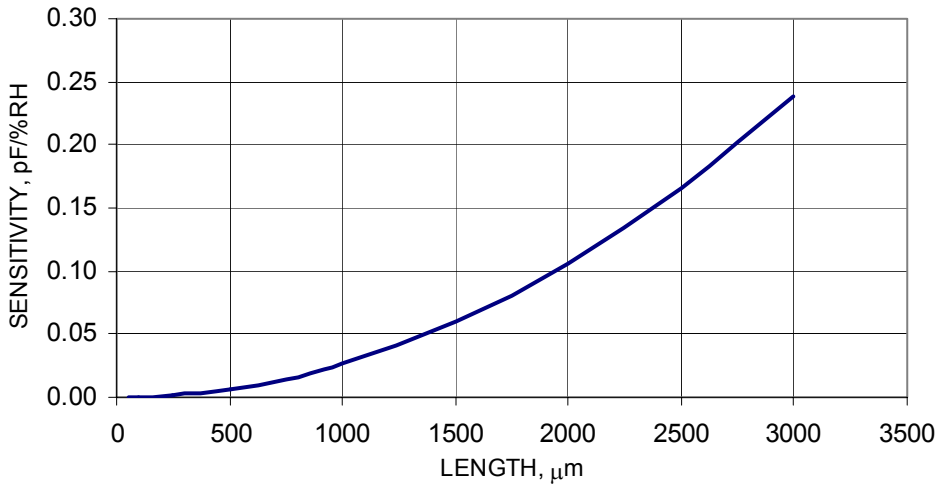

Fig. 7.34. Sensitivity versus different lengths of sensitive layer for t = 2 μm and b = 10μm.

Table 7.7 and Fig. 7.35 show the relationship between the width of strips and sensitivity and response time. It can be observed, since the width of strips and the space between them are the same, that the sensitivity is constant result of getting the balance between the widths of the strips and the number of parallel capacitances. Thus, choosing the smaller strip width results in faster sensors.

Table 7.7. The relationship between the strip width of strips and sensitivity.

a (μm)	b_1 (μm)	b_s (μm)	d (μm)	ε_0 (pNm^2/C^2)	$\varepsilon_{r0\%}$	$\varepsilon_{r100\%}$	n	C_0 (pF)	C_f (pF)	S (pF/%RH)	$t_{90\%}$ (s)	$t_{60\%}$ (s)
1000	100	100	2	8.85	2.8	4	5	6.20	8.85	0.0266	713.0	255.6
1000	75	75	2	8.85	2.8	4	7	6.20	8.85	0.0266	405.7	145.3
1000	50	50	2	8.85	2.8	4	10	6.20	8.85	0.0266	181.4	65.0
1000	25	25	2	8.85	2.8	4	20	6.20	8.85	0.0266	45.5	16.4
1000	15	15	2	8.85	2.8	4	33	6.20	8.85	0.0266	16.4	5.9
1000	10	10	2	8.85	2.8	4	50	6.20	8.85	0.0266	7.3	2.6
1000	5	5	2	8.85	2.8	4	100	6.20	8.85	0.0266	1.8	0.7

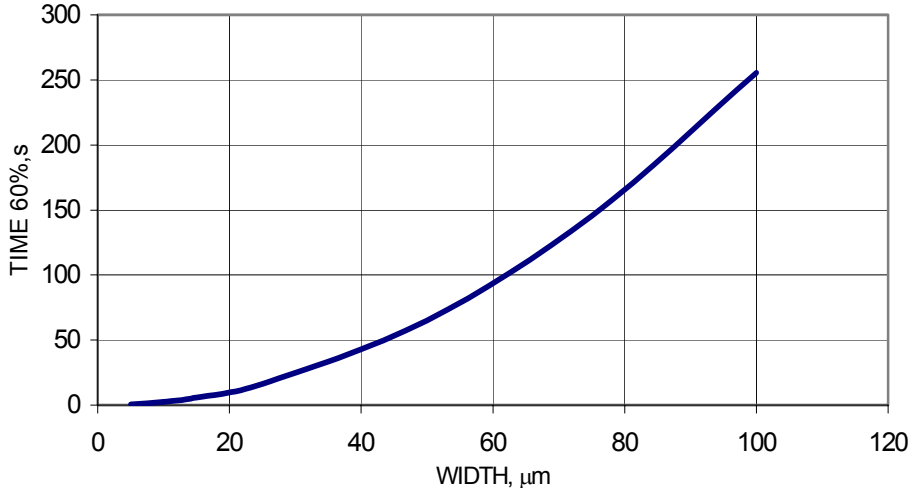

Fig. 7.35. Sensitivity versus strip width for t = 2 μm and L = 1000μm.

The next step is exploring the effect of changing the space between the strips. These changes have effects on the sensitivity. Table 7.8 illustrates that by decreasing the space between the strips the sensitivity increases.

Table 7.8. The relationship between the size of spaces between strips and sensitivity.

a (μm)	b_1 (μm)	b_s (μm)	d (μm)	ε_0 (pNm^2/C^2)	$\varepsilon_{r0\%}$	$\varepsilon_{r100\%}$	n	C_0 (pF)	C_f (pF)	S (pF/%RH)	$t_{90\%}$ (s)	$t_{60\%}$ (s)
1000	10	2.5	2	8.85	2.8	4	80	9.91	14.16	0.0425	7.3	2.6
1000	10	5	2	8.85	2.8	4	66	8.26	11.80	0.0354	7.3	2.6
1000	15	5	2	8.85	2.8	4	50	9.29	13.28	0.0398	16.4	5.9
1000	15	8	2	8.85	2.8	4	43	8.08	11.54	0.0346	16.4	5.9
1000	15	10	2	8.85	2.8	4	40	7.43	10.62	0.0319	16.4	5.9

7.2.3. Moisture diffusion as a function of time

Figure 7.36 shows the normalized capacitance versus time calculated using Eq. 4.81. Finally, with selecting the width of strips equal to 10 μm, the sensitivity and the time constant are equal to 0.0266 pF/%RH and 2.6 sec, respectively.

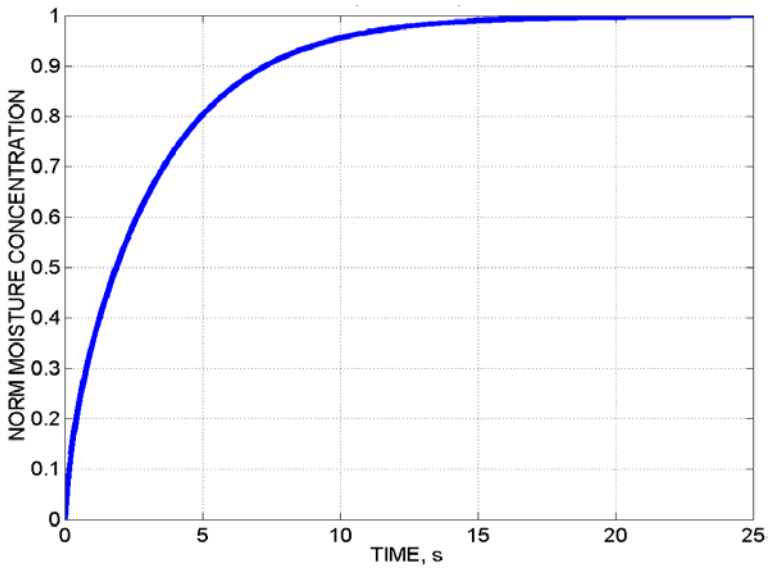

Fig. 7.36. Normalized capacitance versus time for L = 1000 μm, b = 10 μm, and t = 2 μm.

7.2.4. Geometry and dimensions of the MEMS relative humidity sensor

In this study, the width of strips and spaces between them are considered to be the same and equal to 10 μm. The cross section area of this sensor is shown in Fig 7.37.

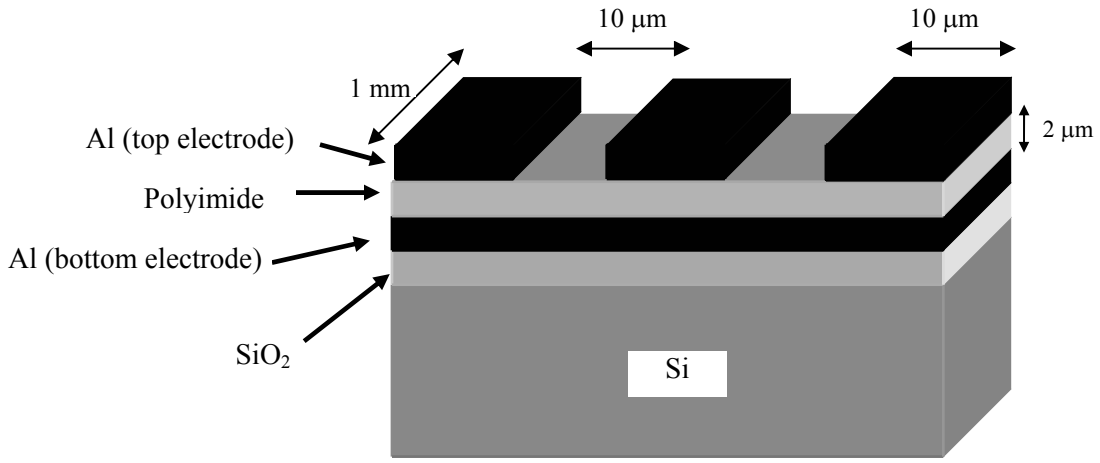

Fig. 7.37. Cross-section area of the capacitive humidity sensor.

7.3. Temperature sensor

7.3.1. Resistivity as a function of characteristic parameters

Using equations presented in section 4.3 resistivity and doping concentrations in the materials for temperature sensors were calculated by the code listed in Appendix C. Representative results obtained during these calculations are displayed in Figs 7.38 and 7.39 for small grain size and large grain size, respectively.

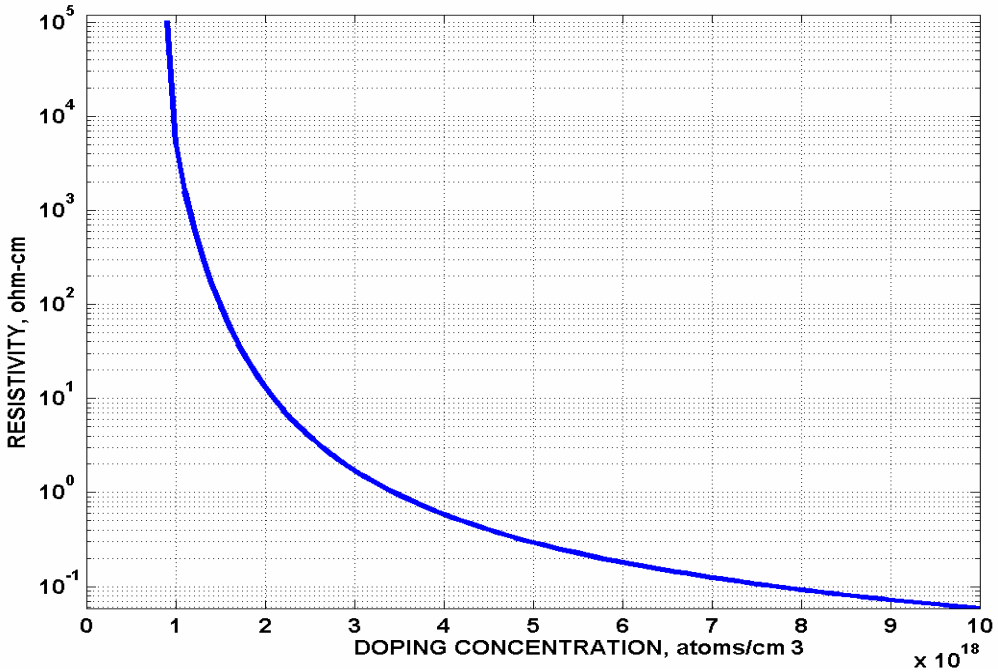

Fig. 7.38. Resistivity versus doping concentration with grain size of 200Å.

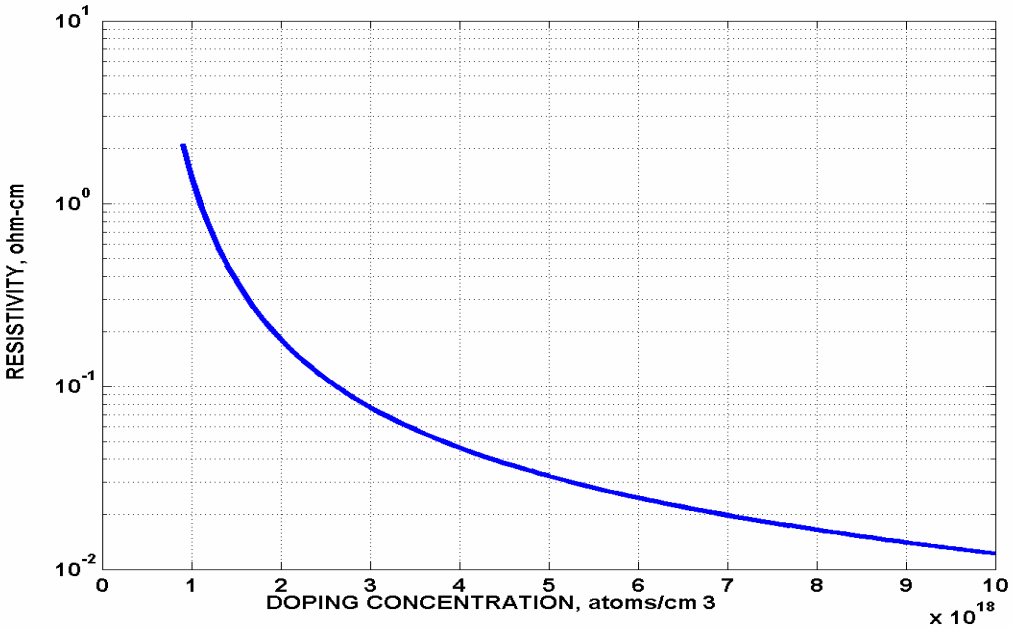

Fig. 7.39. Resistivity versus doping concentration with grain size of 1000 Å.

7.3.2. Temperature coefficient of resistance as a function of concentration

Using Eqs 4.128 and 4.129, TCR_{dc} and TCR_{ac} were calculated, for specific doping concentration, by substituting Eq. 4.126 and $R = V_a/I$ into Eq. 4.124. Representative results showing TCR_{dc} versus doping concentration for different grain size are displayed in Fig. 7.40.

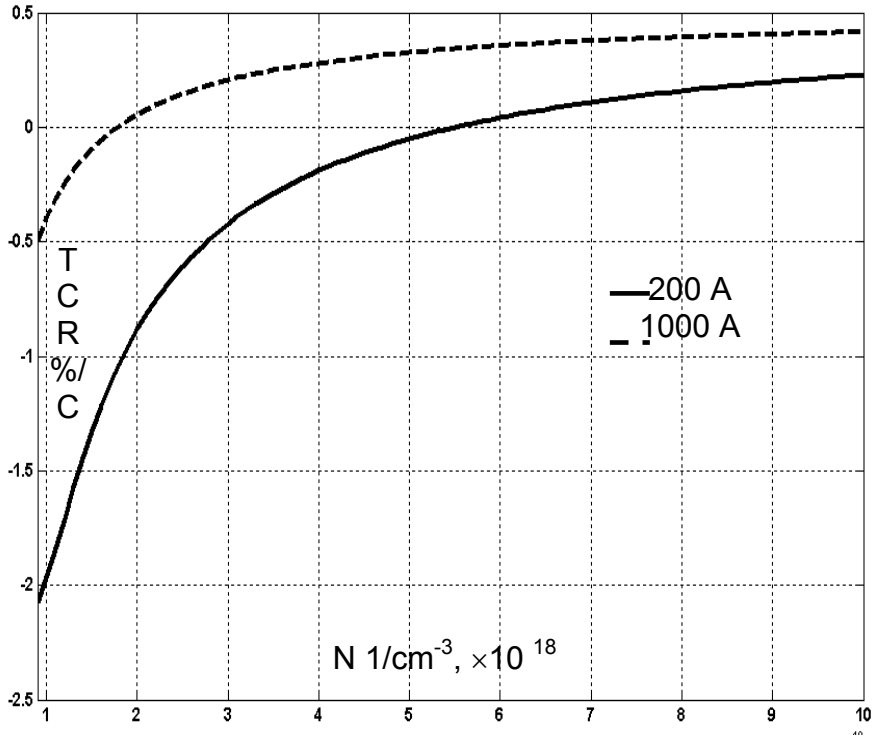

Fig. 7.40. TCR_{dc} versus doping concentration.

7.3.3. Geometry and dimensions of the MEMS temperature sensor

The goal in designing the temperature sensor is to have high sensitivity (i.e., large TCR_{dc}) and a resistivity in the range of kΩ (adequate range for electrical measurements). Figures 7.29 and Fig 7.30 show that large grain size has smaller resistivity, at the same

doping concentration than the small grain size. Therefore, large grain size is better for the sheet resistance in the range of kΩ. However, the smaller grain size results in much higher sensitivity to temperature. Since the objective is to have high thermal sensitivity, by increasing the doping concentration, the sheet resistance can also be controlled. Therefore, to make the small grain size, the deposition temperature and annealing temperature should be chosen in the range of 700°C to 800°C and 950°C to 1100°C, respectively. Also, if the doping concentration is 1×10^{18} atoms/cm^3, the TCR_{dc} is –2.1 %/°C, but resistivity is 11×10^{14} Ω-cm. The sheet resistance can be obtained by using the following equation (Sze, 1969):

$$R_s = \frac{\rho_e}{h} \quad , \tag{7.10}$$

where ρ_e, and h are resistivity and the thickness of the polysilicon film, respectively. Since the thickness of polysilicon layer is 0.5 μm, sheet resistance is 2.2 GΩ, which is out of the range of kΩ. Therefore, a compromise is needed between getting high sensitivity and a measurable value for resistivity. Thus, the doping concentration and grain size are selected to be 1.5×10^{18} atoms/cm^3 and 250 Å, respectively indicate the physical size of the temperature sensor also. With this assumption, the resistivity, sheet resistance, and TCR_{dc} are 14 Ω-cm, 200 kΩ, and 1.4 %/°C, respectively.

8. CONCLUSIONS AND RECOMMENDATIONS

The fundamental operation process of three MEMS sensors: pressure, relative humidity, and temperature has been studied. The study includes various aspects of theoretical, computational, and experimental investigations for each sensor. Conclusions and recommendations based on the results of this study follow.

The piezoresistive pressure sensor (PPS) was considered to measure the pressure of the environment in the range from 0 to 2 atm. In this sensor, diaphragm deforms due to pressure loads. These deformations are sensed by four strain gauges fabricated on the diaphragm. The gauges from Wheatstone bridge which produces an electrical signal indicating magnitude of the pressure load. Therefore, analysis of the PPS consists of two parts, the diaphragm, and the resistors on the diaphragm.

The rectangular diaphragm was selected to be 750 μm in length, 150μm in width, and 2μm in thickness. The analytical and computational solutions were performed to obtain the stress and strain in the diaphragm, with all edges fixed. These solutions indicated the places of extremum strains in the diaphragm for the maximum pressure of 2 atm. Since the direction of strains in x and y directions changes from the center to the edge, the polysilicon strain gauges should be placed in the center and edge of the diaphragm where the strain magnitudes are the greatest. Since the vertical strain component (perpendicular to the edge) is much greater than the transverse (parallel to the edge), the strain gauges should be placed perpendicular to each edge. Furthermore, the maximum stress occurs at the center of the longer edges, for the configuration considered in this thesis. As a result, two strain gauges should be placed perpendicular to the center

of the longer edges, one on each side of the diaphragm. Since the strain in *y*-direction are much larger and more uniform than those in the *x*-direction along the centerline of the diaphragm, the remaining two strain gauges should be placed perpendicular to the centerline at either end of the diaphragm. Because deformations of the diaphragm are on the order of magnitude of its thickness, placement of the gauges was facilitated by large deformations (geometry nonlinear) analysis.

Since strain gauges measure average strain over the area that they cover, average longitudinal and transverse strains were calculated versus length of the strain gauges at the center of longer edge and at the centerline of the diaphragm. Also, the sensitivity versus length and width of a strain gauge was calculated and indicate that the shorter the length and width of strain gauges are the greater the sensitivity. Because of the characteristic of the process used for fabrication of MEMS sensors, the optimum length and width of strain gauges are one-tenth of width and length, respectively, of the diaphragm. Since polysilicon is an anistropic material, the longitudinal gauge factor is much greater than the transverse gauge factor, which increases the sensitivity.

After analytical and experimental analysis of a pressure sensor, optoelectronic interferometric microscope (OELIM) methodology was used to perform deformation measurements of MEMS pressure sensor. OELIM measured deformations of the diaphragm of the PPS compared well with the analytically and computationally determined results.

While considering the capacitance humidity sensor two characteristics were considered: high sensitivity and short response time. Sensitivity is defined by the

changes in capacitance in response to the changes in the relative humidity, which is linearly proportional to the cross sectional area of the capacitor and inversely proportional to the dielectric thickness. Therefore, sensitivity increases by increasing the area and decreasing the thickness of sensitive layer. However, to obtain the short response time, the area of the diffusion layer should be as small as possible. Because of these conflicting requirements, the upper electrode with sensitive layer consists of a number of fingers that make a corresponding number of smaller parallel capacitors instead of one large capacitor. The width of the fingers and the space between them were determined by calculating the response time. Finally, the sensor consists of 50 fingers, each 1 mm long and 10 μm wide with the space of 10 μm between them. Good correlation between analytical and computational results was obtained, for the configuration of the relative humidity sensor developed in this thesis.

A polysilicon resistor was selected as the temperature sensor for measuring temperature in the range from –50°C to 150°C. The advantages of using polysilicon resistors are: they are compatible with monolithic silicon technology, provide adjustable resistance through several orders of magnitude by ion implantation, exhibit small parasitic capacitance and less dependence on the substrate bias because of a thick isolated oxide layer as were as, provide good linearity and large temperature sensitivity when lightly doped.

Taking into consideration current design practices, work of this thesis resulted in MEMS temperature sensor that is 1.5 μm long, 1.5 μm wide, and 0.5 μm thick.

As a summary, all three MEMS sensors: pressure, relative humidity, and temperature were designed.

Listed below are several tasks that should be accomplished as a continuation of the investigation presented in this thesis:

1) integrate the *p*, *RH* and, *T* sensors into a single package,
2) consider influence of the zone affected by one sensor on the performance of other sensors,
3) fabricate the sensors,
4) test the sensors,
5) develop a package for the sensors,
6) test and characterize the package.

9. REFERENCES

H. Ahne, H. Kruger, E. Pammer, and R. Rubner, 1984, "Polyimide patterns made directly from photopolymers," *Proc. Tecl. Conf. Polyimide*, 2:905-918, New York.

C. D. Ahrens, 1985, *Meteorology today*, Chapter 7, West Publishing Company, St. Paul, MN.

Amoco, 1992, *Technical data sheet for Amoco "ULTRADEL coating 7501,"* Amoco Chemical Co., Chicago.

Analog Devices, 2000, "Practical design techniques for sensor signal conditioning," *ADI reliability handbook*, Cambridge, MA.

H. Arai and T. Seiyama, 1989, *Sensors: a comprehensive survey*, Vol 2, Chapter 20, Verband Chemiehandel (VCH), New York.

Asahi, 1994, Tokyo, Japan, Technical data sheet for Asahi Chemical "Pimel TL-500, G-7000 and IX Grade, Asahi Chemical Co., Ltd.," Functional Products Division.

M. Asano, M. Eguchi, K. Kusano, and K. Niwa, 1993, "Development and commercialization of ionic-type photosensitive polyimides," *Polymers for Advanced Technologies*, 4(4):261-267.

A. Avallone and T. Baumeister, 1996*, Marks's standard handbook for mechanical engineers,* McGraw-Hill, New York.

G. Baccarani, B. Ricco, and G. Spadini, 1978 "Transport properties of polycrystalline silicon films," *J. Appl. Phys.*, 49:5565-5570.

W. Bacher, W. Menz, and J. Mohr, 1994, "The LIGA technique and its potential for microsystems," *Proc. Conf. on Industrial Electronics, Control, and Instrumentation IECON '94, 20th Internat*, 3:1466 –1471, Piscataway, NJ.

H. Baltes, O. Paul, J. G. Korvink, M. Schneider, J. Buhler, N. Schneeberger, D. Jaeggi, P. Malcovati, and M. Hornung, 1996, "IC MEMS microtransducers," *Internat. Electron Devices Meeting*, San Francisco, CA, Technical Digest, Cat. No. 96CH35961, pp. 521-524.

R. G. Barry and R. J. Chorley, 1992, *Atmosphere, weather and climate*, Chapter 2, 6ed, Routledge, New York.

L. G. Bassett, 1970, *Principles of chemistry*, Prentice-Hall, Upper Saddle River, NJ, pp. 456-459.

E. Bassous, 1995, “Fabrication of novel three-dimensional microstructure by anisotropic etching of (100) and (110) silicon,” *IEEE Trans. on Electron Devices*, 25:1178-1185.

T. Boltzhauser, A. Haeberli, and H. Baltes, 1993, “Piezoresistive membrane hygrometers based on IC technology,” *Sensors and Materials*, 5:125-134.

M. J. Bowden and S. R. Turner, 1988, *Electronic and Photonic Applications of polymers*, American Chemical Soc., Advances in Chemical Series, Series 218, Chapter 1, Washington, DC.

K. C. Brion, 1986, *Moisture sensors in process control*, Chapter 2, Elsevier Applied Science Publisher, New York.

G. C. Brown and R. J. Pryputniewicz, 2000, “New test methodology for static and dynamic shape measurements of microelectromechanical systems,” *Opt. Eng.*, 39:127-136.

L. Camporesi, 1998, “An overview of the applications of microelectromechanical devices,” http:/ / www.dig.bris.ac.uk/teaching/o_a_hf/lcamp.htm.

L. T. Canham, 1990, “Silicon quantum wire array fabrication by electrochemical and chemical dissolution of wafers,” *Appl. Phys. Lett.*, 57:1046-1051.

J. M. Cech, A. F. Burnett, and L. Knapp, 1991, “Pre-imidized photoimageable polyimide as a dielectric for high density multichip modules,” *Polymers Engineering and Science*, 32(21):1646-1652.

J. Chen, J. Zou, and C. Liu, 2001, “A review of MEMS fabrication technologies,” *J. Chinese Soc. Mech. Eng.,* 22:459-475.

G. Cocorullo, F. G. Della Corte, M. Iodice, I. Rendina, and P. M. Sarro, 1997, “An integrated silicon interferometric temperature sensor,” *Sensors and Acuators A*, 61:267-272.

F. M. Collins, 1961, “Vacuum evaporated silicon films,” *Trans. 8th Natl. Vac. Symp.,* MacMillan, New York, 2:899-904.

D. M. Considine, 1993, *Process/industrial instruments and controls handbook,* McGraw-Hill, New York.

T. A. Core, W. K. Tsang, and S. Sherman, 1993, “Fabrication technology for an integrated surface-micromachined sensor,” *Solid State Technology*, 36:39-47.

M. E. Cowher and T. O. Sedgwick, 1972, "Chemical vapor deposited polycrystalline silicon," *J. Electrochem. Soc*., 119:1565-1570.

J. Crank, 1975, *The mathematics of diffusion*, 2nd ed., Clarendon Press, Oxford, Chapter 4:44-69.

J. Das, S. M. Hossain, S. Chakraborty, and H. Saha, 2001, "Role of parasitics in humidity sensing by porous silicon," *Sensors and Actuators A*, 94:44-52.

D. R. Day, D. Ridley, J. Mario, and S. D. Senturia, 1984, "Polyimide planarization in integrated circuits," *Polyimides*, New York, 2:767-781.
G. Delapierre, H. Grange, B. Chambaz, and L. Destannes, 1983 "Polymer-based capacitive humidity sensor: characteristics and experimental results," *Sensors and Actuators A*, 4:97-104.

D. D. Denton, D. R. Day, D. F. Priore, and S. D. Senturia, 1985, "Moisture diffusion in polyimide films in integrated circuits," *J. Electronic Materials*, 14:119-136.

D. D. Denton, M. A. S. Jaafar, and A. R. K. Ralston, 1990, "The long term reliability of a switched capacitor relative humidity sensor system," *Proc. IEEE 33rd Midwest Symp. on Circuits and Systems*, New York, 854-857.

R. De Souza-Machado, R. M. C., Buncick, and D. D. Denton, 1991, *Proc. 4th Int. Conf. on Polyimides*, Ellenville, NY, pp. 133-136.

B. Diem, P. Rey, S. Renard, S. Viollet Bosson, H. Bono, F. Michel, M. T. Delaye, and G. Delapierre, 1995, "SOI 'SIMOX': from bulk to surface micromachining, a new age for silicon sensors and actuators," *Sensors and Actuators A (Physical),* 46:8-16.

T. H. Distefano and J. J. Cuomo, 1977, "Reduction of grain boundary recombination in polycrystalline silicon solar cells," *Appl. Phys. Lett.*, 30:351-353, 1977

M. Dokmeci and K. Najafi, 2001, "A high-sensitivity polyimide capacitive relative humidity sensor for monitoring anodically bonded hermetic micropackages," *J. Microelectromechanical Systems (JMEMS)*, 10:197-204.

F. W. Dunmore, 1938, "An electrometer and its application to radio metrography," *J. Res. Nat. Bur. Std.*, 20:723-744.

DuPont, 1994, Technical data sheet for DuPont "Pyralin PI 2700" Series, Dupont Co., Wilmington, DE.

W. Ehrfeld, F. Gotz, D. Munchmeyer, W. Schelb, and D. Schmidt, 1988, "LIGA process: sensor construction techniques via X-ray lithography," *Solid-State Sensor and Actuator Workshop,* Hilton Head Island, SC, IEEE Technical Digest:1–4.

R. Fenner and E. Zdankiewicz, 2001 "Micromachined water vapor sensors: a review of sensing technologies," *IEEE Sensors Journal*, 1(4):309-317.

R. P. Feynmann, 1959, "There is plenty of room at the bottom," *29th Annual Meeting of the American Physical Society at Caltech*,Caltech, CA.

R. S. Figiola and D. E. Beasley, 1991, *Theory and design for mechanical measurements*, Wiley, New York, pp. 447-483.

A. Foucaran, B. Sorli, M. Garcia, F. Pascal-Delannoy, A. Giani, and A. Boyer, 2000, "Porous silicon layer coupled with thermoelectric cooler: a humidity sensor," *Sensors and Actuators A*, 79:189-193.

P. J. French and A. G. R. Evans, 1989, "Piezoresistance in polysilicon and its application to strain gauges," *SolidState Electronics*, 32:1-10.

C. Furlong, 1999, *Hybrid, experimental and computational, approach for the efficient study and optimization of mechanical and electro-mechanical components*, Ph.D. dissertation, Worcester Polytechnic Institute, Worcester, MA.

C. Furlong and R. J. Pryputniewicz, 2000, "Absolute shape measurements using high-resolution optoelectronic holography methods," invited paper, special issue on optical shape measurement techniques, *Opt. Eng.*, 39(1):216-223.

C. Furlong and R. J. Pryputniewicz, 2001a, "Measurements and modeling of a nanoindentation process for MEMS," *Proc. Internat. Symp. on MEMS: Mechanics and Measurements*," Portland, OR, pp. 28-33.

C. Furlong and R. J. Pryputniewicz, 2001b, "Sensitivity, accuracy, and precision issues in quantitative optical metrology characterizations," *Internat. Congress on Experimental and Applied Mechanics for Emerging Technologies*, Portland, OR, pp. 631-634.

C. Furlong and R. J. Pryputniewicz, 2001c, "Computational and experimental approach to thermal management in microelectronics and packaging," invited paper, *J. Microelectronics Internat.*, 18(1):35-39.

C. Furlong and R. J. Pryputniewicz, 2002, "Advanced OEH methodology for evaluation of microelectronics and packaging," *Paper No. IMECE2002-39508*, Am. Soc. Mech. Eng., New York.

C. Furlong, R. J. Pryputniewicz, and J. S. Yokum, 2002, "Optimization of optical methodology for high-digital resolution quantitative evaluation of reliability of microelectronics and packaging," *Paper No. IMECE2002-39492*, Am. Soc. Mech. Eng., New York.

K. J. Gabriel, 1995, "Engineering microscopic machines," *Scientific American*, 273:118-121.

G. Gerlach and K. Sager, 1994, "A piezoresistive humidity sensor," *Sensors and Actuators A*, 43:181-184.

L. Gerzberg, 1979, *Monlithic power-spectrum centriod detector*, Ph.D. Dissertation, TR No. G557-2, Stanford Electronic Laboratories, Stanford, CA.

S. K. Ghandhi, 1977, *The theory and practice of microelectronics*, Wiley, New York, Chapter I.

J. Giachino, 2001, "MEMS design techniques, applications, and infrastructure," http://itri.loyola.edu/mems/d_7.htm.

H. Grange, C. Bieth, H. Boucher, and G. Delapierre, 1987, "A capacitive humidity sensor with very fast response time and very low hysteresis," *Sensors and Actuators A*, 12:291-296.

H. Guckel and D. Burns, 1984, "Planer processed polysilicon sealed cavities for pressure transducers array," *Internat. Electron Devices Meeting* (*IEDM),* New York, pp 223-225.

A. Hammerschmidt, H. Ahne, and E. Schmidth, 1989, "Heat-resistance relief patterns made from directly patternable polybenzoxazole precursors," *Polymeric Materials Science and Engineering*, 60:629-633.

D. S. Hanson, T. F. Marinis, C. Furlong, and R. J. Pryputniewicz, 2001, "Advances in optimization of MEMS inertial sensor packaging," *Proc. Internat. Congress on Experimental and Applied Mechanics in Emerging Technologies*, Portland, OR, pp. 821-825.

P. B. Hirch, A. Howie, R. B. Nichelson, D. W. Pashley, and M. J. Whelan, 1965, *Electron Microscopy of Thin Crystals*, Butterworth, London.

M. Hijikigawa, S. Miyoshi, T. Sugihara, and A. Jinda, 1983, "A thin-film resistance humidity sensor," *Sensors and Actuators A*, 4:307-315.

H. Hiramoto, 1990, "Photosensitive polyimides," *Proc. Symp. Materials Research Society Symp.*, 167:87-97.

M. Hirose, M. Taniguchi, and Y. Osaka, 1979, “Electronic properties of chemically deposited polycrystalline silicon,” *J. Appl. Phys*., 50:377-382.

Honeywell, 1998, *Temperature tutorial, comparing temperature sensors,* content.honeywell.com/building/ components/Hycal_Html/temp.asp.

K. Horie and T. Yamashita, 1995, *Photosensitive polyimides*, Technomic Publishing Company, Inc., Lancaster, PA.

G. Hougham, G. Tesoro, A. Viehbeck, and J. Shaw, 1991, “New fluorine-containing polyimides," *Proc. 4th Int. Conf. on Polyimides*, Ellenville, NY, 32(2):77-180.

R. T. Howe and R. S. Muller, 1986, “Resonant-microbridge vapor sensor,” *IEEE Trans. Electron Devices*, 33:499-506.

J. Hruby, 2001, “LIGA technologies and applications”, *MRS Bulletin,* 26:337-340.

T. R. Hsu, 2002, *MEMS & Microsystems design and manufacturing*, McGraw-Hill, New York.

M. S. Hu, M. Y. He, and A. G. Evans, 1991, “Solvent-induced damage in polyimide thin films,” *J. Materials Research*, 6(6):1374-1383.

T. Itoh, K. Kataoka, G. Engelmann, J. Wolf, O. Ehrmann, H. Reichl, and T. Suga, 2000, “MEMS IC test probe utilizing fritting contacts,” *Proc. SPIE*, 4019:244-249.

M. L. Jadhav, S. A. Gangal, and R. N. Karekar, 1985, “Study of the effect of humidity on AlO-x thin film resistors,” *Sensors and Actuators A*, 8:149-159.

T. I. Kamins, M. Mandurah, and K. C. Saraswat, 1978, “Structure and stability of low pressure chemically vapor-deposited silicon films,” *J. Electrochem. Soc.*, 125:927-932.

T. I. Kamins and T. R. Cass, 1973, “Structure of chemically deposited polycrystalline-silicon films,” *J. Thin Solid Films*, 16:147-165.

T. I. Kamins, 1971, “Hall mobility in chemically deposited polycrystalline silicon,” *J. App. Phys.*, 42:4357-4365.

T. I. Kamins, J. Manoliu, and R. N. Tucker, 1972, “Diffusion of impurities in polycrystalline silicon,” *J. Appl. Phys.*, 43:83-91.

T. I. Kamins, 1974 “Chemically vapor deposited polycrystalline-silicon films,” *IEEE Trans. on Parts, Hybrid, and Packaging*, PHP-10, pp 221-229.

T. I. Kamins, 1971, “Hall mobility in chemically deposited polycrystalline silicon,” *J. Apps. Phys*, 42:4357-4365.

U. Kang., and K. D. Wise, 1999, “A high-speed capacitive humidity sensor,” *in Dig. IEEE Solid-State Sensor and Actuator Workshop*, Hilton Head Island, SC, IEEE Technical Digest, pp183-186.

K. Kato, T. Ono, and Y. Amemiya, 1980, “Electrical trimming of polycrystalline silicon resistors and its application to analog ICs,” *IEEE Trans. on Electron Devices*, ED-27, New York, pp.2194-2198.

L. L. Kazmerski, 1980, *Polycrystalline and amorphous thin films and devices*, Academic Press, New York.

R. E. Kerwin and M .R. Goldrick, 1971, “Thermally stable photoresist polymer,” *Polymer Engineering and Science*, 11(5):426-430.

M. M. Khan, T. S. Tarter, and H. Fatemi, 1988, “Stress relief in plastic encapsulated integrated circuit devices by die coating with photosensitive polyimide,” *in Digest of the 38th Electronic Components Conference*, Los Angeles.

F. D. King, J. Shewchun, D. A. Thomson, H. D. Barber, and W. A. Pieczonka, 1973, “Polycrystalline silicon resistors for integrated circuits,” *Solid State Electronics*, 16:701-708.

W. H. Ko, J. Hynecek, and S. F. Boettcher, 1979, “Development of a miniature pressure transducer for biomedical application,” *IEEE Trans. Electronic Devices*, 26:1896-1905.

G. J. Korsh and R. S. Muller, 1978, “Conduction properties of lightly doped polycrystalline silicon,” *SolidState Electronics*, 21:1045-1051.

P. A. Krulevitch, 1994, “Micromechanical investigation of silicon and Ni-Ti-Cu thin films,” Ph. D. dissertation, University of California, Berkeley.

T. Kuroiwa, T. Hayashi, and A. Ito, 1993, “A thin film polyimide based capacitive type relative humidity sensor,” S*ensors and Actuators B*, 13-14:89-91.

J. M. Lauerhaas, G. M. Credo, J. L. Heinrich, and M. J. Sailor, 1992, “Reversible luminescence quenching of porous Si by solvents,” *J. Am. Chem. Soc*., 114:1911-1912.

C. Laville and C. Pellet, 2002, “Comparison of three humidity sensors for a pulmonary function diagnosis microsystem,” *IEEE Sensors J.*, 2:96-101.

S. Levy and S. Greenman, 1942, "Bending with large deflection of a clamped rectangular plate with length-width ratio of 1.5 under normal pressure," NACA Technical Note, No. 853, Washington, DC.

L. Lin and W. Yun, 1998, "Design, optimization and fabrication of surface micromachined pressure sensors," *Mechatronics*, 8:505-519.

B. Liptak, 1995, *Instrument engineers' handbook,* CRC Press LLC, Rodnor, PA, Chilton Book Co.

N. C. C. Lu, L. Gerzberg, and J. D. Meindl, 1980, "A quantitative model of the effect of grain size on the resistivity of polycrystalline silicon resistors," *IEEE Electron Dev. Lett*., ED-1, 38-41.

N. C. C. Lu, L. Gerzberg, and J. D. Meindl, 1981, "Modeling and optimization of monolithic polycrystalline silicon resistors," *IEEE Trans. on Electron Devices*, ED-28:818-830.

N. C. C. Lu, 1981, *Monolithic polycrystalline-silicon passive devices: theory, realization, and applications*, Ph.D. dissertation, TR No. G549-1, Stanford Electronic Laboratories, Stanford, CA.

E. Luder, 1986, "Polycrystalline silicon-based sensors," *Sensors and Actuators A*, 10:9-23.

S. E. Lyshevski, 2002, "Modeling and identification of induction micromachines in microelectromechanical systems applications," *Energy Conversion and Management*, 43:2123-2133.

M. Madou, 1997, *Fundamentals of microfabrication*, CRC Press, Boca Raton, FL.

M. M. Mandurah, K. C. Saraswat, and T. I. Kamins, 1979, "Phosphorus doping of low-pressure chemically vapor-deposited silicon films," *J. Electrochem. Soc.*, 126:1019-1023.

Y. Matsuoka, K. Yokota, S. Ogitani, A. Ikeda, H. Takahashi, and H. Ai, 1991, "Ester-type photosensitive polyimide precursor with low thermal pansion coefficient," *Polymer Engineering and Science*, 32(21):1618-1622.

M. Mehregany and C. A. Zorman, 2001 "Micromachining and microfabrication process technology VII," *Proc. SPIE,* 2: 4557-4560.

J. Melcher, Y. Daben, and G. Arlt, 1989, "Dielectric effects of moisture in polyimide," *IEEE Transa. Electronic Insulation*, 24(1):31-38.

MEMS,2003, “MEMS: Revolution of sorts,” http://www.frost.com/prod/news.nsf/3fcc3449277e0b738025695d006cfe7f/b6b15bdbc53797f265256b1f00157ff6?OpenDocument

L. M. Minsk and W. P. Van Deusen, 1948, *US Patent 2*,690,966.

K. Miyazaki, C. Xu, and M. Hieda, 1994, “ A new potential-type humidity sensor using EMD-based manganese oxides as a solid electrolyte,” *Journal of Electrochem. Soc.*, 141(4):35-37.

M. R. Monkowski, J. Bloem, L. J. Giling, and M. W. M. Graef, 1979, “Comparison of dopant incorporation into polycrystalline and monocrystalline silicon,” *Appl. Phys. Lett.*, 35:410-412.

Motorola, 1994, *Pressure sensor device*, Motorola Products Sector, Phoenix, AZ.

A. J. Mountvala and G. Abowitz, 1965, “Textural characteristics and electrical properties of vacuum evaporated silicon films,” *Vacuum*, 15:359-362.

R. S. Muller and T. I. Kamins, 1977, *Device electronics for integrated circuits*, Wiley, New York, Chapter I.

A. E. Nader, K. Imai, J. D. Craig, C. N. Lazaridis, D. O. Murray, M. T. Pottiger, S. A. Dombchik, and W. J. Lautenberger, 1991, “Synthesis and characterization of a low stress photosensitive polyimide,” *Polymer Engineering and Science*, 32(21),1613-1617.

S. C. Noe, J. Y. Pan, and S. D. Senturia, 1991, “Optical waveguiding as a method for characterizing the effect of extended cure and moisture on polyimide films,” *Annual Technical Conference-Society of Plastic Engineers*, 49:1598-1601.

T. Nomura, K. Oobuchi, T. Yasuda, and S. Furukawa, 1993, “Humidity sensor using surface acoustic wave delay line with hygroscopic dielectric film,” *J. Appl. Physics*, 32:4205-4208.

S. Numata, S. Oohara, K. Fujisaki, J. Imaizumi, and N. Kinjo, 1986, “Thermal expansion behavior of various aromatic polyimides,” *J. Appl. Polymer Sci.*, 31(1):101-110.

S. Numata, R. Tawata, T. Ikeda, K. Fujisaki, H. Shimanoki, and T. Miwa, 1991, “Preparation of aromatic acid anhydride complexes as cross linking agents,” *Japan Patent JP 03090076*.

OCG, 1994, Technical data sheet for Ciba Geigy “Probimide 7000, 7500 and 400”, OCG Microelectronics Materials AG, Basel, Switzerland

O'Halloran, J. Groeneweg, P. M. Sarro, and P. J. French, 1997, "Porous silicon membrane for humidity sensing applications," *in: Proceedings of the Eurosensors XII*: Los Angeles, pp 901-904.

Omegadyne, 1996, *Omegadvne pressure, force, load, torque databook,* www.omegadyne.com/intsafe.html.

Omega, 1996, *The pressure, strain, and force handbook*, Omega Inc., Stamford, CT.

Omega, 2003, http://www.omega.com/literature/transactions/volume3/pressure.html.

G. L. Pearson and J. Bardeen, 1949, "Electrical properties of pure silicon and silicon alloys containing boron and phosphorous," *Phys. Rev.*, 75:865-883.

K. E. Peterson, 1982, "Silicon as a mechanical material," *Proc. IEEE*, 70:420-457.

Piezosensors, 2001, "Choosing a humidity sensor: a review of three technologies," http://www.sensorsmag.com/articles/00701/main

G. E. Pike and C. H. Seager, 1979, "The dc voltage dependence of semiconductor grain-boundary resistance," *J. Appl. Phys.*, 50:3414-3422.

R. J. Pryputniewicz, 1995, "Quantitative determination of displacements and strains from holograms," ch. 3 in *holographic interferometry*, vol. 68 of Springer series in Science, Springer-Verlog, Berlin, pp. 33-72.

R. J. Pryputniewicz, 2000, "Integrated approach to teaching of design, analysis, and characterization in miromechatronics," *Symposium on Design Education with Mechatronics and MEMS, Paper No. DE-13*, Orlando, FL.

E. J. Pryputniewicz, S. L. Miller, M. P. de Boer, G. C. Brown, R. R. Biederman, and R. J. Pryputniewicz, 2000a, "Experimental and analytical characterization of dynamic effects in electrostatic microengines," *Proc. Internat. Symp. on Microscale Systems*, Orlando, FL, pp. 80-83.

R. J. Pryputniewicz, J. J. Allen, C. W. Dyck, and G. C. Brown, 2000b, "Experimental method for measurements of dynamic characteristics of microgyroscopes," *Proc. Internat. Symp. on Microscale Systems*, Orlando, FL, pp. 84-87.

R. J. Pryputniewicz, R. P. Champagne, J. P. Angelosanto, G. C. Brown, C. Furlong, and E. J. Pryputniewicz, 2000c, "Multivariable MEMS polysilicon sensor: analysis and measurements," *Proc. Internat. Symp. on Microscale Systems*, Orlando, FL, pp. 76-79.

R. J. Pryputniewicz, M. P. de Boer, and G. C. Brown, 2000d, "Advances in optical methodology for studies of dynamic characteristics of MEMS microengines rotating at high speeds," *Proc. IX Internat. Congress on Exp. Mech*., SEM, Bethel, CT, pp. 1009-1012.

R. J. Pryputniewicz, 2001, "MEMS design education by case studies," *Paper No. IMECE2001/DE-23292*, Am. Soc. Mech. Eng., New York, NY.

D. R. Pryputniewicz, C. Furlong, and R. J. Pryputniewicz, 2001a, "ACES approach to the study of material properties of MEMS," *Proc. Internat. Symp. on MEMS: Mechanics and Measurements*," Portland, OR, pp. 80-83.

R. J. Pryputniewicz, J. J. Allen, C. W. Dyck, and G. C. Brown, 2001b, "Dynamic characterization of MEMS microgyros," *Proc. 28th Annual Symp. & Exhibition of IMAPS-NE*, Boxboro, MA, pp. 218-224.

R. J. Pryputniewicz, J. P. Angelosanto, G. C. Brown, C. Furlong, and R. J. Pryputniewicz, 2001c, "New hybrid methodology for the development of MEMS multivariable sensors," *Paper No. IMECE2001/EPP-24722*, Am. Soc. Mech. Eng., New York, NY.

R. J. Pryputniewicz, J. P. Angelosanto, C. Furlong, G. C. Brown, and E. J. Pryputniewicz, 2001d, "Analysis and measurements of high pressure response of MEMS sensors," *Proc. Internat. Symp. on MEMS: Mechanics and Measurements*," Portland, OR, pp. 76-79.

R. J. Pryputniewicz, C. Furlong, G. C. Brown, and E. J. Pryputniewicz, 2001e, "Optical methodology for static and dynamic measurements of nanodisplacements," *Proc. Internat Congress on Experimental and Applied Mechanics for Emerging Technologies*, Portland, OR, pp. 826-831.

R. J. Pryputniewicz, C. Furlong, G. C. Brown, E. J. Pryputniewicz, and M. E. Seta, 2001f, "ACES methodology for studies of MEMS," *Proc. 28th Annual Symp. & Exhibition of IMAPS-NE*, Boxboro, MA, pp. 208-217.

R. J. Pryputniewicz, C. Furlong, G. C. Brown, E. J. Pryputniewicz, and M. E. Seta, 2001g, "Optoelectronic method for studies of MEMS," *Proc. Internat Congress on Experimental and Applied Mechanics for Emerging Technologies*, Portland, OR, pp. 817-820.

R. J. Pryputniewicz, P. Galambos, G. C. Brown, C. Furlong, and E. J. Pryputniewicz, 2001h, "ACES characterization of surface micromachined microfluidic devices," *Internat. J. Microcircuits and Electronic Packaging (IJMEP)*, 24:30-36.

R. J. Pryputniewicz, T. M. Marinis, D. S. Hanson, and C. Furlong, 2001i, "New approach to development of packaging for MEMS inertial sensors," *Paper No. IMECE2001/MEMS-23906*, Am. Soc. Mech. Eng., New York, NY.

R. J. Pryputniewicz, C. Furlong, and E. J. Pryputniewicz, 2002a, "Design by analysis of a MEMS pressure sensor," *Proc. 35th Internat. Symp. on Microelectronics*, Denver, CO, pp. 81-86.

R. J. Pryputniewicz, C. Furlong, and E. J. Pryputniewicz, 2002b, "Optimization of contact dynamics for an RF MEMS switch," *Paper No. IMECE2002-39504*, Am. Soc. Mech. Eng., New York.

R. J. Pryputniewicz and C. Furlong, 2003, "Novel optoelectronic methodology for testing of MOEMS," *Proc. Internat. Symp. on MOEMS and Miniaturized Systems III*, SPIE-4983:11-25.

A. J. Przekwas, M. Turowski, M. Furmanczyk, A. Heike, and R. J. Pryputniewicz, 2001, "Multiphysics design and simulation environment for microelectromechanical systems," *Proc. Internat. Symp. on MEMS: Mechanics and Measurements*," Portland, OR, pp. 84-89.

W. Qu. and J. U. Meyer, 1992, "A novel thick film ceramic humidity sensitive characteristics of α-Fe_2O_3 ceramic sensor," *J. Am. Ceram. Soc*., 75:546-551.

A. R. K. Ralston, M. C. Buncick, and D. D. Denton, 1990, "Effects of aging on polyimide: a model for dielectric behavior," *IEEE Solid-State Sensor and Actuator Workshop*, Hilton Head, SC, IEEE Technical Digest, pp. 759-763.

A. R. K. Ralston, C. F. Klein, P. E. Thoma, and D. D. Denton, 1995, "A model for the relative environmental stability of a series of polyimide capacitance humidity sensors," *Proc. Int. Conf. on Solid-State Sensors and Actuators (Transducers'95)*, Stockholm, Sweden: pp.821-824.

W. Ramberg, A. E. Mcpherson, and S. Levy, 1942, "Normal-pressure tests of rectangular plates," NACA Technical Note.No. 849, Washington, DC.

K. N. Ratnakumar, J. D. Meindl, and D. Bartelink, 1980, "Performance limits of E/D NMOS VLSI," *ISSCC Digest of Tech. Papers*, pp. 74-75.

M. Ree, S. Swanson, and W. Volksen, 1991, "Residual stress and its relaxation behavior of high-temperature polyimides: effect of precursor origin," *Proc. 4th Int. Conf. on Polyimides*, New York, 601-617.

M. Ree, K. J. Rex Chen, and G. Czornyj, 1992, “Effect of UV exposure and thermal history on properties of a preimidized photosensitive polyimide,” *Polymer Engineering and Science*, 32(14):924-930.

A. Reiser, 1989, *Photoreactive polymers*, Wiley, New York.

S. Renard and V. Gaff, 2000, “Chip size packaging for MEMS and ICs realized at the wafer level,” *MST News*, 1:18-19.

R. J. Roark, 1965, *Formulas for stress and strain*, McGraw-Hill, New York.

C. Roman, O. Bodea, N. Prodan, A. Levi, E. Cordos, and I. Manoviciu, 1995, “A capacitive–type humidity sensor using crosslinked poly (methyl methacrylate-co-(2 Hydroxyproxy)-Methacrylate),” *Sensors and Actuators B*, 24-25:710-713.

R. Rubner, W. Kleeberg, and E. Kuhn, 1974, “Photohardenable polyester compositions,” *German Patent 2437348*.

R. Rubner, A. Hammerschmidt, R. Leuschner, and H. Ahne, 1990, “Photopatternable organic dielectrics: polybenzoxazoles versus polyimides,” *Polymers for Microelectronics-Science and Technology*, Tokyo, Japan, pp. 789-810.

W. R. Runyan, 1965, *Silicon semiconductor technology*, McGraw-Hill, New York, Chapter VIII.

W. S. Ruska, 1987, *Microelectronic processing*, McGraw-Hill, New York.

Y. Sadaoka, M. Matsuguchi, Y. Sakai, and Y. Murata, 1992, “ Optical humidity sensing characteristics of Nafion-dyes composite thin films,” *Sensors and Actuators B*, 7:443-446.

K. Sager, G. Gerlach, A. Nakladal, and A. Schroth, 1994, “Ambient humidity and moisture a decisive failure sources in piezoresistive sensors,” *Sensors and Actuators A*, 46:171-175.

Schechter, M. Ben-Chorin, and A. Kux, 1995, “Gas sensing properties of porous silicon,” *Anal. Chem.*, 67:3727-3732.

C. H. Seager and T. G. Castner, 1978, “Zero-bias resistance of grain boundaries in neutron-transmutation-doped polycrystalline silicon,” *J. Appl. Phys.*, 49:3879-3889.

J. Y. W. Seto, 1975, “The electrical properties of polycrystalline silicon films,” *J. Appl. Phys.*, 46:5247-5254.

H. Shimizu, H. Matsumoto, M. Asakura, and K. Watanabe, 1988, "A digital hygrometer," *IEEE Instrumentation and Measurement Technology Conference*, Los Angeles: pp.173-177.

S. N. Singh, R. Kirshore, and P. K. Singh, 1985, "*J. Appl. Phys*., 57: 2793-2799.

C. S. Smith, 1954, " Piezoresistive effect in germanium and silicon," *Phys. Rev*., 94:42-49.

D. S. Soane and Z. Martynenko, 1989, *Polymers in microelectronics-fundamentals and applications*, Elsevier: Amsterdam.

E. Spenke, 1958, *Electronic semiconductors*, McGraw-Hill, NewYork, pp. 387-394.

SRAC, 2003, *Advanced finite element analysis*, Structural Research Analysis Corp., Los Angeles, CA.

S. Stadler and P. K. Ajmera, 2002, "Integration of LIGA structures with CMOS circuitry," *Sensors and Materials*, 14:151-166.

G. Stix, 1992, "Micron machinations", *Sci. Am.*, 267:73-80.

S. Sugiyama, M. Takigawa, and I. Igarashi, 1983 "Integrated piezoresistive pressure sensor with both voltage and frequency output," *Sensors and Actuators A,* 4:113-120

S. Sugiyama, K. Shimaoka, and O. Tabata, 1992, "Surface micromachined micro-diaphragm pressure sensors," *Proc. 6th Internat. Conf. on Solid-State Sensors and Actuators*, pp.188-191, Piscataway, NJ.

S. Suwazono, H. Tanigawa, and M. Hirata, 1987, "Diaphragm thickness control in silicon pressure sensor using an anodic etch-stop," *J. Electromechanical Soc.*,134:2037- 2041.

K. Suzuki, S. Suwazono, and T. Ishihara, 1987, "CMOS integrated silicon pressure sensor," *IEEE J. Solid-State Circuits*, 22:151-156.

I. S. M. Sze, 1969, *Physics of semiconductor devices*, Wiley, New York, Chapter I, IV, VIII.

W. C. Tang, 2001, "Surface micromachining: a brief introduction," *MRS Bulletin*, 26:289-290.

Z. H. Tao and Z. Bin, 2002, "Microelectromechanical system technology and its application," *Electronic Components & Materials*, 21:28-30.

M. L. Tarng, 1978, “Carrier transport in oxygen-rich polycrystalline silicon films,” *J. Appl. Phys.*, 49, 4069-4076.

S. Timoshenko, 1959, *Theory of plates and shells*, McGraw-Hill, New York, pp. 419-423.

M. Tomokawa, H. Asano, G. Okbayashi, H. Hiramoto, Y. Morishima, and M. Kamadu, 1992, “Photo-reaction of ionic bonding photosensitive polyimide,” *Journal of Photopolymer Science and Technology*, 5(2):343-350.

Toray, 1992, Technical data sheet for Toray “Photoneece UR-5100”, Toray Ind., Tokyo, Japan.

E. Traversa, 1995, “ Ceramic sensors for humidity detection: the state-of-the-art and future development,” *Sensors and Actuators B*, 23:135-156.

S. Tsuchitani, T. Sugawara, N. Kinjo, and S. Ohara, 1985, “ Humidity sensor using ionic copolymer,” *IEEE Int. Conf. on Solid-State Sensors and Actuators (Transducers ’85)*, Piscataway, NJ, pp. 210-212.

O. N. Tufte, P. W. Chapman, and D. Long, 1962 “Silicon diffused-element piezoresistive diaphragm,” *J. Appl. Phys*, 33:22-33.

D. R. Tuner, 1958, “Electropolishing silicon in hydrofluoric acid solution,” *J. Electrochemical Soc.*, 105:402-405.

E. Ventsel, and T. Krauthammer, 2001, *Thin plates and shells*, Marcel-Dekker, New York.

Y. Wada and S. Nishimatsu, 1978, “Grain growth mechanism of heavily phosphorous-Implanted polycrystalline silicon,” *J. Electrochem. Soc.*, 125:1499-1504.

C. T. Wang, 1953, *Applied elasticity*, McGraw-Hill, NewYork, pp. 286-291.

N. M. White and J. D. Turner, 1997,“Thick film sensors: past, present and future,” *Measur. Sci. Technol*, 8:1-20.

H. F. Wolf, 1969, *Silicon semiconductor data*, Pergamon Press, Oxford, Chapter II.

D. K. Yang, W. J. Koros, H. B. Hopfenberg, and V. T. Stannett, 1985, “Sorption and transport of water in kapton polyimide,” *J. Appl. Polymer Sci.*, 30:1035-1047.

D. K. Yang, W. J. Koros, H. B. Hopfenberg, and V. T. Stannett, 1986, “The effects of morphology and hygrothermal aging on water sorption and transport in kapton polyimide,” *J. Appl. Polymer Sci.*, 31:1619-1629.

N. Yamazoe, 1986, “Humidity sensors: principles and applications,” *Sensors and Actuators*, 10:379-398.

N. Yoda and H. Hiramoto, 1984, “New photosensitive high temperature polymers for electronic applications,” *J. Macromolecular Science and Chemistry*, A21(13-14): 1641-1663.

APPENDIX A. Matlab program for determining the parameters a_{mn} for different number of m, n

```
% In this program, the kramer method is used to determine the amn.
% Input
%   m,n  the number of sentences for infinite series,
%   K        the length-width ratio for the diaphragm
%   P        uniform pressure
%   D        flexyral rigidity of the plate
%   aa       length of the diaphragm
%   B        the constant vector
% Output
%   A        the coefficient matrix
%   X        the vector that include amn
clear all;
m=10;
n=10;
k=5;
m1=m^2;
n1=n^2;
syms p D aa;
B=ones(m1,1)*(p/(4*D))*((aa/pi)^4);
for i=1:m1
   for j=1:n1
      a=fix(i/m)+1;
      b=fix(j/n)+1;
      c=rem(i,m);
      d=rem(j,n);
      if (d==0)
         b=b-1;
      end;
      if (c==0)
         a=a-1;
      end;
      if i==j
         if c==0
            f=c+n;
         else
            f=c;
         end;
        A(i,j)= 3*(a^4)+3*((f*k)^4)+2*((a*f*k)^2);
      elseif (c==d) &( a~=b)
```

```
          if c==0
             cc=c+m;
          else
             cc=c;
          end;
           A(i,j)=2*(cc*k)^4;
       elseif  (a==b) & (c~=d)
           A(i,j)=2*(a)^4;
       else
           A(i,j)=0;
       end;
    end;
end;
display(A);
S=inv(A);
X=S*B
e0=8.84 *10^(-12);
d=2*10^(-6);
c1=1;
c2=1;
D=4.2*10^-13;
k=1;
syms x y ;
r=1;
t=1;
for a=0.0005:0.0005:0.002
    for b=0.0005:0.0005:0.002
        S1=(1/d)*(e0*c1*4*a*b+e0*c2*4*a*b*k*t);
        S2=(e0*c2*16)/(d*pi^2);
        S11=0;
        for i=1:3
            for j=1:3
                m=i-1;
                n=j-1;
                alpha=(D*pi^2/4)*(((2*m+1)^2)/(a^2)+((2*n+1)^2)/(b^2));
                S3=((-1)^(m+n))/((2*m+1)*(2*n+1));
                S4=(k/alpha)*(1-exp(-alpha*t));
                S5=(M0^2)*exp(-alpha*t);
                S6=cos(((2*m+1)*pi*x)/(2*a))*cos(((2*n+1)*pi*y)/(2*b));
                S7=int(S6,x,-a,a);
                S8=int(S7,y,-a,a);
                S9=S3*S4+S5;
                S10=S9*S8;
                S11=S11+s10*S2+S1;
```

```
            end;
        end;
        out(r,t)=S11;
        t=t+1;
    end;
    r=1;
    r=r+1;
end;
a=0.5*10^-3:0.5*10^-3:2*10^-3;
b=0.5*10^-3:0.5*10^-3:2*10^-3;
mesh(b,a,out)
view(3)
```

APPENDIX B. Matlab program for calculating the sensitivity of the diaphragm using different numbers of terms in infinite series.

```
% Input
%  aa      length of the diaphragm
%  bb      the width of the diaphragm
%  t       the thickness of the diaphragm
%  GF1     the longitudal gauge factor
%  GF2     the transverse gauge factor
%  x1      the distance between the shorter edge and the middle of the strain gauges
%          in the centerline of the diaphragm
%  P       uniform pressure
%  E       Young's modulus
%  v       Possion ratio
%  D       flexural rigidity of the plate
%  Ei      the input voltage for wheatstone bridge
%  m,n     the number of sentences in the infinite series
%  K       the length-width ratio in the diaphragm
%  L       the length of the strain gauge
%  w       the width of the strain gauge

%  Eo      the output voltage of the wheatstone bridge as a function of length and
           width of strain gauge
S          the sensitivity for the diaphragm as a function of length and width of strain
           gauge

clear all;
aa=750*10^(-6);
bb=150*10^(-6);
t=2*10^(-6);
GF1=39;
GF2=-15;
x1=aa/3;
p=2*10^5;
E=1.60*10^11;
v=0.25;
D=E*(t^3)/(12*(1-v^2));
p1=p*((bb/pi)^4)/D;
Ei=20;
m=10;
```

```
n=10;
k=5;
m1=m^2;
n1=n^2;
B=ones(m1,1)*(p/(4*D))*((aa/pi)^4);
for i=1:m1
   for j=1:n1
      a=fix(i/m)+1;
      b=fix(j/n)+1;
      c=rem(i,m);
      d=rem(j,n);
      if (d==0)
         b=b-1;
      end;
      if (c==0)
         a=a-1;
      end;
      if i==j
         if c==0
            f=c+n;
         else
            f=c;
         end;
        A(i,j)= 3*(a^4)+3*((f*k)^4)+2*((a*f*k)^2);
      elseif (c==d) &( a~=b)
         if c==0
            cc=c+m;
         else
            cc=c;
         end;
          A(i,j)=2*(cc*k)^4;
      elseif  (a==b) & (c~=d)
           A(i,j)=2*(a)^4;
      else
           A(i,j)=0;
      end;
   end;
end;
S=inv(A);
X=S*B;
z=1;
jj=1;
  for L=0.1e-6:2e-6:50e-6
    for w=0.1e-6:2e-6:200e-6
```

```
        E0=0;
        q=1;
        for r=1:m
            for s=1:n
              E0=(E0+pi*t*( (GF1+1/(2*v))*( s*X(q,1)/(L*bb))*( (1-
cos(pi*r))*sin(2*s*pi*L/bb) -2*(1-cos(2*pi*r*x1/aa))*cos(s*pi)*sin(s*pi*L/bb)
)+(2*r*X(q,1)/(aa*w))*(GF2+1/(2*v))*( (1-cos(s*pi*L/bb))*sin(r*pi*w/aa)*cos(r*pi)-
(1-cos(s*pi))*sin(r*pi*w/aa)*cos(2*pi*r*x1/aa)) ));
               q=q+1;
            end;
        end;
        out(z,jj)=E0*(10^6)/(Ei*p);
        z=z+1;
    end;
    z=1;
   jj=jj+1;
end;
L=0.1e-6:2e-6:50e-6;
w=0.1e-6:2e-6:200e-6;
mesh(L,w,out)
view(3);
xlabel('L');
ylabel('w');
zlabel('sensitivity');
```

APPENDIX C. Matlab program for calculating the barrier resistivity, resistivity and thermal coefficient resistance (TCR) for the temperature sensor.

```
function [rob, ro, TCR]=tcrcal81(N,L,et,Qt,f)
%-----------------------
% Input values
%N, and L can be entered in cm^-3, and Angstrom.
%N=1*10^18;%cm^-3
%L=230;%angstrom
%f=0.12;%unitless
%Length=5;%micron
Vg=0.10;%volt
I=0;
%-----------------------
N_star=7.3*10^16;%cm^-3
q=1.602*10^-19;%C
K=1.38*10^(-23);%J/K
ni=1.45*10^10;%cm^-3
Eg=1.12;%ev
mo=9.11*10^-31;%kg
mpr=0.81;%unitless
mh=mpr*mo; %kg
e=11.7*8.854*10^-14;%Fard/cm
roc=21*10^5;%ohm-cm
T=300; %K
%Qt=2.98*10^12; %cm^-2
%et=-0.18; %eV
me=1.08*mo; %kg
thickness=0.5*10^-4;%cm
A=8*10^-8;
%---------------------------------
%Eg=1.16-((7.02*10^(-4)*T^2)/(T+1108));
%ni=2*((2*pi*K*T/h^2)^1.5)*((me*mh)^(3/4))*exp(-Eg/2*K*T);
%---------------------------------------
%change all units to metric
% each electron volt is equal to 1.602*10^-19 j.
%N_star=N_star*10^6;
%roc=roc*10^(-2);
L=L*10^(-8);%cm
%Qt=Qt*10^4;
%N=N*10^6;
%ni=ni*10^6;
```

```
%Eg=Eg*(1.602*10^-19);
%et=et*1.602*10^-19;
%-------------------------------
%Ng=Length*10000/L;
option = optimset('TolX',10^-20);
j=(1/1.602)*10^19;%converting j to ev.
if (N<N_star)|(N==N_star)
   W=L/2;
   vb=q*N*(L^2)/(8*e);
   Ef=et-q*vb*j+K*T*j*log((1/2)*((Qt/(L*N))-1));
   po=ni*exp(-Ef/(K*T*j));
   pave=ni*exp(-
Ef/(K*T*j))*((1/q*L)*((2*pi*e*K*T/N)^0.5)*erf((q*L/2)*(N/(2*e*K*T))^0.5));
   Eaa=Eg/2+et+K*T*j;

 else
   EA=-(Eg/2)+ 0.08-(4.3*10^(-8))*N^(1/3);
   b=EA/(K*T*j);
   c3=1/(K*T*j);
   uf = inline([sprintf('%25.20f',ni) '*' 'exp(-Ef1*' sprintf('%25.20f',c3) ')*(1+2*exp('
sprintf('%25.20f',b) '-Ef1*' sprintf('%25.20f',c3) '))-' sprintf('%25.20f',N)]);
   %[Ef,fval,exitflag,output] = fzero(uf,0,option);
   Ef=fzero(uf,0);
   N_plus=N/(1+2*exp((EA-Ef)/(K*T*j)));
   c1=(ni/N_plus)*exp(-et/(K*T*j));
   c2=(q^2)*N/(2*e*K*T);
   c11=exp((Ef-et)/(K*T*j));
   Qt=double(Qt);N=double(N);c1=double(c1);c2=double(c2);
   uf2=inline(['W1-(' sprintf('%25.20f',Qt) '/(2*' sprintf('%25.20f',N) '*(1+2*'
sprintf('%25.20f',c1) '*exp((W1^2)*' sprintf('%25.20f',c2) '))))']);
   %uf2=inline(['W1-(' sprintf('%25.20f',Qt) '/(2*' sprintf('%25.20f',N) '*(1+2*'
sprintf('%25.20f',c11) '*exp((W1^2)*' sprintf('%25.20f',c2) '))))'])
   %uf2=inline(['W1*2*' sprintf('%25.20f',N) '*(1+2*' sprintf('%25.20f',c1)
'*exp((W1^2)*' sprintf('%25.20f',c2) '))-' sprintf('%25.20f',Qt)])
   [W,fval,exitflag,output]=fzero(uf2,15e-8,option);
   vb=q*N*(W^2)/(2*e);
   po=ni*exp(-Ef/(K*T*j));
   pave=ni*exp(-Ef/(K*T*j))*((1-
2*W/L)+(1/(L*q))*((2*pi*e*K*T/N)^0.5)*erf(q*W*(N/(2*e*K*T))^0.5));
 end
 rob=(1/(f*2*W*(q^2)*pave))*((2*pi*mh*K*T)^0.5)*exp(q*vb/(K*T));
 rob=rob*10^-2; % ohm-cm
 %ro=rob*(2*W/L)+roc*(1-2*W/L)
```

```
ro=rob*(2*W/L);
syms TT;
I=2*10^-8*q*po*((K*TT/(2*pi*mh))^0.5)*exp(-q*vb/(K*TT))*sinh(q*Vg/(2*K*TT));
I=I*100;
V=5;
R=V/I;
TCRdc=100*(R^(-1))*(diff(R,TT));
TCR=subs(TCRdc,300);


s=zeros(91,6);
r=zeros(1,3);
NN=9:100;
L=[230, 1220]
for n=1:length(L)
   if L(n)==1220
      et=-0.17;
      Qt=1.9*10^12;
      f=0.06;
   else
      et=-0.18;
      Qt=3.34*10^12;
      f=0.12;
   end;
   for i=1:length(NN)
          NNN=NN(i)*10^17;
      [a b c]=tcrcal82(NNN,L(n),et,Qt,f);
       s(i,((n-1)*3+1):((n-1)*3+3))=[a b c];
   end
end
display(s)
NN=9:100;
plot(NN*10^17,abs(s(:,1)))
figure
plot(NN*10^17,abs(s(:,4)))
figure
plot(NN*10^17,abs(s(:,2)))
figure
plot(NN*10^17,abs(s(:,5)))
figure
plot(NN*10^17,s(:,3))
hold on
plot(NN*10^17,s(:,6),'r')
```

APPENDIX D. MathCAD program for determining the uncertainty of maximum stress in *y*-direction in the PPS.

Input

r The stress ratio that is read from the graph
E The Young's modulus
h The thickness of the diaphragm
a The width of the diaphragm
dr The uncertainty in the stress ratio
dE The Young's modulus uncertainty
dh The thickness uncertainty
da The width uncertainty

Output

S1 The maximum stress in y direction
dS The uncertainty in maximum stress in y direction
ddS The percentage of uncertainty in the stress
ddr The percentage contribution of stress ratio in the uncertainty of the maximum stress
ddE The percentage contribution of Young's modulus in the uncertainty of the maximum stress
ddh The percentage contribution of thickness in the uncertainty of the maximum stress
dda The percentage contribution of width in the uncertainty of the maximum stress

$r := 18$

$\delta r := 0.5$ (Pa)

$E := 160 \cdot 10^{9}$ (Pa)

$\delta E := 5 \cdot 10^{9}$ (m)

$h := 2 \cdot 10^{-6}$ (m)

$\delta h := 0.05 \cdot 10^{-6}$ (m)

$a := 150 \cdot 10^{-6}$ (m)

$\delta a := 2 \cdot 10^{-6}$

$$S1 := r \cdot E \cdot \frac{(h)^2}{a^2}$$

$S1 = 5.12 \times 10^{8}$

$$S(r,E,h,a) := r\cdot E\cdot\frac{(h)^2}{a^2}$$

$$\frac{d}{dr}S(r,E,h,a) = 2.844\times 10^{7}$$

$$\frac{d}{dE}S(r,E,h,a) = 3.2\times 10^{-3}$$

$$\frac{d}{dh}S(r,E,h,a) = 5.12\times 10^{14}$$

$$\frac{d}{da}S(r,E,h,a) = -6.827\times 10^{12}$$

$$\delta S := \left[\left[\left(\frac{d}{dr}S(r,E,h,a)\right)\cdot\delta r\right]^2 + \left[\left(\frac{d}{dE}S(r,E,h,a)\right)\cdot\delta E\right]^2 \ldots \right.$$
$$\left. + \left[\left(\frac{d}{dh}S(r,E,h,a)\right)\cdot\delta h\right]^2 + \left[\left(\frac{d}{da}S(r,E,h,a)\right)\cdot\delta a\right]^2 \right]^{0.5}$$

$$\delta S = 3.606\times 10^{7}$$

$$\delta\delta S := \frac{\delta S}{S1}\cdot 100$$

$$\delta\delta S = 7.042$$

$$\delta\delta r := \frac{\left[\left(\frac{d}{dr}S(r,E,h,a)\right)\cdot\delta r\right]^2}{(\delta S)^2}\cdot 100$$

$$\delta\delta r = 15.559$$

$$\delta\delta E := \frac{\left[\left(\frac{d}{dE}S(r,E,h,a)\right)\cdot\delta E\right]^2}{(\delta S)^2}\cdot 100$$

$\delta\delta E = 19.692$

$$\delta\delta h := \frac{\left[\left(\frac{d}{dh} S(r, E, h, a)\right) \cdot \delta h\right]^2}{(\delta S)^2} \cdot 100$$

$\delta\delta h = 50.411$

$$\delta\delta a := \frac{\left[\left(\frac{d}{da} S(r, E, h, a)\right) \cdot \delta a\right]^2}{(\delta S)^2} \cdot 100$$

$\delta\delta a = 14.339$

$\delta\delta r + \delta\delta E + \delta\delta a + \delta\delta h = 100$

$\delta\delta h = 50.411$

$\delta\delta E = 19.692$

$\delta\delta r = 15.559$

$\delta\delta a = 14.339$